Quantum simulation and out-of-equilibrium dynamics of quantum gases in optical cavities

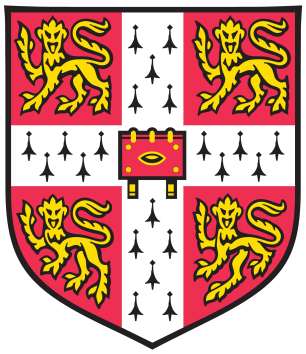

Ezequiel Ignacio Rodríguez Chiacchio

Homerton College
University of Cambridge

Supervisor: Dr. Andreas Nunnenkamp

June, 2020

This dissertation is submitted for the degree of Doctor of Philosophy

To my grandfather.

Declaration

I hereby declare that except where specific reference is made to the work of others, the contents of this dissertation are original and have not been submitted in whole or in part for consideration for any other degree or qualification in this or any other institution. This dissertation is my own work and contains nothing which is the outcome of work done in collaboration with others, except as detailed in the text and specified below. This dissertation contains fewer than 60,000 words including appendices, bibliography, footnotes, tables, and equations, and has fewer than 150 figures.

Chapters 3, 4 and 5 contain work published in:

- [1] E. I. Rodríguez Chiacchio and A Nunnenkamp, *Tuning the relaxation dynamics of ultracold atoms in a lattice with an optical cavity*, Phys. Rev. A 97, 033618 (2018)
- [2] E. I. Rodríguez Chiacchio and A Nunnenkamp, *Emergence of continuous rotational symmetries in ultracold atoms coupled to optical cavities*, Phys. Rev. A 98, 023617 (2018)
- [3] E. I. Rodríguez Chiacchio and A Nunnenkamp, *Dissipation-induced instabilities of a spinor Bose-Einstein condensate inside an optical cavity*, Phys. Rev. Lett. 122, 193605 (2019)

Ezequiel Rodríguez Chiacchio
June 7, 2020

Abstract

Ultracold atomic gases loaded into optical cavities constitute one of the most versatile platforms for the study of out-of-equilibrium dynamics and quantum simulation of many-body systems. In this thesis, we explore these two possibilities, motivated by current state-of-the-art atom-cavity experiments, uncovering novel phenomena and opening up new theoretical and experimental avenues into the intriguing world of quantum many-body physics.

First, we study a gas of ultracold atoms coupled to three optical resonators. We show that the inherent $\mathbb{Z}_2$ symmetries, associated with each atom-cavity coupling, can be combined into a global $SO(3)$ rotational symmetry which can be spontaneously broken. We determine the phase diagram of the system, which shows the emergence and breaking of the continuous symmetries and displays first- and second-order phase transitions. We argue that by coupling the atoms equally to n different modes, it will in general be possible to generate a global $SO(n)$ symmetry.

Second, we investigate the dynamics of a spinor BEC inside an optical cavity. We focus on a two-component Dicke model with complex light-matter couplings, accounting for photon losses. We compute the steady-state phase diagram and find dynamical instabilities in the form of limit cycles, heralded by the presence of exceptional points and level attraction. We show that the instabilities are induced by dissipative processes that generate nonreciprocal couplings between the two collective spins.

Lastly, we explore the dynamics of a BEC inside an optical cavity in the presence of an optical lattice. We derive an effective master equation by adiabatically eliminating the cavity field. In the bad-cavity regime, we find an infinite-temperature steady state, but with relaxation dynamics that can be highly nontrivial. For small hopping, the interplay between dissipation and strong interactions leads to an algebraic relaxation of the system, whereas for large hopping, the approach to the steady state is exponential. In the good-cavity regime, we show that the system allows for optical pumping between momentum modes, enabling cavity cooling.

Acknowledgements

First and foremost, I would like to thank Andreas for giving me the chance to join his group here in Cambridge four years ago. I deeply appreciate all the patience you had with me given my lack of experience in the field and in the art of doing research in theoretical physics. Your continuous support throughout this period has not only been inspiring and encouraging for my academic development, but also ensured I could have an exciting and vibrant life experience during these past years. Thank you for your positivity and trust on my ideas, my questions and on myself. It has been a pleasure to work with you.

I am also grateful for the rest of my team: Matteo, Petr, Andrea, Clara, Bogdan, Simon and Daniel; with whom altogether I have shared countless hours in the coffee area or the seminar room discussing about physics, life and food. I have enjoyed so much working alongside each other and see you grow as researchers on the way. I am excited to see what awaits in the future for all of you.

I want to thank my office mates Stephen and Yang, which made sure we always had a comfortable atmosphere, despite working in a window-less asbestos-filled tiny cell. Thank you for always being there to answer all my random questions. I always look up to you for being filled with so much knowledge.

My time in TCM would by no means have been the same without the presence of Beñat and Joas. They welcomed me in their lives since day one, listened to all my troubles in and out of the academic world, encouraged me to appreciate all the amazing things that happen around me and overall brought loads of happy moments and adventures that I will take with me everywhere I go. On this note I would also like to thank my partner in crime, Chris Parmee, for making all conferences hilarious experiences and for the many hours helping me with work. I hope we get to keep exploring the world together in the coming years. The TCM family is vast and rapidly changing, but I would like to thank each one of you who took a moment to have a conversation with me and allowed me to get to know you a bit more, being it during a break, Friday drinks, Christmas party or the pub. All of you are responsible for a continuous set of great memories in this group.

This is also dedicated to all my Homerton family. I would like to thank Daniel, who has had to put up with me since my second day in Cambridge until today. It has been a great

pleasure to navigate with you the emotional roller coaster that is doing PhD and to share a macroscopic amount of unforgettable moments since we met in Queen's Wing. I would also like to thank Gonzalo for being a constant source of disparate humor, positivity and friendship. Al toque, perro. A great amount of support and companionship during the second half of my time in Cambridge was provided by Ana and Pamela, who did not flicker for a moment to be there for me whenever I needed them. Thanks for being so patient and caring with me. Thank you Charlotte for the endless conversations about life while trashing the kitchen or sipping some tea. I am actually happy I met you. Thank you so much to my other roommates in and out of Homerton: Tim, Sergio, Natasha and Kima. You have in different ways made, and still make, the everyday life a much more joyful experience. I would also like to thank Maite and Luz, for always sporadically reappearing in my life to provide fun, laughter and great moments.

It is fundamental for me to thank all of the dance community in Cambridge, which I am so so grateful to have had a chance to be part of. I would like to thank Ron for sharing his passion for dancing and his commitment to the scene. I would also like to send a big shout out to the break dance society family for providing a fun and friendly environment to dance during my first year. Most importantly, I would like give a massive thank you to my Street Dance Team, including every single person who has been a part of it during the past three years. This team has been my family and together we have been through a lot more than words can possibly express. I am constantly amazed at how fast you all learn, progress and strive. You have been, are, and will always be a source of inspiration to me. Lastly, among the many incredible dancers that I have come across these past years, I am indebted to Simon and Ani for making my journey so special. I am grateful for all the patience, constructive feedback, support, encouragement and trust I have received from you. Thanks for always pushing me to keep challenging myself and giving my best every time.

Another beautiful aspect of my Cambridge life has been performing alongside some its most talented musicians. Thanks to all the members of Syzygie for allowing me to be part of this crazy project. It has been amazing to experience all the different sides of the Cambridge musical scene with you.

I want to thank Sofia for her company during the past year and a half. Through you I have been able to experience the world and appreciate its beauty from a different perspective. Thank you for all the adventures, the laughter, the support and the love.

I would like to thank my family for being there for me every time I needed it. Thanks to my younger siblings for reminding me of what it means to evolve and mature and to always accept me for who I am. Thanks to my dad for sharing his life experiences, his

wisdom, his passions and for his love. A very special mention goes to my mum, the person I grew up with and who provided everything for my mental and emotional development. You never hesitated to make every single effort you possibly could to construct a brighter future for me. Against all odds, I ended up studying in Cambridge, something that neither of us would have ever dreamed of back when we lived in Mendoza. This is all a result of your continuous support, trust and love. Te quiero mamá, muchas gracias por creer siempre en mi.

Last but not least, I want to dedicate the work in this thesis to my aunt, Pieri, my uncles, Duilio and Favio, and my grandfather, Juan Andrés. This all started when you challenged yourselves to teach advanced mathematical concepts to a six years old kid. The interest and love for math and science I inherited from you is one of the most wonderful gifts I have ever received. Thanks for teaching me to observe and question everything around me. Los quiero mucho, gracias por todo el amor.

Contents

1

Introduction

Light-matter interactions play a central role in the way we perceive, comprehend and communicate with our environment. These give rise to colors, shadows, brightness, opacity, and many other properties that we assign to our environment, based on the way it interacts with light. The formulation of Maxwell's equations in 1862 constituted a major step in the understanding of this phenomenon, by explaining how electromagnetic waves propagate through space. Deeper insight arrived decades later with the advent of quantum theory, which re-established the notion that light can also be understood in terms of finite energy packages or particles, called photons.

Quantum mechanics not only allowed to explain remarkable phenomena such as the photoelectric effect, but also forged the foundational ideas for the manipulation of light. At the pinnacle of this stands the invention of the laser, which revolutionized the technological world and opened the door to a new generation of experimental platforms in physics. Two paradigmatic examples are the development of laser cooling and atomic traps, which earned Steven Chu, Claude Cohen-Tannoudji and William Daniel Phillips the Nobel prize in 1997 [4–6]. This advancement in turn led to the generation of the first atomic Bose-Einstein Condensate which also resulted in Eric Cornell, Carl Wieman and Wolfgang Ketterle receiving the Nobel prize in 2001 [7, 8]. The achievement of ultra low temperatures using laser cooling provided the opportunity to explore the behavior of quantum matter in an highly controlled environment [9], given by the interaction between atoms and light.

In the following decade, this possibility gave birth to a new field of research interested in exploiting this exquisite control to simulate quantum phenomena using cold atom experiments [10]. This goes under the name of quantum simulation. This concept emerged from the difficulty in studying macroscopic systems computationally, using the currently

available technological tools. The main obstacle is the size of the Hilbert space, which grows exponentially with the number of components in the system, exceeding the capacity of computational power very fast. In this sense, experiments with quantum gases can act as simulators for macroscopic systems by manipulating the set-up in such a way that it realizes a particular model one is interested in studying. A particularly successful example constitutes the trapping of ultracold atoms in optical lattices [11], offering the possibility to study a wide variety of tight-binding models. Examples include the realization of strongly interacting states of matter [12–14], topological phenomena [15–17], or many-body localization [18]. Nowadays, quantum simulation is an ongoing and very active research area, present in other experimental platforms such as trapped ions [19], superconducting circuits [20] or photonic crystals [21].

In spite of these advances relying on the use of lasers to trap and control the atoms, light plays a passive role in these systems, acting as a fixed background for the atoms. This situation is drastically changed if atoms are placed inside optical cavities [22]. In these set-ups, photons make several round trips between the two mirrors before being scattered away of the system. This enhances the effective light-matter coupling and allows for the atoms to back act of the dynamics of the light field. The study of electromagnetic fields trapped within confined spaces is usually referred to as cavity quantum electrodynamics or cavity QED. An additional, and unavoidable, feature of this type of systems is the presence of photon losses due to imperfections in the cavity mirrors, meaning that cavity QED platforms are intrinsically open quantum systems. Excitingly, this dissipation channel can be exploited to monitor the system in situ by placing a photodetector at one of the cavity mirrors. This allows to perform measurements on the system without having to modify or destroy it. For these reasons, optical cavities have become strong candidates for quantum simulation.

The idea of placing Bose-Einstein condensates inside optical cavities was born with the intention of expanding the quantum simulation toolbox to models containing long-range interactions, mediated by cavity photons. This was experimentally conceived for the first time in 2010 by K. Baumann et al. at ETH Zurich [23]. They showed that the influence of long-ranged interactions contributed to the presence of a self-organization phase transition in which a crystal of light and matter emerges. This work has since become the foundation for a myriad of studies using atom-cavity systems to perform quantum simulation of more complex phenomena. These directions include multimode cavities [24, 25], optical lattices [26, 27], multiple cavities [28–30] and spinor BEC's [31–33], among others [22].

The aim of this thesis is to explore new possibilities for atom-cavity systems as simulators of complex quantum phenomena, and to investigate the impact of dissipation on

the dynamics of these systems. The former is motivated by the arguments presented above, with the results of our work enlarging the quantum simulation toolbox. The latter arises from the need to fully characterize the system, as dissipative processes unavoidably affect the dynamics beyond a certain timescale. This question is very timely as, in contrast to their closed system counterparts, open quantum systems remain far less well-understood. Thus, it is not a priori clear what kind of effects, properties or phases can emerge in these settings. It is then of vital importance to address this issue in order to be capable of characterizing and predicting novel phenomena in quantum many-body systems. Our work contributes to this goal by analyzing two relevant physical examples (spinor Bose-Einstein condensates and Bose-Hubbard models) and uncovering exciting phenomena resulting from the effects of dissipation.

1.1 Thesis outline

In this thesis we explore the physics of ultra-cold atomic gases interacting with light fields confined to optical cavities. Chapters 1 and 2 correspond to introductory concepts and tools needed to study the physics of these systems and Chapters 3 to 5 discuss the original work carried out as part of the PhD programme.

In this chapter, we explore the fundamental concepts behind light-matter interaction between atoms and cavity fields. We generalize this to the case where a quantum gas, formed by a macroscopic amount of atoms, interacts with a cavity mode and derive an effective model to describe this system. We then take an intermezzo to describe in detail the main features of this model, as they will be highly relevant for the all the work described in this thesis, and in particular for the systems considered in Chapters 3 and 4. We also provide a physical interpretation of these features in terms of the atomic and cavity degrees of freedom, which are the relevant quantities for experimental studies. We close this chapter by including the effects of optical lattices and derive the effective model we will consider in Chapter 5. In Chapter 2, we introduce the formalism of open quantum systems from the point of view of Markovian Lindblad master Equations, which will be pivotal for the study of out-of-equilibrium dynamics in Chapters 4 and 5.

In Chapter 3, we consider a quantum gas interacting with multiple optical cavities. We show that in certain parameter regimes, the effective model describing this system can exhibit different continuous symmetries. We compute the ground-state phase diagram and discuss its implications on the real space configuration of the atomic cloud. We argue that for n modes coupled to the atomic cloud in the same fashion it is possible to simulate the symmetry breaking of continuous rotational symmetries $SO(n)$. This

work was published in [2]. In Chapter 4, we instead consider the interaction of a spinor Bose-Einstein condensate with the single mode of an optical cavity. By introducing a misalignment between the polarizations of an external drive and the cavity we obtain non-reciprocal interactions between the atomic species mediated by the cavity photons. We investigate the system dynamics, and discover the presence of a previously unobserved instability, which is generated by photon loss processes. This was published in [3]. The work presented in Chapter 5, published in [1], concerns the physics of a quantum gas placed on a two-dimensional optical lattice and interacting with a single cavity mode. In this work we develop an effective model solely in terms of atomic degrees of freedom by adiabatically eliminating the cavity photons and analyze the possible steady-states and relaxation dynamics in different parameter regimes. We identify two different relaxation regimes. The first one corresponds to a diffusive approach to the steady-state, emerging when the gas is strongly interacting, and where type of diffusion is given by the interplay between short- and long-ranged interactions. The second one occurs when the short-ranged interactions are negligible and results in an exponential decay towards the steady-state. Lastly, concluding remarks are provided in Chapter 6.

Throughout the thesis, we work in units where $\hbar = 1$ and $c = 1$.

1.2 Light-matter interaction in a cavity

In this section we introduce the two main characters in this thesis: atoms and confined light fields. We start by describing the interaction between a single atom and a single cavity mode and introduce the well-known dispersive limit, corresponding to the parameter regime in which we will be operating throughout this thesis. Using these tools, we then construct a many-body Hamiltonian for the interaction between a Bose-Einstein Condensate (BEC) and the single-mode of an optical cavity. This model forms the basis for what will be discussed in this work. Next, we present a brief summary of the physics of an archetypal model in quantum optics known as the *Dicke model* [34]. As we will show below, this model provides a very useful framework to describe the low-energy manifold of a BEC interacting with a cavity mode, and in particular, is able to capture the physics behind the *self-organization* phase transition that takes place in this system [23].

1.2.1 A single atom in a cavity

Our starting point consists of an atom trapped inside a high-finesse Fabry-Perot resonator with the assumption that it only interacts with a specific mode of the resonator. All

the different modes supported by the resonator can be obtained by solving the paraxial Helmholtz equation. These solutions are periodic in the longitudinal direction, corresponding to the cavity axis. In the transverse plane, they are instead described by the Hermite-Gauss polynomials. This transverse structure of the modes leads to the nomenclature $\mathrm{TEM}_{n,m} \equiv$ *Transverse Electromagnetic Modes*, with (n, m) specifying the precise transverse structure defined by the Hermite-Gauss polynomials. For simplicity, we will consider the atom to be coupled to the so-called fundamental mode $\mathrm{TEM}_{0,0}$. In the transverse plane, the $\mathrm{TEM}_{0,0}$ mode has a Gaussian structure, whose width we will consider to be much larger than the size of the region where the atom is trapped. This allows us to drop the spatial dependence along the transverse plane and focus only on the effects along the longitudinal axis.

The interaction between an atom and an electromagnetic field can be captured within the electric dipole approximation, leading to an interaction Hamiltonian of the form

$$\hat{H}_{\mathrm{int}} = -\hat{\vec{d}} \cdot \hat{\vec{E}}, \tag{1.1}$$

where $\hat{\vec{E}}$ is the electric field inside the cavity and $\hat{\vec{d}}$ corresponds to the dipole operator of the atom. In general, the dipole operator for a multi-level atom is defined

$$\hat{\vec{d}} = \sum_{i,k} \left(\vec{d}_{i,k} |i\rangle\langle k| + \vec{d}_{k,i} |k\rangle\langle i| \right), \tag{1.2}$$

with $|i\rangle$ the energy levels of the atom and $\vec{d}_{i,k} = \langle i|\hat{x}|k\rangle$ the spatial overlap between the energy levels and the atomic position $\hat{x}$. By modifying the geometry of the resonator, e.g. varying the length of the cavity, it is possible to control the natural frequency of the light modes, allowing one to tune it close to resonance with respect to a specific atomic transition. With this in mind, the first simplification we introduce in our model is the assumption that the atom is effectively well described by only two relevant energy levels, namely, a ground state $|g\rangle$ and an excited state $|e\rangle$ with a level splitting of frequency ω_{at}. In this basis, the atom can be parametrized using the Pauli matrices, with $\hat{\sigma}_z = (|e\rangle\langle e| - |g\rangle\langle g|)/2$, $\hat{\sigma}_+ = |e\rangle\langle g|$ and $\hat{\sigma}_- = |g\rangle\langle e|$. The dipole operator then acquires the form $\hat{\vec{d}} = \vec{d}\hat{\sigma}_- + \vec{d}^*\hat{\sigma}_+$. On the other hand, the electromagnetic field for the cavity mode is given by

$$\hat{\vec{E}} = E_{\mathrm{c}} \sqrt{\frac{\omega_c}{V\varepsilon_0}} \cos\left(\vec{k}_{\mathrm{c}} \cdot \hat{\vec{x}}\right) \left(\vec{\epsilon}\, \hat{a} + \vec{\epsilon}^*\, \hat{a}^\dagger \right), \tag{1.3}$$

where E_{c} is the amplitude of the field, ω_c the frequency of the cavity mode, V the mode volume, defined as the cross section of the optical beam times the length of the cavity, and $\vec{k}_{\mathrm{c}}$ the cavity wave vector. The operators $\hat{a}^\dagger$ and $\hat{a}$ correspond to bosonic operators,

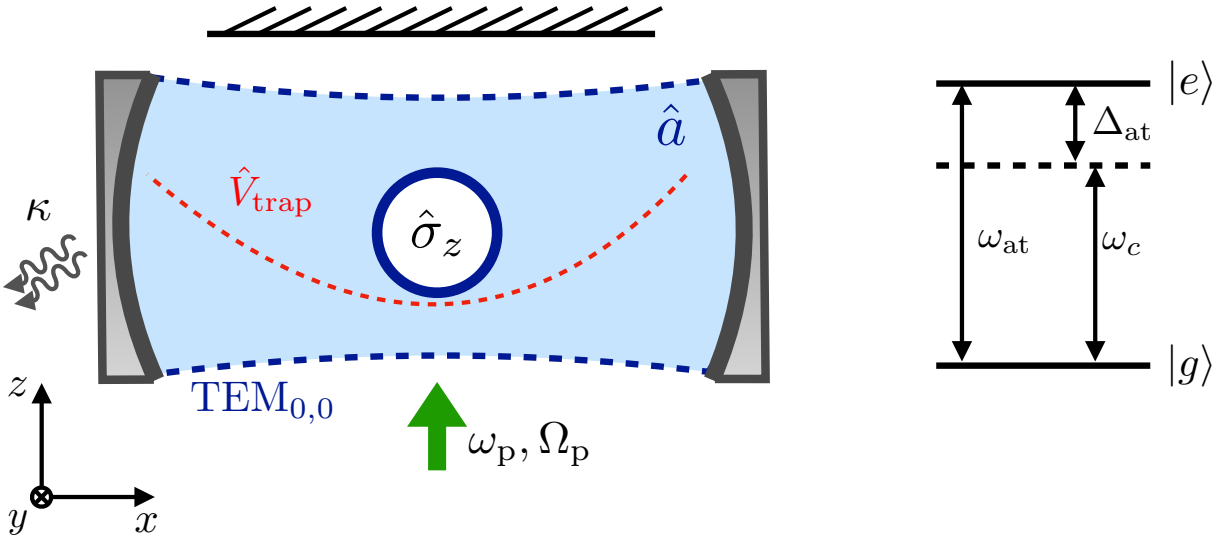

Figure 1.1: Schematic depiction of the model presented in (1.4). A two level system $\hat{\sigma}_z$ with frequency ω_{at} is placed inside an optical cavity under a trapping potential $\hat{V}_{\text{trap}}$. The atom interacts with the $\text{TEM}_{0,0}$ quantized mode of the cavity, represented by the bosonic operators $\hat{a}$ and $\hat{a}^\dagger$, with frequency ω_c. Photons can escape the cavity at a rate κ. Moreover, the system is transversely driven by an external laser with frequency ω_{p} and amplitude Ω_{p}.

obeying $[\hat{a}, \hat{a}^\dagger] = 1$, which create and annihilate photons inside the cavity. Lastly, the vector $\vec{\epsilon}$ corresponds to the polarization vector of the field satisfying $|\vec{\epsilon}|^2 = 1$. With these definitions we can now write an effective Hamiltonian for the coupled atom-cavity system of the form

$$\hat{H} = \frac{\hat{\vec{p}}^2}{2m} + \hat{V}_{\text{trap}} + \omega_{\text{at}}\hat{\sigma}_z + \omega_{\text{c}}\hat{a}^\dagger\hat{a} + g(\hat{\vec{x}})\left(\hat{a} + \hat{a}^\dagger\right)(\hat{\sigma}_- + \hat{\sigma}_+)\,, \tag{1.4}$$

where we introduced the light-matter coupling $g(\hat{\vec{x}}) = g_0 \cos(\vec{k}_{\text{c}} \cdot \hat{\vec{x}})$, with $g_0 = \sqrt{\frac{\omega}{V\varepsilon_0}}\vec{\epsilon} \cdot \vec{d}$, and we took both $\vec{\epsilon}$ and $\vec{d}$ to be real. The first term in the Hamiltonian corresponds to the kinetic energy of the atom, with $\vec{p}$ the momentum operator and m the mass of the atom, and the second one to an external trapping potential. The third and fourth terms are associated with the internal levels of the atom and the cavity photons, respectively, and the last term with the light-matter interaction, resulting from the dipole approximation. This interaction allows for two type of scattering processes: number conserving, corresponding to $\hat{a}^\dagger\hat{\sigma}_-$ and $\hat{a}\hat{\sigma}_+$, in which a photonic excitation is exchanged by an atomic transition or vice versa; and number non-conserving, corresponding to $\hat{a}^\dagger\hat{\sigma}_+$ and $\hat{a}\hat{\sigma}_-$, where photon and atomic excitations can be simultaneously created or destroyed.

In a rotating frame with respect to $\hat{H}_0 = \omega_{\text{c}}\hat{a}^\dagger\hat{a} + \omega_{\text{at}}\hat{\sigma}_z$, the number conserving terms evolve as $\hat{a}^\dagger\hat{\sigma}_- e^{i(\omega_{\text{at}}-\omega_{\text{c}})} + \hat{a}\hat{\sigma}_+ e^{-i(\omega_{\text{at}}-\omega_{\text{c}})}$, while the non-conserving terms obey $\hat{a}^\dagger\hat{\sigma}_+ e^{i(\omega_{\text{at}}+\omega_{\text{c}})} +$

$\hat{a}\hat{\sigma}_- e^{-i(\omega_{\rm at}+\omega_{\rm c})}$. This means that for $|\omega_{\rm at}-\omega_{\rm c}| \ll \omega_{\rm at}+\omega_{\rm c}$, the non-conserving terms will rotate at a much faster rate than the conserving terms. Consequently, they have a much weaker imprint on the dynamics of the system. Hence, we neglect these terms. This procedure is known as *Rotating Wave Approximation* (RWA), and it works best in the limit of small coupling[1] $g_0 \ll (\omega_{\rm at}, \omega_{\rm c})$. As a result of this approximation, we arrive at

$$\hat{H} = \frac{\hat{\vec{p}}^2}{2m} + \hat{V}_{\rm trap} + \omega_{\rm at}\hat{\sigma}_z + \omega_{\rm c}\hat{a}^\dagger\hat{a} + g(\hat{\vec{x}})\left(\hat{a}\hat{\sigma}_+ + \hat{a}^\dagger\hat{\sigma}_-\right), \tag{1.5}$$

where the Hamiltonian now conserves the number of excitations. Ignoring the external degrees of freedom of the atom, this Hamiltonian goes under the name of Jaynes-Cummings model and is arguably one the most fundamental models describing light-matter interaction [35]. Instead of delving into the physics of this paradigmatic Hamiltonian, we will explore the case when the system is coherently driven by an external classical pump which is far detuned from the atomic transition frequency $\omega_{\rm at}$. This is known as the *dispersive regime*.

The dispersive regime

We now include in our model the presence of an external coherent pump which drives the system periodically with frequency $\omega_{\rm p}$, see Fig. 1.1. Typically, in atom-cavity systems we are interested in two types of pumping, side pumping, where the cavity mode is being driven, or transverse pumping, where the atomic transitions are being driven. In our case, we will focus on the latter. In particular, we will consider the cavity axis to be pointing along the x axis and the pump along the z axis. For a two-level atom, the effects of transverse pumping can be incorporated in our Hamiltonian through the term

$$\hat{H}_{\rm pump} = \Omega(\hat{z})(\hat{\sigma}_- e^{i\omega_{\rm p}t} + \hat{\sigma}_+ e^{-i\omega_{\rm p}t}), \tag{1.6}$$

with $\Omega(\hat{z}) = \Omega_p \cos(k_{\rm p}\hat{z})$, where Ω_p is the Rabi frequency and $k_{\rm p} = |\vec{k}_{\rm p}|$ the modulus of the pump wavevector. Note that this introduces an undesired time dependence in our Hamiltonian. Such dependence can be removed by moving into a frame rotating at the pump frequency, given by the transformation $\hat{U} = e^{i\omega_{\rm p}(\hat{a}^\dagger\hat{a}+\hat{\sigma}_z)t}$, leading to

$$\hat{H} = \frac{\hat{\vec{p}}^2}{2m} + \hat{V}_{\rm trap} - \Delta_{\rm at}\hat{\sigma}_z - \Delta_{\rm c}\hat{a}^\dagger\hat{a} + g(\hat{x})\left(\hat{a}\hat{\sigma}_+ + \hat{a}^\dagger\hat{\sigma}_-\right) + \Omega(\hat{z})(\hat{\sigma}_- + \hat{\sigma}_+), \tag{1.7}$$

[1] In the context of Rb atoms inside optical cavities, this is well justified as $g_0 \sim$ MHz while both the cavity frequency and level splitting satisfy $(\omega_{\rm c}, \omega_{\rm at}) \sim$ THz.

where $\Delta_c = \omega_p - \omega_c$ and $\Delta_{at} = \omega_p - \omega_{at}$ are the cavity and atomic detunings respectively. For the reminder of this work, we will consider the pump to be red-detuned from both the atomic transition and the cavity frequency, meaning $(\Delta_{at}, \Delta_c) < 0$. We proceed by using Eq. (1.7) to compute the equations of motion in the Heisenberg picture. This yields

$$\begin{aligned}
\partial_t \hat{a} &= i\Delta_c \hat{a} - ig_0 \cos(k_c \hat{x})\hat{\sigma}_- \\
\partial_t \hat{\sigma}_- &= i\Delta_{at}\hat{\sigma}_- + i2g_0 \cos(k_c \hat{x})\hat{a}\hat{\sigma}_z + i2\Omega_p \cos(k_p \hat{z})\hat{\sigma}_z \\
\partial_t \hat{\sigma}_z &= -ig_0 \cos(k_c \hat{x})(\hat{a}\hat{\sigma}_+ - \hat{a}^\dagger \hat{\sigma}_-) \\
\partial_t \hat{x} &= \frac{\hat{p}_x}{m} \qquad\qquad \partial_t \hat{z} = \frac{\hat{p}_z}{m} \\
\partial_t \hat{p}_x &= i[\hat{V}_{trap}, \hat{p}_x] + g_0 k_c \sin(k_c \hat{x}) \left(\hat{a}\hat{\sigma}_+ + \hat{a}^\dagger \hat{\sigma}_-\right) \\
\partial_t \hat{p}_z &= i[\hat{V}_{trap}, \hat{p}_z] + \Omega_p k_p \sin(k_p \hat{z}) \left(\hat{\sigma}_- + \hat{\sigma}_+\right).
\end{aligned} \tag{1.8}$$

Let us now focus on the limit when the pump is far detuned from the atomic transition, meaning $\Delta_{at} \gg (\Delta_c, g_0, \eta)$, known as the dispersive regime. In this limit, the probability for the atom to go through a transition into the excited state is strongly suppressed, resulting in the atom mostly remaining in the ground state. Thus, we can adiabatically eliminate the excited state of the atom by approximating $\hat{\sigma}_z \approx -\frac{1}{2}$ and taking $\partial_t \hat{\sigma}_- = 0$, resulting in $\hat{\sigma}_- = \frac{g(\hat{x})}{\Delta_{at}}\hat{a} + \frac{\Omega(\hat{z})}{\Delta_{at}}$. Substituting this expression into the equation of motion for the other operators, we obtain a set of expressions than can be traced back into an effective Hamiltonian [36]

$$\begin{aligned}
\hat{H} = \frac{\hat{\vec{p}}^2}{2m} + \hat{V}_{trap} - \Delta_c \hat{a}^\dagger \hat{a} + \frac{g_0^2}{\Delta_{at}} \cos^2(k_c \hat{x})\hat{a}^\dagger \hat{a} + \frac{\Omega_p^2}{\Delta_{at}} \cos^2(k_p \hat{z}) \\
+ \frac{g_0 \Omega_p}{\Delta_{at}} \cos(k_c \hat{x}) \cos(k_p \hat{z})(\hat{a} + \hat{a}^\dagger).
\end{aligned} \tag{1.9}$$

We have now obtained an effective picture in which the interaction between the atom and the cavity photons is given by virtual transitions to the excited state, hence why the Δ_{at}^{-1} dependence in the interaction terms. Notice also that now the light field is only coupled to the external degrees of freedom of the atom. Let us now examine in more detail the resulting effective interaction, corresponding to the last three terms in Eq. (1.9). The first one is proportional to the photon number operator $\hat{a}^\dagger \hat{a}$ and corresponds to a dielectric shift of the cavity frequency due to the presence of the atom. This reveals that even a single atom can act as a dielectric medium inside an optical resonator. On the other hand, this term can also be understood as a lattice potential along the cavity axis acting on the atom, which is dependent on the number of photons present in the cavity. Analogously, the second one corresponds to a lattice potential along the z direction, generated by the

external pump. Lastly, the third term is associated with two-photon scattering processes between the pump and the cavity field, mediated by the atom and depending on its position. One can also understand this term as an effective 2D potential felt by the atom when the cavity occupies a coherent state $\hat{a}|\alpha\rangle = \alpha|\alpha\rangle$. As we will see in the next section, when considering the many-body case in the ultra-cold regime, this last term is responsible for the emergence of a quantum phase transition, defining two different macroscopic behaviors, one in which the system remains in a superfluid state and another in which the system spontaneously self-organizes in real space.

Before proceeding to add the next layer of complexity to our model, a few remarks regarding the considerations made in this section are due. First, the way adiabatic elimination was carried out above was a rather crude procedure. In general, tracing out degrees of freedom requires a more careful treatment. This will be discussed more rigorously at the beginning of Chapter 2, where we will describe a generic method to adiabatically eliminate degrees of freedom and obtain a physically well-defined and meaningful description. Nevertheless, the approximations used above can provide a qualitative picture for understanding the physics of the system in this parameter regime. Finally, it is also important to remark that we have not included the effects of dissipative processes in our model. Typical dissipation sources include atom loss, spontaneous emission and photon loss through the cavity mirrors. In particular, photon losses will be the main dissipation channel that we will consider in the remainder of this work. For the moment, dissipation will be included phenomenologically in our equations of motion. Nevertheless, in Chapter 2 we will introduce the formalism of Lindblad master equations, which will allows us to rigorously account for the presence of dissipative process in the dynamics of the system.

1.2.2 A BEC in a cavity

We now consider the case of N atoms inside an optical cavity. In typical experiments, this number is usually of order $N \sim 10^5$. Moreover, we will consider the system to be at a sufficiently low temperature such that atoms are forming a Bose-Einstein condensate (BEC), meaning that they are all macroscopically occupying the same single-particle state. In this context, by sufficiently low temperature T, we mean that $T \ll \omega_{\mathrm{r}}$, where $\omega_{\mathrm{r}} = \frac{k_{\mathrm{p}}^2}{2m}$ is the recoil frequency of the atoms inside the cavity, given by the momentum k_p imparted by pump photons. Using the result derived in Eq. (1.9) we define the many-body

Hamiltonian

$$\hat{H} = -\Delta\hat{a}^\dagger\hat{a} + \int d\vec{x}\Bigg[\hat{\Psi}^\dagger(\vec{x})\Bigg(\frac{\vec{p}^2}{2m} + \hat{V}_{\text{trap}} + U_0\cos^2(k_c x)\hat{a}^\dagger\hat{a} + V_0\cos^2(k_p z) + \eta\cos(k_c x)\cos(k_p z)(\hat{a}+\hat{a}^\dagger)\Bigg)\hat{\Psi}(\vec{x}) + \frac{\alpha_s}{2}\hat{\Psi}^\dagger(\vec{x})\hat{\Psi}^\dagger(\vec{x})\hat{\Psi}(\vec{x})\hat{\Psi}(\vec{x})\Bigg], \tag{1.10}$$

where we have introduced the creation and annihilation field operators $\hat{\Psi}^\dagger(\vec{x})$ and $\hat{\Psi}(\vec{x})$ for the atoms, and the parameters $U_0 = g_0^2/\Delta_{\text{at}}$, $V_0 = \Omega_p^2/\Delta_{\text{at}}$ and $\eta = g_0\Omega_p/\Delta_{\text{at}}$. Note that we have dropped the subscript in the cavity the detuning, as for the rest the discussion this will be the only detuning we consider. The last term in this expression accounts for contact interaction between atoms, with strength α_s. This Hamiltonian was the starting point of the first experimental realization of a BEC in a cavity [23]. In principle, this corresponds to an interacting many-body problem between two bosonic fields, intrinsically not fully solvable. However, it is possible to obtain an accurate minimal picture of the physics by performing suitable approximations. The first one will be to ignore the effects of short-range interactions between the atoms, assuming that the effective interaction strength is weaker than the rest of energy scales in the system. The second and most important one will be considering that the pump strength, encoded in η, is small enough such that we can consider only the low-energy manifold to play a significant role in the dynamics of the system. Given that the cavity mode only couples to the external degrees of freedom of the atoms, by low-energy manifold of the system, we refer to the lowest momentum states the atoms can occupy and which allow to minimally capture the effects of scattering processes with the cavity field. In the remainder, we will choose the pump wavevector to match that of the cavity and we will use the notation $k_p = k_c = k$.

In the non-interacting case, the atoms form a condensate in the lowest momentum state available from the standing-wave potential generated by the transverse pump. We will consider this to be our zero-point energy. Next, we need to analyze the effects of photon scattering with the cavity field. The interaction via the AC Stark shift does not result in momentum transitions for the atoms, and simply shifts the cavity detuning. On the other hand, momentum transitions do occur when photons are scattered from the pump into the cavity, and vice versa, by interacting with the atoms. When an atom absorbs a photon from the pump, it virtually enters its excited state while getting a momentum kick in the $(\pm)z$ direction. This photon is then almost instantaneously emitted into the cavity, resulting in the return of the atom into its ground state and the gain of another momentum kick, now in the $(\pm)x$ direction. Taking into account all the possible directions in which

this process can happen, we see that these two-photon scattering processes couple the BEC state $|0,0\rangle$ with the momentum states $|\pm k_x, \pm k_z\rangle$, with $|k_x| = |k_z| = k$ and energy $E = 2\omega_\mathrm{r}$. Assuming that the energies associated with higher momentum states in the band defined by the standing-wave potential of the pump are much higher than ω_r, we restrict our low-energy manifold to two states: the BEC state $|0,0\rangle$, and the symmetric linear combination of the excited momentum states $|k\rangle = \sum_{\sigma,\sigma'=\pm} |\sigma k_x, \sigma' k_z\rangle$. This truncation is sometimes denoted as the *single recoil limit*, as we consider only the first excited state due to the recoil from atom-photon scattering process. This is shown schematically in Fig. 1.2. This simplification allows us to construct an ansatz for the atomic field operator of the form

$$\hat{\Psi}(x,z) = \frac{1}{\sqrt{V}}\hat{b}_0 + \frac{2}{\sqrt{V}}\cos(kx)\cos(kz)\hat{b}_1, \tag{1.11}$$

where V is the volume of the system, $\hat{b}_0$ is the annihilation operator for atoms in the BEC and $\hat{b}_1$ the annihilation operator for atoms in the excited momentum state $|k\rangle$, both satisfying bosonic commutation relations $[\hat{b}_i, \hat{b}_j^\dagger] = \delta_{i,j}$ and the constraint $\hat{b}_0^\dagger\hat{b}_0 + \hat{b}_1^\dagger\hat{b}_1 = N$. Note that the cosine-like spatial structure of the excited states results from the linear combination of propagating planar waves in the four different directions $\pm x$ and $\pm z$. Inserting this ansatz into Eq. (1.11) and carrying out the integration we arrive at

$$\hat{H} = \left(-\Delta + \frac{U_0 N}{2}\right)\hat{a}^\dagger\hat{a} + \omega_0\hat{b}_1^\dagger\hat{b}_1 + \frac{\lambda}{\sqrt{N}}\left(\hat{a}^\dagger + \hat{a}\right)\left(\hat{b}_1^\dagger\hat{b}_0 + \hat{b}_0^\dagger\hat{b}_1\right) + U_0 M\hat{b}_1^\dagger\hat{b}_1\hat{a}^\dagger\hat{a}, \tag{1.12}$$

where $\omega_0 = 2\omega_\mathrm{r}$, $\lambda = \frac{\eta N}{2}$ and $M = \frac{3}{4}$ is a numerical factor resulting from the overlap of the cosine functions. The Stark shift term produces two different terms. The first one corresponds to a shift of the cavity frequency, proportional to the number of atoms, and the second to an interaction between the photon number and the number of atoms in the excited state. For the rest of our discussion, we will in general consider the majority of the atoms to be populating the BEC and thus we neglect the last term in Eq. (1.12). As a final step, we make use of the Schwinger transformation to map the two atomic bosonic operators $\hat{b}_{0,1}$ into collective spin operators $\hat{J}_z = \frac{\hat{b}_1^\dagger\hat{b}_1 - \hat{b}_0^\dagger\hat{b}_0}{2}$, $\hat{J}_+ = \hat{b}_1^\dagger\hat{b}_0$ and $\hat{J}_- = \hat{b}_0^\dagger\hat{b}_1$. This leads to

$$\hat{H} = -\Delta\hat{a}^\dagger\hat{a} + \omega_0\hat{J}_z + \frac{\lambda}{\sqrt{N}}\left(\hat{a}^\dagger + \hat{a}\right)\left(\hat{J}_+ + \hat{J}_-\right), \tag{1.13}$$

where we absorbed the dispersive shift into the definition of the cavity detuning and neglected a constant shift. This resulting Hamiltonian corresponds to the well-known Dicke model, which describes the interaction between a bosonic field ($\hat{a}$) and a collective spin ($\hat{\vec{J}}$) of length $\frac{N}{2}$. We will show that the Dicke model suffices as a minimal model capable of capturing the presence of a phase transition in our system, and the departure

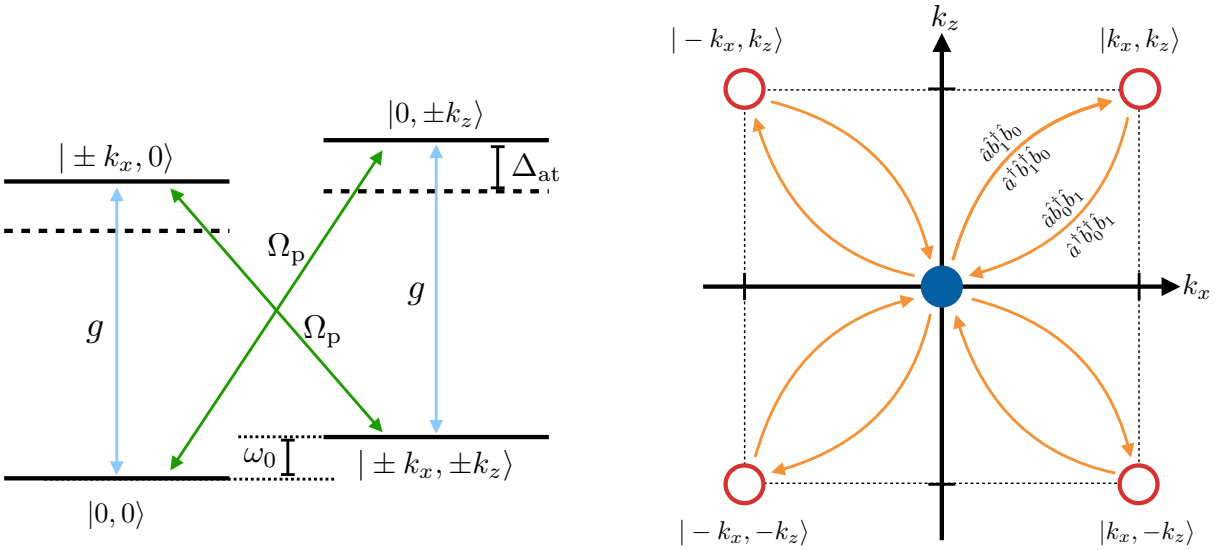

Figure 1.2: Schematic representation of the momentum transitions of the atoms generated by interacting with pump and cavity photons, adapted from Ref. [23]. On the left, level scheme for the transitions. From the BEC state $|0, 0\rangle$ the atom scatters either a pump (green arrows) or a cavity (light blue arrows) photon and virtually transitions to its excited state with a momentum excitation along the x or the z direction, see Fig. 1.1 for reference. The atom then leaves this virtual state by scattering a second photon, thus entering the $|\pm k_x, \pm k_z\rangle$ state, corresponding to carrying a momentum excitation in each spatial direction. On the right, the effective channels resulting from the two-photon Raman scattering in momentum space. On the top right corner we include the second quantization interaction terms that lead to the transitions into the excited momentum state and those that lead to the return into the BEC.

of a macroscopic population of the BEC, due to interactions with the light field. In the next section, we proceed to provide a short description of the main properties of the Dicke model and elaborate on the presence of a so-called *superradiant* phase transition and its interpretation as a spatial self-organisation for the atoms inside the cavity.

1.3 *Intermezzo*: The Dicke model

In this section, we take a brief detour from our main discussion regarding atoms inside a cavity, and instead focus on the effective model we just derived: the Dicke model. This model will be central for the rest of the work presented in this thesis, and when not explicitly treated, we will draw important analogies with it.

The so-called Dicke model was first described by Dicke in 1954 [34]. In his work, Dicke considered an ensemble of two-level atoms occupying their respective excited state and coupled to an electromagnetic field. He found that if the atoms were placed within a

fraction of a wavelength of the electromagnetic field, they could go through a collective relaxation process in which the intensity of the emitted photons was enhanced by a factor of N, being the N the number atoms, with respect to the single-particle emission intensity. This *transient* collective process was later dubbed *superradiance*, or superradiant emission.

Decades later, separately, Hepp and Lieb [37] and Wang and Hioe [38] focused on this model from a different perspective. Namely, they studied the steady-state properties of this model when the two-level atoms were coupled to a quantized electromagnetic mode, such as the ones present inside optical cavities. Their findings were that this model exhibited two different phases: one phase in which the atoms occupy their ground-state while the photonic field is in its vacuum state, which we will denote *normal phase*; and a second phase in which the atoms partially occupy their excited state, signalling a finite number of photonic excitations, which grows linearly with N. This phase corresponds to what we denote today as the *superradiant phase*, and the transition between these two phases is known as *superradiant phase transition*. In both these works, the system was taken to be at finite temperature T, making these phase transition classical. However, it has been shown that this transition does survive in the limit $T \to 0$ [39]. Moreover, this is the regime that will be considered throughout the rest of the thesis.

Here we will introduce a few key concepts and distinguishing features of this model which will be useful for the coming chapters. In particular, we will make emphasis on the presence of the superradiant phase transition both for the ground state, when the system is closed, and in the steady state, when the system is open. One last important remark is that we will be in general interested in focusing on the case of large N, i.e. the thermodynamic limit, as in real experiments $N \sim 10^5$. The Dicke model turns out to be particularly amenable in this limit, as it has been shown that in the thermodynamic limit all of its properties can be captured using the mean-field approximation [39].

Symmetries

Before jumping onto discussing the phase diagram of the Dicke model, it is vital that we point out one of the fundamental aspects of this model, namely, its symmetries. If we look at the Hamiltonian (1.13), it is straightforward to see that it remains invariant under the transformation

$$\left(\hat{a}, \hat{a}^\dagger, \hat{J}_-, \hat{J}_+\right) \to -\left(\hat{a}, \hat{a}^\dagger, \hat{J}_-, \hat{J}_+\right). \tag{1.14}$$

This corresponds to a $\mathbb{Z}_2$ symmetry. This symmetry is associated with invariance under the action of the operator $\hat{\mathcal{U}} = e^{i\pi\hat{\mathcal{N}}}$, where the operator $\hat{\mathcal{N}} = \hat{a}^\dagger\hat{a} + \hat{J}_z$ counts the number

of excitations in the system. Note that $\hat{\mathcal{U}}$ is a parity operator. This means that the Dicke Hamiltonian conserves the parity of the number of excitations, defining two disjoint sectors in the Hilbert space where the number of excitations is either even or odd. The spontaneous breaking of this symmetry leads to the aforementioned phase transition. In the symmetry broken phase, this results in a pair of degenerate ground states, connected by the action of $\hat{\mathcal{U}}$ on them.

1.3.1 Closed system

It is easiest tounderstand the physics of the Dicke model by considering first the case where the physics is dictated purely by the Hamiltonian presented in Eq. (1.13). This will be very useful for the discussion in Chapter 3, where we focus on the closed system physics of an atomic cloud coupled to several atomic resonators, generalizing the discussion presented here. Despite the plethora of interesting phenomena concerning the Dicke model, for our purposes, it will suffice to discuss the main properties of its phase diagram. In order to make direct connection with the discussion in Chapter 3, we will use two approaches: a simple mean-field expansion of the Dicke Hamiltonian, and an exact diagonalization approach, following the route presented by Emary and Brandes [39]. Clearly, the second option will provide a more detailed and accurate picture. However, it is still interesting to discuss the first approach as it turns out to offer a very good qualitative picture and can provide useful insights of the model by performing very simple calculations. Additionally, it is a very common approach to study the dynamics in the case when the system is open.

Before discussing these two procedures, let us slightly modify the physical picture by mapping the collective spin operators into bosonic operators $\hat{b}^\dagger$ and $\hat{b}$, obeying $[\hat{b}, \hat{b}^\dagger] = 1$, making use of the Holstein-Primakoff transformation

$$\hat{J}_+ = \hat{b}^\dagger \sqrt{N - \hat{b}^\dagger \hat{b}} \qquad \hat{J}_- = \sqrt{N - \hat{b}^\dagger \hat{b}}\, \hat{b} \qquad \hat{J}_z = \hat{b}^\dagger \hat{b} - \frac{N}{2}, \tag{1.15}$$

which results in the Hamiltonian

$$\hat{H} = -\Delta \hat{a}^\dagger \hat{a} + \omega_0 \left(\hat{b}^\dagger \hat{b} - \frac{N}{2} \right) + \frac{\lambda}{\sqrt{N}} \left(\hat{a}^\dagger + \hat{a} \right) \left(\hat{b}^\dagger \sqrt{N - \hat{b}^\dagger \hat{b}} + \sqrt{N - \hat{b}^\dagger \hat{b}}\, \hat{b} \right). \tag{1.16}$$

The key idea behind this step is to facilitate the study of this model when considering the thermodynamics limit $N \to \infty$.

Mean-field approximation

The starting point of this approach consists of introducing a mean-field energy E_{MF}, by defining the average values of the bosonic modes as $\alpha = \langle \hat{a} \rangle$ and $\beta = \langle \hat{b} \rangle$, which will play the role of order parameters, and minimize it with respect to α and β to obtain the corresponding ground state as a function of the system parameters. Using the Hamiltonian defined in (1.16), up an irrelevant constant shift, we obtain

$$E_{\mathrm{MF}} = -\Delta|\alpha|^2 + \omega_0|\beta|^2 + \frac{\lambda}{\sqrt{N}}\left(\alpha + \alpha^*\right)\left(\beta^* + \beta\right)\sqrt{N - |\beta|^2}. \tag{1.17}$$

Minimizing with respect to α leads to

$$\alpha = -\frac{\lambda}{(-\Delta)}\left(\beta^* + \beta\right)\sqrt{1 - \frac{|\beta|^2}{N}} \tag{1.18}$$

resulting in

$$E_{\mathrm{MF}} = \omega_0|\beta|^2 - \frac{\lambda^2}{(-\Delta)}\left(\beta^* + \beta\right)^2\left(1 - \frac{|\beta|^2}{N}\right). \tag{1.19}$$

Splitting the order parameter as $\beta = \mathrm{Re}[\beta] + i\mathrm{Im}[\beta]$ and further minimizing the energy with respect to $\mathrm{Im}[\beta]$, we obtain $\mathrm{Im}[\beta] = 0$, yielding

$$E_{\mathrm{MF}} = \omega_0\left(\frac{\mu - 1}{\mu}\beta^2 + \frac{1}{N}\frac{\beta^4}{\mu}\right) \tag{1.20}$$

where we introduced a new parameter $\mu = \lambda_{\mathrm{cr}}^2/\lambda^2$, with $\lambda_{\mathrm{cr}} = \frac{\sqrt{(-\Delta)\omega_0}}{2}$. As we will see λ_{cr} corresponds to the critical coupling strength at which the phase transition occurs. The phase diagram now follows from the resulting global minima of E_{MF} in (1.20). As a function of the coupling strength λ, we find two different phases:

- **Normal phase** (NP) - For $\lambda < \lambda_{\mathrm{cr}}$ there is only one global minimum, corresponding to $\beta = 0$ and $\alpha = 0$. This is associated with the cavity being empty, and the collective spin pointing towards the south pole of the Bloch sphere $(\langle \hat{J}_x \rangle, \langle \hat{J}_y \rangle, \langle \hat{J}_z \rangle) = (0, 0, -\frac{N}{2})$.

- **Superradiant phase** (SP) - For $\lambda > \lambda_{\mathrm{cr}}$, the $\mathbb{Z}_2$ symmetry is spontaneously broken and a pair of minima emerge with $\beta = \pm\sqrt{\frac{N}{2}(1-\mu)}$. Here, the cavity field gets *macroscopically* occupied, as $(\alpha, \beta) \propto \sqrt{N}$, and the collective spin acquires a finite component along the x direction, as $\langle \hat{J}_x \rangle \propto \beta$. Note that for the cavity, the difference between the two possible solutions corresponds to the phase of α, which can be either 0 or π.

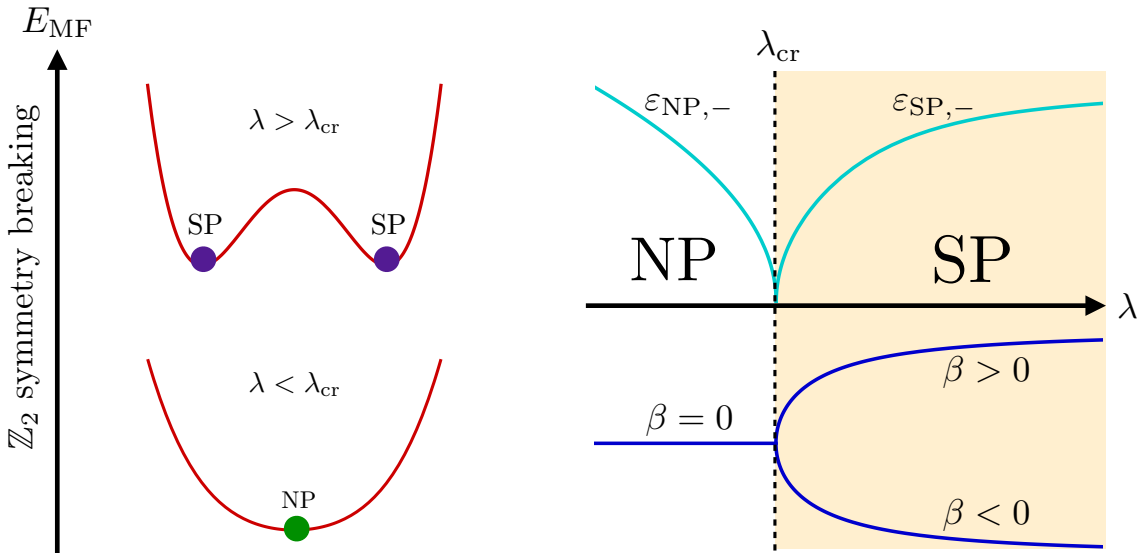

Figure 1.3: Schematic depiction of the properties of the superradiant phase transition for a closed system. On the left, we show the mean-field energy E_{MF} in the two parameter regimes, above and below the critical coupling λ_c. The $\mathbb{Z}_2$ symmetry breaking is observed in the splitting of the global minimum (solid green dot), representing the NP, into two degenerate minima for $\lambda > \lambda_c$ (solid purple dots), representing the superradiant ground states. On the right, we plot the lower branch of the excitation spectrum (solid cyan) and the bosonic order parameter (solid blue), as a function of the light-matter coupling λ. We observe how at the critical point the gap in the spectrum closes, signaling the phase transition, and the order parameter acquires a finite value, which can be positive or negative as a consequence of the symmetry breaking.

Note that at $\lambda = \lambda_{\mathrm{cr}}$ the order parameters approach zero in each phase, meaning that this is a phase transition of *second order*.

We have thus obtained the already predicted superradiant phase transition, the critical point λ_{cr} at which this transition occurs and the form of the order parameters. These results are summarized in Fig. 1.3. To further understand the properties of each phase and the character of the transition, it is necessary to go beyond this mean-field energy approach.

Exact diagonalization

In general, the next step to go beyond the mean-field approximation would be to expand the operators around their mean-field values and expand the interaction terms in the Hamiltonian up to quadratic order. Excitingly, for the Dicke Hamiltonian (1.16) this turns to be particularly easy. In the thermodynamic limit the interaction is quadratic and the Hamiltonian becomes exactly diagonalizable. In the previous section, we learned that the phase diagram displays two different phases, distinguished by the values of the

order parameters (α, β), which vanish in the NP and are proportional to $\sqrt{N}$ in the SP. We can now use this knowledge to simplify the non-linear interaction in the Hamiltonian (1.16).

Let us first consider the NP. In the thermodynamic limit $N \to \infty$, the occupation of the modes is much smaller than N. Therefore we can neglect the terms proportional to $\hat{b}^\dagger \hat{b}$ inside the square roots in (1.16), leading to

$$\hat{H} = -\Delta \hat{a}^\dagger \hat{a} + \omega_0 \hat{b}^\dagger \hat{b} + \lambda \left(\hat{a}^\dagger + \hat{a}\right)\left(\hat{b}^\dagger + \hat{b}\right). \tag{1.21}$$

After this simplification, the Hamiltonian is effectively quadratic and it is thus diagonalizable. The precise steps are very simple and they are explained in detail in [39]. They amount to moving into a position-momentum $(\hat{x}_{1,2}, \hat{p}_{1,2})$ representation for each mode, where the interaction term corresponds to an $\hat{x}_1 \hat{x}_2$ type coupling. Next, one needs to perform a rotation to decouple the position coordinates, and then return to the creation and annihilation operator picture. Up to a constant shift, the resulting diagonalized Hamiltonian is

$$\hat{H}_{\mathrm{NP}} = \varepsilon_{\mathrm{NP},+}\, \hat{c}^\dagger_{\mathrm{NP},+} \hat{c}_{\mathrm{NP},+} + \varepsilon_{\mathrm{NP},-}\, \hat{c}^\dagger_{\mathrm{NP},-} \hat{c}_{\mathrm{NP},-}, \tag{1.22}$$

where the spectrum is defined as

$$\varepsilon^2_{\mathrm{NP},\pm} = \frac{1}{2}\left[\Delta^2 + \omega_0^2 \pm \sqrt{\left(\Delta^2 - \omega_0^2\right)^2 - 16\lambda^2 \Delta \omega_0}\right]. \tag{1.23}$$

Crucially, in this expression we can observe how the "$-$" mode starts softening as the value of λ is increased. In particular, when $\lambda = \lambda_{\mathrm{cr}}$ this energy branch reaches zero, corresponding to a gap closing in the spectrum and resulting in a phase transition. For $\lambda > \lambda_{\mathrm{cr}}$ the spectrum (1.23) becomes imaginary, meaning that this effective description is not valid anymore in the superradiant phase.

So how do we proceed now? The key point is that in the superradiant phase the order parameters are proportional to $\sqrt{N}$, and thus $\langle \hat{b}^\dagger \hat{b} \rangle \sim N$, meaning that the terms inside the square root cannot be neglected anymore. The trick to go about this is to displace the bosonic operators by their respective average values as $\hat{a} \to \alpha + \hat{c}$ and $\hat{b} \to \beta + \hat{d}$. Considering again the thermodynamic limit, we can then expand the square root terms to obtain a quadratic Hamiltonian by eliminating all terms with negative powers of N. As shown in [39], these steps lead to the presence of linear terms in our Hamiltonian that we want to get rid of. For them to vanish, the order parameters need to satisfy the conditions

$$2\lambda\beta\sqrt{1 - \frac{\beta^2}{N}} - \Delta\alpha = 0 \qquad\qquad \left[\frac{4\lambda^2}{\Delta N}(N - 2\beta^2) + \omega_0\right]\beta = 0. \tag{1.24}$$

In fact, the two possible sets of solutions to these conditions correspond to the order parameters in the NP and SP as defined above. In the NP, the trivial solution results in no displacement of the operators and leads to the description in Eq. (1.22). In this case, we are instead interested in the second set of solutions with α given by Eq. (1.18) and $\beta = \sqrt{\frac{N}{2}(1-\mu)}$. We are then left with the quadratic Hamiltonian

$$\hat{H} = -\Delta \hat{c}^\dagger \hat{c} + \frac{\omega_0}{2\mu}(1+\mu)\hat{d}^\dagger \hat{d} + \frac{\omega_0(1-\mu)(3+\mu)}{8\mu(1+\mu)}\left(\hat{d}^\dagger + \hat{d}\right)^2 + \lambda\mu\sqrt{\frac{2}{1+\mu}}\left(\hat{c}^\dagger + \hat{c}\right)\left(\hat{d}^\dagger + \hat{d}\right). \tag{1.25}$$

We observe that in the limit $\mu \to 1$, i.e. $\lambda = \lambda_{\mathrm{cr}}$, the Hamiltonians (1.21) and (1.25) coincide, thus confirming our intuition that the phase transition is indeed of second order. This Hamiltonian can now be diagonalized following the same steps as before, yielding

$$\hat{H}_{\mathrm{SP}} = \varepsilon_{\mathrm{SP},+}\,\hat{c}^\dagger_{\mathrm{SP},+}\hat{c}_{\mathrm{SP},+} + \varepsilon_{\mathrm{SP},-}\,\hat{c}^\dagger_{\mathrm{SP},-}\hat{c}_{\mathrm{SP},-}, \tag{1.26}$$

with spectrum

$$\varepsilon^2_{\mathrm{SP},\pm} = \frac{1}{2}\left[\frac{\omega_0^2}{\mu^2} + \Delta^2 \pm \sqrt{\left(\frac{\omega_0^2}{\mu^2} - \Delta^2\right)^2 + 4\Delta^2\omega_0^2}\right], \tag{1.27}$$

where we again see how as $\lambda \to \lambda_{\mathrm{cr}}$ the lower branch starts softening until the gap is closed at the critical point. This is shown in Fig. 1.3.

In summary, we have analyzed the system using two approaches. First, the mean-field approximation, based on a Landau free energy scheme, provided some qualitative insights about the form of the phase diagram, where we obtained the critical point and the order parameters. Next, using this knowledge, we exploited the simple form of the Hamiltonian in the thermodynamic limit and diagonalized it to obtain the excitation spectrum on top of each phase. In chapter 3, we will revisit these approaches and generalize these results to the case for multiple bosonic modes interacting with each other.

1.3.2 Open system

We are now interested in explicitly considering the open nature of our system. In particular, we will focus on the presence of photon losses in the system, meaning the number of photonic excitations in our system will decay at rate κ. This was first considered in [40], where an experimental realization of Dicke model in ring cavities was proposed, and later studied in more detail in [41–44], in the context of a cavity mode coupled to a BEC. Other types of dissipation channels, such as spin dephasing or spontaneous emission,

have also been considered recently in the context of the Dicke model and shown to also influence the dynamics in non-trivial ways [45]. As opposed to the closed case, now the definition of our problem is intrinsically different. In the closed system we were looking for the ground state, i.e. the configuration in which the system minimizes the energy. Instead, here we are interested in the dynamics of the system. In particular, we focus on the possible steady states it exhibits and their stability against fluctuations, which define a steady-state phase diagram.

As previously mentioned, the formalism for treating open systems will only be introduced in Chapter 2, but for now it will suffice to add dissipation phenomenologically. Additionally, we will not make use of the Holstein-Primakoff transformation and we will look instead at the dynamics of the collective spin. We will consider the large N limit, thus allowing to describe the system through the dynamics of their mean-field values. From the Hamiltonian (1.13), we can obtain the dynamics in the Heisenberg picture. This leads to

$$\begin{aligned}
\partial_t \alpha &= \left(i\Delta - \frac{\kappa}{2}\right)\alpha - i\frac{2\lambda}{\sqrt{N}}S_x \\
\partial_t S_x &= -\omega_0 S_y \\
\partial_t S_y &= \omega_0 S_x - \frac{2\lambda}{\sqrt{N}}\left(\alpha + \alpha^*\right)S_z \\
\partial_t S_z &= \frac{2\lambda}{\sqrt{N}}\left(\alpha + \alpha^*\right)S_y,
\end{aligned} \tag{1.28}$$

where we have introduced the mean-field values $(S_x, S_y, S_z) = (\langle \hat{J}_x \rangle, \langle \hat{J}_y \rangle, \langle \hat{J}_z \rangle)$ and $\alpha = \langle \hat{a} \rangle$ is defined as before. Again, note that we have added the presence of photon losses by hand, on the first equation, by including a decay rate κ. It is also important to note that these equations are still invariant under parity transformations $(\alpha, S_x) \to -(\alpha, S_x)$. Thus, we expect that the presence of a phase transition will also lead two the emergence of a pair of steady states. The steady-states of the dynamics can now be obtained by setting the equations of motion to zero. We thus arrive at the steady-state conditions

$$\alpha = \frac{2\lambda S_x}{\sqrt{N}(\Delta + i\frac{\kappa}{2})} \qquad S_y = 0 \qquad \left[\omega_0 - \frac{8\lambda^2\Delta}{N(\Delta^2 + \frac{\kappa^2}{4})}S_z\right]S_x = 0, \tag{1.29}$$

resulting in two fixed points of the dynamics, one associated with the NP and another with the SP. The former corresponds to the solution $\alpha = S_x = 0$ and $S_z = -\frac{N}{2}$, in analogy

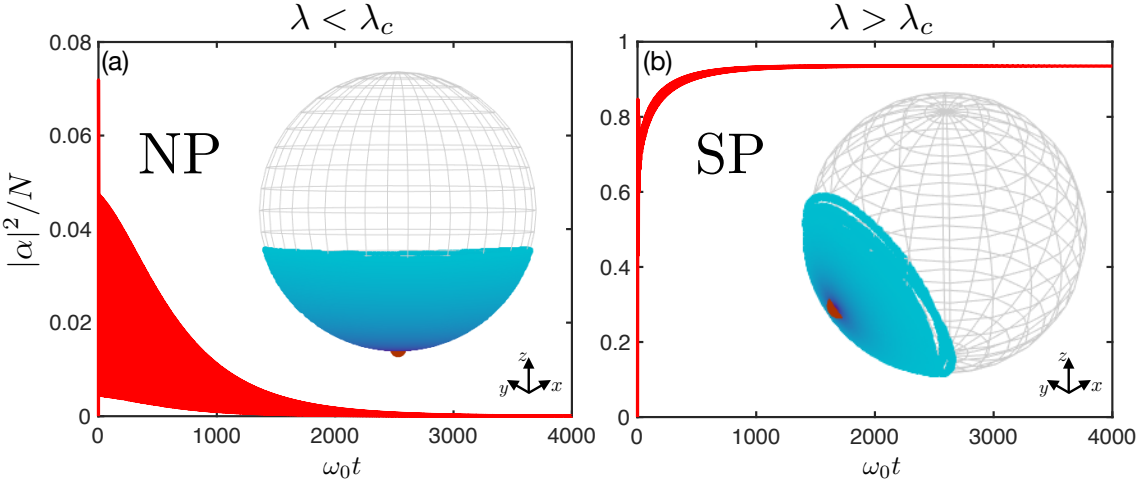

Figure 1.4: Dynamics of the system, as given by Eqs. (1.28), below and above the critical point λ_c. The cavity field is given in the solid red curves and the collective spin is plotted on a Bloch sphere, with a darker trajectory color for later times and the steady state denoted by a solid red dot. In (a), we show the evolution inside the NP, where we see how the collective spin stabilizes in the south pole of the Bloch sphere $S_z = -\frac{N}{2}$and the cavity field approaches zero in the long-time limit. In (b), we observe how the SP becomes the steady state above threshold, with the collective spin acquiring a finite component in the x direction and the cavity field getting macroscopically populated. Paremeters: (a) $\Delta = -10\omega_0$, $\kappa = 4\omega_0$, $\lambda = 0.5\omega_0$; (b) $\Delta = -\omega_0$, $\kappa = 0.5\omega_0$, $\lambda = \omega_0$. For both cases a generic initial condition was taken.

with the result obtained for the closed case. The latter yields

$$S_x = \pm\frac{N}{2}\sqrt{1 - \frac{\omega_0^2\left(\Delta^2 + \frac{\kappa^2}{4}\right)^2}{16\lambda^4\Delta^2}}, \tag{1.30}$$

corresponding to the two different superradiant steady states, where S_z results from Eq. (1.29), and S_x is obtained from the spin length conservation condition $S_x^2 + S_y^2 + S_z^2 = \frac{N^2}{4}$. The critical point can be extracted directly from (1.30) as the value of λ for which S_x becomes complex, corresponding to

$$\lambda_c = \frac{1}{2}\sqrt{\frac{\omega_0\left(\Delta^2 + \frac{\kappa^2}{4}\right)}{(-\Delta)}}. \tag{1.31}$$

In Fig. 1.4 we present the time evolution of a generic trajectory in the NP and the SP. The steady-state characteristics are similar to those of the ground-state picture, with the difference that the critical point and the exact form of the order parameters are now also dependent on the photon loss rate κ in a non-trivial way.

We corroborate these results by performing a linear stability analysis of the semiclassi-

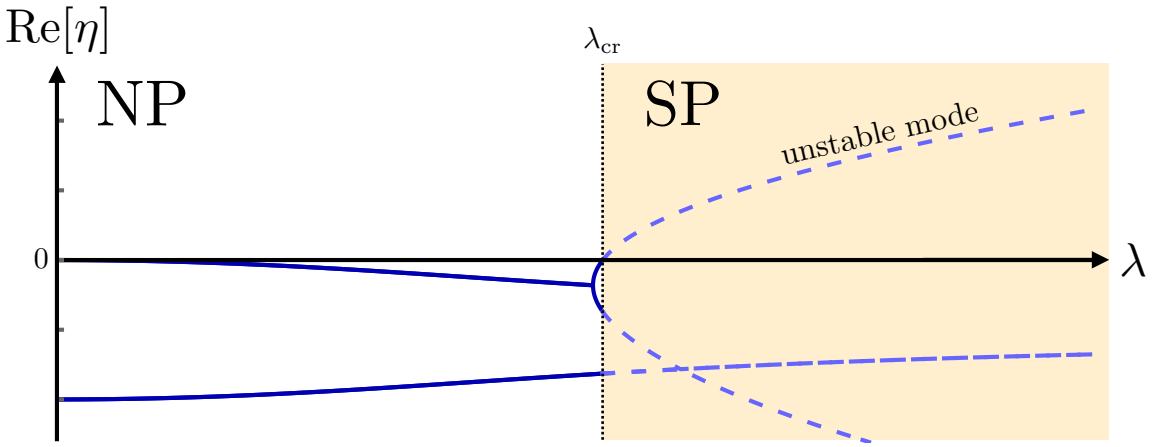

Figure 1.5: Stability of the dynamical modes of the system inside the NP. Below threshold (solid blue curves), all eigenvalues of the dynamical matrix (1.32) possess negative real part, yielding damping towards the NP attractor. Above threshold, one of the eigenvalues acquires a positive real part, corresponding to the NP fixed point becoming unstable in favor of the SP becoming the new steady state.

cal equations of motion (1.28). This amounts to performing the expansions $\hat{a}(t) = \alpha + \delta\hat{a}(t)$ and $\hat{J}_\sigma(t) = S_\sigma + \delta\hat{J}_\sigma(t)$, where α and S_σ are steady-state values, and linearizing the equations of motion. Following these steps leads to the linearized equations of motion

$$\partial_t \begin{pmatrix} \delta\hat{a} \\ \delta\hat{a}^\dagger \\ \delta\hat{J}_x \\ \delta\hat{J}_y \end{pmatrix} = \begin{pmatrix} \left(i\Delta - \frac{\kappa}{2}\right) & 0 & -i\frac{2\lambda}{\sqrt{N}} & 0 \\ 0 & -\left(i\Delta + \frac{\kappa}{2}\right) & i\frac{2\lambda}{\sqrt{N}} & 0 \\ 0 & 0 & 0 & -\omega_0 \\ -\frac{\lambda S_z}{\sqrt{N}} & -\frac{\lambda S_z}{\sqrt{N}} & \omega_0 + \frac{\lambda}{\sqrt{N}}\frac{S_x}{S_z}(\alpha + \alpha^*) & 0 \end{pmatrix} \begin{pmatrix} \delta\hat{a} \\ \delta\hat{a}^\dagger \\ \delta\hat{J}_x \\ \delta\hat{J}_y \end{pmatrix}, \tag{1.32}$$

where the fluctuations along the z direction are fixed by $S_x\delta\hat{J}_x + S_z\delta\hat{J}_z = 0$, taking into account that $S_y = 0$ in both phases. Note that the matrix elements of the dynamical matrix depend on the order parameters (α, S_x). To search for the presence of the phase transition, it is most convenient to carry out this analysis in the NP, where $\alpha = S_x = 0$ and $S_z = -\frac{N}{2}$, and obtain when the fluctuations become unstable. Plugging these values into the dynamical matrix in Eq. (1.31), we arrive at the eigenvalue equation

$$\left(\omega_0^2 + \eta^2\right)\left[\Delta^2 + \left(\eta + \frac{\kappa}{2}\right)^2\right] + 4\Delta\lambda^2 = 0, \tag{1.33}$$

with η the eigenvalues of the dynamical matrix. The imaginary part of η is associated with the frequencies of the eigenmodes and the real part with their damping. In particular, the latter determines the stability of the fixed points. A stable fixed point results in $\mathrm{Re}[\eta] < 0$ for all eigenvalues, while an unstable one possesses at least one eigenvalue with $\mathrm{Re}[\eta] > 0$.

For $\lambda = 0$, we retrieve the eigenfrequecies of the uncoupled system $\eta = i\omega_0, -i\omega_0, i\Delta - \frac{\kappa}{2}$ and $-i\Delta - \frac{\kappa}{2}$. For finite λ, this equation does not admit a compact analytical form, and needs to be solved numerically. In Fig. 1.5, we present the real part of the eigenvalues as a function of λ for the NP fixed point. As expected, at the critical point, one of the modes approaches zero, and becomes positive above threshold, signalling the transition of the NP to an unstable fixed point.

To summarize, in this section we have considered the open version of the Dicke model and studied its semiclassical equations of motion. We found that the phase transition survives the presence of dissipation, and overall exhibits qualitatively similar features to that of the ground-state transition. Namely, the steady-state is unique in the NP and splits into two different ones, connected by a parity transformation, when crossing into the SP. The main difference resulted in the exact form of the order parameters and the position of the critical point, which shows a non-trivial dependence on the dissipation rate. It is worth mentioning that a second, less obvious difference also exists. The critical exponent of the phase transition in the closed case, equal to -1 [39], differs to that of the open case, which has been shown to be equal to $-\frac{1}{2}$ [43]. This points out that despite the similarities between both cases, the intrinsically different nature of each transition makes them distinguishable, even in the $\kappa \to 0$ limit, where the equations of motion and order parameters become equal.

1.4 Self-organization phase transition

Let us now return to our original problem. In Sec. 1.2.2, we arrived at the Dicke model as an effective description for the interaction between a single mode of an optical cavity and the external degrees of freedom of a BEC. In Sec. 1.3, we explored the Dicke model and showed that this model exhibits a phase transition. So what does this physically mean for the atomic gas interacting with the cavity? Tracing back our derivation of Eq. (1.13), the effective two-level systems depicted the atoms either being part of the BEC or occupying an excited momentum state with $\vec{k} = \vec{k}_p$ and accounting for the entire atomic cloud led to the collective spin $\hat{\vec{J}}$. For small λ, i.e. for weak pump strength, atom-photon scattering events occur at a very low rate, followed by their loss through the cavity mirror. Therefore, on average, the atoms remain in the BEC, while the cavity stays in its vacuum state. This corresponds to the NP, where the full occupation of the BEC is equivalent to all two-level systems pointing down, meaning $S_z = -\frac{N}{2}$. More photons get scattered into the cavity as we increase the strength of the drive, thus increasing λ, and this behavior remains stable until the threshold value is reached $\lambda = \lambda_{\mathrm{cr}}$. Beyond this

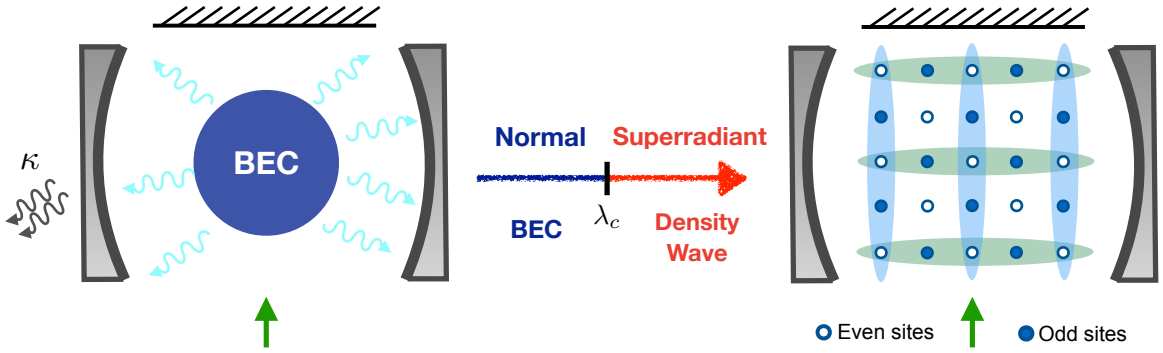

Figure 1.6: Schematic picture of the self-organization phase transition. For $\lambda < \lambda_{\mathrm{cr}}$ all the atoms are in the BEC, and scattered photons leak out before any light field is able to build up inside the cavity. For $\lambda > \lambda_{\mathrm{cr}}$, a finite cavity field is formed inside the cavity, leading to the self-organization of the atoms in a checkerboard-pattern, either in the even or odd sites, thus forming a so-called density wave.

value, the phase transition takes place and we can interpret the behavior of the system in two different ways.

One way is to think of the amount of photons scattered into the cavity overcoming the amount that is dissipated, resulting in the build up of a finite amplitude of the light field. The combination between the finite cavity field and the transverse drive generates an effective lattice potential for the atoms of the form $\cos(kx)\cos(kz)$, as previously shown in Eq. (1.9). In the presence of this new potential, the atoms adapt by starting a process of self-organization in which they occupy either the even $(\cos(kx)\cos(kz) = 1)$ or the odd sites $(\cos(kx)\cos(kz) = -1)$. This results in the formation of a periodic checkerboard-like spatial structure commonly referred to as *density wave* (DW) or *density-wave state*, which in this picture is the counterpart of the SP phase. The occupation of either even or odd sites stems from the breaking of the $\mathbb{Z}_2$ symmetry present in our model. The specific choice also fixes the phase of the cavity field to either 0 or π. On the other hand, this transition can also be interpreted as the atoms starting to occupy the excited momentum state as a result of the high incoming flux of pump photons. The spatial wave function of the excited state $|k\rangle$ is proportional to $\cos(kx)\cos(kz)$, corresponding to the atoms populating the density-wave state. This spatial structure then acts as a Bragg lattice for the incoming transverse drive which can then efficiently transfer photons into the cavity, generating a finite population of the cavity mode. The phase transition is schematically shown in Fig. 1.6.

Overall, we can view this process as a self-sustained mechanism in which the density-wave state allows for the generation of cavity photons and these in turn strengthen the potential that keeps the atoms organized in a checkerboard pattern. Physically, the

presence of this phase transition can be understood as a competition between the kinetic energy which favors a homogeneous spatial distribution, i.e the BEC, and the long-ranged interactions with the cavity field which in turn favors the formation of a spatial structure. It is important to remind ourselves that the picture provided by the Dicke model is only valid within the single-recoil limit. This turns out to be a good description close to criticality, but as one increased the pump strength further, higher momentum states start getting occupied. Therefore, within our effective description, even in the self-organized regime, it still holds that the majority of the atoms still occupy the BEC state $\langle \hat{b}_0^\dagger \hat{b}_0 \rangle \sim O(N)$, while the population of the excited state, despite not being zero, is of order 1.

Self-organization due to atom-cavity interactions was first described [46] and experimentally observed [47] in the context of thermal atoms in 2003. Almost a decade later this phenomenon was experimentally realized for quantum gases [23], where a connection with a quantum phase transition and Dicke model was first made. This triggered a plethora of theoretical studies [41–44, 48, 49] and experimental follow-ups [50–53], which further characterized the properties of the phase transition and explored the out-equilibrium dynamics of the system. As mentioned previously, the work of Baumann et al. [23] has also become the cornerstone for countless experimental extensions of this set-up, including the use of multimode cavities [24, 25], optical lattices [26, 27], multiple cavities [28–30] and spinor BEC's [31–33].

Before finalizing the introduction chapter, we consider one further extension of the BEC in a cavity model, which includes the presence of an external optical lattice in the system. This constitutes the basis of the phenomena studied in Chapter 5.

1.5 Optical lattices

In this section we derive the effective model describing an ultra-cold atomic gas coupled to the single mode of an optical cavity and in the presence of an external optical lattice in the x-z plane. We assume a third, much deeper, lattice potential in the y direction that effectively splits the system in several two-dimensional copies. In relation with our previous discussion, the laser in the z direction acts both as an external pump and as a lattice potential for the atomic cloud. For the sake of generality, we consider the cavity to be rotated by an angle φ in the x-z plane and define its wave vector as $\vec{k}_c = \frac{2\pi}{\lambda_c}(\cos\varphi, 0, \sin\varphi)$. We also allow the cavity wavelength λ_c to be different from the lattice (pump) wavelength λ_p.

Our starting point is the single-particle Hamiltonian defined in Sec. 1.2.2

$$\hat{H} = -\Delta\hat{a}^\dagger\hat{a} + \int d\vec{x}\left\{\hat{\Psi}^\dagger(\vec{x})\left[\frac{\vec{p}^2}{2m} + \hat{V}_{\text{trap}} + U_0\cos^2\left(\vec{k}_{\text{c}}\vec{x}\right)\hat{a}^\dagger\hat{a} + V_0\left(\cos^2\left(k_{\text{p}}x\right) + \cos^2\left(k_{\text{p}}z\right)\right)\right.\right.$$
$$\left.\left. + \eta\cos\left(\vec{k}_{\text{c}}\vec{x}\right)\cos\left(k_{\text{p}}z\right)(\hat{a} + \hat{a}^\dagger)\right]\hat{\Psi}(\vec{x}) + \frac{\alpha_s}{2}\hat{\Psi}^\dagger(\vec{x})\hat{\Psi}^\dagger(\vec{x})\hat{\Psi}(\vec{x})\hat{\Psi}(\vec{x})\right\}, \tag{1.34}$$

where we have now also included the external lattice potential in the x direction. We then expand the field operators in term of Wannier functions $\hat{\Psi} = \sum_i W_i(\vec{x})\hat{b}_i$. The Wannier functions $W_i(\vec{x})$ are defined as the eigenfunctions of the non-interacting Hamiltonian $\hat{H}_0 = \frac{\vec{p}^2}{2m} + V_0\left(\cos^2\left(k_{\text{p}}x\right) + \cos^2\left(k_{\text{p}}z\right)\right)$. They exhibit the same periodicity as the lattice and are strongly localized at sites $i = (i_x, i_z)\frac{\lambda_p}{2}$. In particular, we restrict ourselves to the lowest Bloch band of the Hamiltonian. The operators $\hat{b}_i$ and $\hat{b}_i^\dagger$ the annihilation and creation operators for particles at a specific site i. Inserting this decomposition into (1.34) we obtain

$$\hat{H} = \sum_i \varepsilon_i\hat{n}_i - J\sum_{\langle i,j\rangle}\hat{b}_i^\dagger\hat{b}_j + \frac{U}{2}\sum_i \hat{n}_i(\hat{n}_i - 1) - \Delta\hat{a}^\dagger\hat{a} + \sum_i \delta_i\hat{n}_i\hat{a}^\dagger\hat{a} + \left(\hat{a}^\dagger + \hat{a}\right)\sum_i g_i\hat{n}_i, \tag{1.35}$$

where $\hat{n}_i = \hat{b}_i^\dagger\hat{b}_i$ is the number operator at site i. The first term can be interpreted as a local chemical potential $\varepsilon_i \approx V_{\text{trap}}(x_i, z_i)$ due to presence of the trap, which we have assumed to be slowly varying. For the second and third terms, the parameters

$$J = \int\int dxdz\; W_i^*(x,z)\;\left[\frac{\vec{p}^2}{2m} + V_0\left(\cos^2\left(k_{\text{p}}x\right) + \cos^2\left(k_{\text{p}}z\right)\right)\right]\; W_i\left(x, z - \frac{\lambda}{2}\right) \tag{1.36}$$

$$U = \frac{\alpha}{2}\int\int dxdz\;|W_i(x,z)|^4 \tag{1.37}$$

correspond to the hopping amplitude, which we have considered only up to nearest neighbor, and the on-site interaction strength. The fifth term in (1.35), with

$$\delta_i = U_0\int dxdz\; W_i^*(x,z)\cos^2\left(\vec{k}_c\cdot\vec{x}\right)W_i\left(x,z\right), \tag{1.38}$$

is associated with the dispersive shift, where it now depends on the specific configuration of the atoms on the lattice. Note that considering general $\lambda_c \neq \lambda_p$ and/or $\varphi \neq 0$ yields a site dependent shift. The last term corresponds to the atom-light scattering process, where

$$g_i = \eta\int dxdz\; W_i^*(x,z)\cos\left(\vec{k}_c\cdot\vec{x}\right)\cos\left(kz\right)W_i\left(x,z\right). \tag{1.39}$$

After having derived a general model, we now focus on the more specific case of $\lambda_c = \lambda_p$ and $\varphi = 0$. Ultimately, in Chapter 5 we will be interested in exploring the experimental set-up realized in [23], which satisfies this condition. Other studies have considered an incommensurate ratio λ_c/λ_p and showed that glassy phases and structural superfluids may arise in this case [54]. Two important simplifications take place when considering equal pump and cavity wavelengths. First, the dispersive shift becomes equivalent for all sites, leading to an energy shift $\sum_i \delta_i \hat{n}_i = N\delta$, which we absorb in the definition of Δ. Second, the light matter coupling adopts the form $g_i = P_i g$, where $P_i = \pm 1$ is the parity of site i. This results in the light field being coupled to the operator $\hat{\Phi} = \sum_e \hat{n}_e - \sum_o \hat{n}_o$, which measures the occupation imbalance between even and odd sites. Additionally, we will for simplicity neglect the effects of the trapping potential. Including these simplifications into Eq. (1.35) yields the effective Hamiltonian

$$\hat{H} = -J \sum_{\langle i,j \rangle} \hat{b}_i^\dagger \hat{b}_j + \frac{U}{2} \sum_i \hat{n}_i(\hat{n}_i - 1) - \Delta \hat{a}^\dagger \hat{a} + g\left(\hat{a}^\dagger + \hat{a}\right)\hat{\Phi}, \tag{1.40}$$

which corresponds to a modified version of the well-known Bose-Hubbard model. The properties of this Hamiltonian have been considered both experimentally [26, 27, 55] and theoretically [54, 56–58], showing that it exhibits a rich phase diagram resulting from the competition of scales between the kinetic energy, given by the hopping term, the short-ranged interactions and the infinite-range interactions mediated by the cavity photons. In Chapter 5, we will focus on the impact of photon losses in the dynamics of this model and discuss its relaxation dynamics towards the steady state.

2

Open quantum systems

2.1 Introduction

An open quantum system is defined as a quantum system coupled to an external bath, leading to the presence of dissipative processes in its dynamics [59, 60]. In general, all physical systems are intrinsically open, with the only exception of the universe as a whole. Thus, a description of any realistic system requires accounting for the presence of dissipative channels. This is particularly important in certain areas such as quantum information [61], where it is crucial to understand the impact of losses in order to design robust protocols and efficient experimental platforms. Additionally, dissipation can also serve as a mean to drive a system into particular states of interest, opening the door to the field of reservoir engineering [62]. Our current understanding of open quantum systems is rudimentary compared to that of closed systems. This makes open systems an active field of research not only from a practical point of view, but also from a fundamental perspective. A representative example is the study of quantum many-body systems in open settings [63, 64]. There, great progress is being made along several lines such as classifying many-body phases of matter [65, 66], identifying clear signatures for phase transitions [67] or exploring novel features which emerge when the system is open [68].

There is a wide variety of strategies to approach open quantum systems, with the appropriate choice depending on the problem at hand. Throughout this thesis, we make use of the formalism of Linblad master equations to describe the open dynamics of atom-cavity systems. In this chapter, we introduce this formalism and provide a minimal background in order to follow the discussions in Chapters 4 and 5. In Sec. 2.2, we present a derivation for the Lindblad master equation, and in Sec. 2.3 we outline the main properties of this framework, in contrast with the usual properties of closed systems.

2.2 Master equation

While there are several methods to derive the form of the master equation, our derivation will make use of the so-called projection methods or Nakajima-Zwanzig formalism [69, 70]. Specifically, we follow the steps presented in [59]. In short, the strategy consists of splitting the whole system into a small subsystem and a bath and then tracing out the bath degrees of freedom to obtain an effective equation of motion for the subsystem. Tracing out the bath degrees of freedom turns out to be a rather complex procedure which in general cannot be carried out. However, in many relevant physical systems it is possible to introduce a set of approximations that make this elimination procedure possible. These assumptions are known as the *Born approximation* or weak-coupling condition and the *Markov approximation*. Both will be key in order to derive the final form of the master equation[1].

We consider the time evolution for the density matrix of a closed system of the form

$$\partial_t \hat{\rho} = \mathcal{L}\hat{\rho} = -i[\hat{H}, \hat{\rho}] = -i\left[\hat{H}_{\text{sys}} + \hat{H}_{\text{B}} + \hat{H}_{\text{int}}, \hat{\rho}\right], \tag{2.1}$$

where we have split the evolution into three terms: $\hat{H}_{\text{sys}}$ contains the evolution with support only in the subsystem we are interested in studying, which we denote as 'system' from now on; $\hat{H}_{\text{B}}$ corresponds to the rest of degrees of freedom of the whole system, which correspond to the external bath, labeled 'B'; and finally, $\hat{H}_{\text{int}}$ includes the interaction terms between the system and the bath. We have also introduced the superoperator $\mathcal{L}(\star) = (-i)[\hat{H}, \star]$, which determines the dynamical evolution of the density matrix $\hat{\rho}$.

To eliminate the bath degrees of freedom we define the projection operators

$$\mathcal{P}\hat{\rho} = \text{Tr}_{\text{B}}[\hat{\rho}(t)] \otimes \hat{\rho}_{\text{B}} \qquad\qquad \mathcal{Q} = 1 - \mathcal{P}, \tag{2.2}$$

where $\mathcal{P}$ projects the full density matrix into a product state, with $\hat{\rho}_{\text{B}}$ the steady state of the bath in the absence of coupling with the system and Tr_{B} the trace over the bath. Our objective is then to obtain an effective equation of motion for the projection $\mathcal{P}\hat{\rho}$, which only concerns the system degrees of freedom. These operators obey the properties:

$$\begin{aligned} &\text{i)} \quad \mathcal{P}\mathcal{L}_{\text{sys}} = \mathcal{L}_{\text{sys}}\mathcal{P} && \text{ii)} \quad \mathcal{P}\mathcal{L}_{\text{B}} = \mathcal{L}_{\text{B}}\mathcal{P} = 0 \\ &\text{iii)} \quad \mathcal{P}\mathcal{L}_{\text{int}}\mathcal{P} = 0 && \text{iv)} \quad \mathcal{P}^2 = \mathcal{P} \quad \mathcal{Q}^2 = \mathcal{Q}, \end{aligned} \tag{2.3}$$

[1] It is worth pointing out that strong efforts are currently being made to expand this formalism beyond the boundaries of these approximations, leading to so-called Non-Markovian Lindblad master equations [71].

where the subscripts on $\mathcal{L}$ denote which Hamiltonian is inside the commutator. Property (i) follows from $\mathcal{L}_{\text{sys}}$ and $\mathcal{P}$ operating on different sectors and (ii) from $\mathcal{P}$ taking the bath into the steady state. Property (iii) corresponds to assuming no interactions acting only on a single support, either the bath or the system, as these can be absorbed in the definitions of $\hat{H}_{\text{sys}}$ or $\hat{H}_{\text{B}}$, respectively. Lastly, property (iv) is true by definition of a projector operator. Using these properties, we can obtain the equations of motion for each sector

$$\begin{aligned}\partial_t(\mathcal{P}\hat{\rho})(t) &= \mathcal{L}_{\text{sys}}(\mathcal{P}\hat{\rho})(t) + \mathcal{P}\mathcal{L}_{\text{int}}(\mathcal{Q}\hat{\rho})(t)\\ \partial_t(\mathcal{Q}\hat{\rho})(t) &= \left(\mathcal{L}_{\text{B}} + \mathcal{L}_{\text{sys}} + \mathcal{Q}\mathcal{L}_{\text{int}}\right)(\mathcal{Q}\hat{\rho})(t) + \mathcal{Q}\mathcal{L}_{\text{int}}(\mathcal{P}\hat{\rho})(t).\end{aligned} \tag{2.4}$$

To introduce the first approximation we first simplify the form of the Eqs. (2.4) by using the Laplace transform[2] $f(s) = \int_0^\infty e^{-st} f(t)dt$, yielding

$$\begin{aligned}s(\mathcal{P}\hat{\rho})(s) - (\mathcal{P}\hat{\rho})(0) &= \mathcal{L}_{\text{sys}}(\mathcal{P}\hat{\rho})(s) + \mathcal{P}\mathcal{L}_{\text{sys}}(\mathcal{Q}\hat{\rho})(s)\\ s(\mathcal{Q}\hat{\rho})(s) - (\mathcal{Q}\hat{\rho})(0) &= \left(\mathcal{L}_{\text{B}} + \mathcal{L}_{\text{sys}} + \mathcal{Q}\mathcal{L}_{\text{int}}\right)(\mathcal{Q}\hat{\rho})(s) + \mathcal{Q}\mathcal{L}_{\text{int}}(\mathcal{P}\hat{\rho})(s).\end{aligned} \tag{2.5}$$

Solving for $(\mathcal{Q}\hat{\rho})(s)$ using the second equation and inserting this expression in the first one we obtain

$$\begin{aligned}s(\mathcal{P}\hat{\rho})(s) - \left\{(\mathcal{P}\hat{\rho})(0) + \mathcal{P}\mathcal{L}_{\text{int}}\left[s - \mathcal{L}_{\text{sys}} - \mathcal{L}_{\text{B}} - \mathcal{Q}\mathcal{L}_{\text{int}}\right]^{-1}(\mathcal{Q}\hat{\rho})(0)\right\}\\ = \left\{\mathcal{L}_{\text{sys}} + \mathcal{P}\mathcal{L}_{\text{int}}\left[s - \mathcal{L}_{\text{sys}} - \mathcal{L}_{\text{B}} - \mathcal{Q}\mathcal{L}_{\text{int}}\right]^{-1}\mathcal{Q}\mathcal{L}_{\text{int}}\right\}(\mathcal{P}\hat{\rho})(s).\end{aligned} \tag{2.6}$$

We now perform the first approximation and consider the coupling between the bath and the system to be weak with respect to the rest of energy scales in each sector. In the spirit of the Born approximation, this amounts to truncating the expression in (2.6) by keeping up to lowest order terms in $\mathcal{L}_{\text{int}}$, yielding

$$\begin{aligned}s(\mathcal{P}\hat{\rho})(s) - \left\{(\mathcal{P}\hat{\rho})(0) + \mathcal{P}\mathcal{L}_{\text{int}}\left[s - \mathcal{L}_{\text{sys}} - \mathcal{L}_{\text{B}}\right]^{-1}(\mathcal{Q}\hat{\rho})(0)\right\}\\ = \left\{\mathcal{L}_{\text{sys}} + \mathcal{P}\mathcal{L}_{\text{int}}\left[s - \mathcal{L}_{\text{sys}} - \mathcal{L}_{\text{B}}\right]^{-1}\mathcal{Q}\mathcal{L}_{\text{int}}\right\}(\mathcal{P}\hat{\rho})(s).\end{aligned} \tag{2.7}$$

The term proportional to $(\mathcal{Q}\hat{\rho})(0)$ can be neglected as it simply shifts the initial conditions and does not affect the dynamics at later times. On the other hand, the term proportional to $\mathcal{Q}\mathcal{L}_{\text{int}}$ on the second line does modify the effective evolution of the system dynamics. This term corresponds to the influence of the system-bath interactions on the

[2]For notational simplicity, we distinguish the functions in the time domain and the s domain only by their arguments.

bath dynamics in the limit of weak coupling. Performing a second Laplace transformation to return to the time domain, we arrive at

$$\partial_t \hat{\rho}_{\rm sys}(t) = \mathcal{L}_{\rm sys}\hat{\rho}_{\rm sys}(t) + {\rm Tr}_{\rm B}\left[\mathcal{P}\mathcal{L}_{\rm int}\int_0^\infty d\tau\; e^{(\mathcal{L}_{\rm sys}+\mathcal{L}_{\rm B})\tau}\mathcal{Q}\mathcal{L}_{\rm int}(\mathcal{P}\hat{\rho})(t-\tau)\right]. \tag{2.8}$$

We have obtained an equation of motion for the system degrees of freedom $\hat{\rho}_{\rm sys} = {\rm Tr}_{\rm B}[\hat{\rho}]$. In practice, however this equation is rather complicated to solve as it depends on its own past history, as seen in the term proportional to $\hat{\rho}(t-\tau)$. To proceed, we make the assumption that the energy scales defining the bath are much larger than those of the system, resulting in it evolving at a much faster rate than the system. In this regime, we can make use of the so-called Markov approximation and neglect the influence of past events on the evolution of the system, namely $\hat{\rho}(t-\tau) \approx \hat{\rho}(t)$. Physically, this corresponds to the bath quickly approaching the steady-state, due to its fast evolving dynamics. Hence, any internal transition in the bath, caused by system-bath interactions, will disappear before backacting on the system. Consequently, the system effectively interacts with the bath in its steady-state, in spite of any previous interacting events. In this sense, we refer to the bath being memoryless and the system dynamics being independent of its previous history.

Next we consider the interaction Hamiltonian to be of the form $\hat{H}_{\rm int} = \sum_{m,n} g_{m,n}\hat{X}_m\hat{\xi}_n$, with $\hat{X}_m$ being system operators and $\hat{\xi}_n$ bath operators. Making use of

$$e^{(\mathcal{L}_{\rm sys}+\mathcal{L}_{\rm B})\tau}\hat{O} = e^{-i\hat{H}_{\rm B}\tau}e^{-i\hat{H}_{\rm sys}\tau}\hat{O}e^{i\hat{H}_{\rm B}\tau}e^{i\hat{H}_{\rm sys}\tau} \tag{2.9}$$

and the properties (2.3), we obtain that the second term in Eq.(2.8) reduces to

$$-{\rm Tr}_{\rm B}\left\{\mathcal{P}\left[\sum_{mn} g_{mn}\hat{X}_m(0)\hat{\xi}_n(0), \left[\int_0^\infty d\tau \sum_{m'n'} g_{m'n'}\hat{X}_{m'}(-\tau)\hat{\xi}_{n'}(-\tau), \hat{\rho}_{sys}(t)\otimes\hat{\rho}_{\rm B}\right]\right]\right\}, \tag{2.10}$$

with $\hat{X}_m(t) = e^{i\hat{H}_{\rm sys}t}\hat{X}_m e^{-i\hat{H}_{\rm sys}t}$ and $\hat{\xi}_m(t) = e^{i\hat{H}_{\rm B}t}\hat{\xi}_m e^{-i\hat{H}_{\rm B}t}$. Accounting for the action of the projector $\mathcal{P}$ and performing the trace using ${\rm Tr}[\hat{\rho}_{\rm B}] = 1$ we obtain

$$\begin{aligned}\partial_t\hat{\rho}_{\rm sys}(t) = \mathcal{L}_{\rm sys}\hat{\rho}_{\rm sys}(t) - \sum_{mn}\sum_{m'n'} g_{mn}g_{m'n'}\int_0^\infty d\tau\; \Big\{&\langle\hat{\xi}_n(0)\hat{\xi}_{n'}(-\tau)\rangle[\hat{X}_m(0), \hat{X}_{m'}(-\tau)\hat{\rho}_{\rm sys}(t)] \\ &+\langle\hat{\xi}_{n'}(-\tau)\hat{\xi}_n(0)\rangle[\hat{\rho}_{\rm sys}(t)\hat{X}_{m'}(-\tau), \hat{X}_m(0)]\Big\},\end{aligned} \tag{2.11}$$

where $\langle\hat{\xi}_{n'}(t)\hat{\xi}_n(t')\rangle = {\rm Tr}_{\rm B}[\hat{\xi}_{n'}(t)\hat{\xi}_n(t')\hat{\rho}_{\rm B}]$. Note that the presence of the external bath is now fully encoded in the correlators $\langle\hat{\xi}_{n'}(t)\hat{\xi}_n(t')\rangle$. To proceed, it is necessary to make

further assumptions about the structure of the bath. A similar expression is derived in Chapter 5, when eliminating the photonic degrees of freedom in an atom-cavity system. For simplicity, we redefine the form of the interaction as $\hat{H}_{\rm int} = \sum_n g_n \left(\hat{X}_n^\dagger \hat{\xi}_n + \hat{X}_n \hat{\xi}_n^\dagger\right)$, where $\hat{X}_n$ are eigenoperators satisfying $[\hat{H}_{\rm sys}, \hat{X}_n] = \omega_n \hat{X}_n$ and $\hat{X}_n(t) = \hat{X}_n e^{-i\omega_n t}$. Following the same steps as above, we obtain

$$\begin{aligned}\partial_t \hat{\rho}_{\rm sys}(t) = \mathcal{L}_{\rm sys}\hat{\rho}_{\rm sys}(t) - \sum_{mn} g_m g_n \int_0^\infty d\tau \Big\{ &\langle \hat{\xi}_m^\dagger(0)\hat{\xi}_n(-\tau)\rangle [\hat{X}_m(0), \hat{X}_n^\dagger(-\tau)\hat{\rho}_{\rm sys}(t)] \\ &+\langle \hat{\xi}_m(0)\hat{\xi}_n^\dagger(-\tau)\rangle [\hat{X}_m^\dagger(0), \hat{X}_n(-\tau)\hat{\rho}_{\rm sys}(t)] + \langle \hat{\xi}_n(-\tau)\hat{\xi}_m^\dagger(0)\rangle [\hat{\rho}_{\rm sys}(t)\hat{X}_n^\dagger(-\tau), \hat{X}_m(0)] \\ &+\langle \hat{\xi}_n^\dagger(-\tau)\hat{\xi}_m(0)\rangle [\hat{\rho}_{\rm sys}(t)\hat{X}_n(-\tau), \hat{X}_m^\dagger(0)] \Big\}. \end{aligned} \tag{2.12}$$

Given that the correlators are considered at steady state of the bath, they are invariant under time translations. Consequently, terms oscillating at different frequencies $\omega_m \neq \omega_n$ will vary at a very fast time scale compared to the evolution of the system. We thus perform a rotating wave approximation and neglect all terms with $m \neq n$. Re-expressing the integral terms as

$$\begin{aligned} \int_0^\infty d\tau\ e^{-i\omega_n\tau}\langle \hat{\xi}_n^\dagger(-\tau)\hat{\xi}_n(0)\rangle &= \frac{1}{2}F_n + i\chi_n \qquad & \int_0^\infty d\tau\ e^{-i\omega_n\tau}\langle \hat{\xi}_n(-\tau)\hat{\xi}_n^\dagger(0)\rangle &= \frac{1}{2}G_n + i\delta_n \\ \int_0^\infty d\tau\ e^{i\omega_n\tau}\langle \hat{\xi}_n^\dagger(0)\hat{\xi}_n(-\tau)\rangle &= \frac{1}{2}F_n - i\chi_n \qquad & \int_0^\infty d\tau\ e^{i\omega_n\tau}\langle \hat{\xi}_n(0)\hat{\xi}_n^\dagger(-\tau)\rangle &= \frac{1}{2}G_n - i\delta_n \end{aligned} \tag{2.13}$$

we arrive at

$$\begin{aligned}\partial_t \hat{\rho}_{\rm sys}(t) = &- i\left[\hat{H}_{\rm sys} + \sum_n \left(\delta_n \hat{X}_n^\dagger \hat{X}_n + \chi_n \hat{X}_n \hat{X}_n^\dagger\right), \hat{\rho}_{\rm sys}(t)\right] \\ &+ \sum_n F_n \left(\hat{X}_n^\dagger \hat{\rho}_{\rm sys}(t)\hat{X}_n - \frac{1}{2}\hat{X}_n\hat{X}_n^\dagger\hat{\rho}_{\rm sys}(t) - \frac{1}{2}\hat{\rho}_{\rm sys}(t)\hat{X}_n\hat{X}_n^\dagger\right) \\ &+ \sum_n G_n \left(\hat{X}_n \hat{\rho}_{\rm sys}(t)\hat{X}_n^\dagger - \frac{1}{2}\hat{X}_n^\dagger\hat{X}_n\hat{\rho}_{\rm sys}(t) - \frac{1}{2}\hat{\rho}_{\rm sys}(t)\hat{X}_n^\dagger\hat{X}_n\right). \end{aligned} \tag{2.14}$$

This equation of motion for the density matrix is known as Lindblad master equation. The terms inside the commutator correspond to the coherent evolution of the system together with a pair of new coherent terms which arise due to the interaction with the bath. The second and third lines describe dissipative process, and make the time evolution of the density matrix non-unitary. Inside the brackets, the first term defines what type of dissipative process takes place while the second and third term ensure that the density matrix remains normalized. If we consider the first term in the second line $\hat{X}_n^\dagger \hat{\rho}_{\rm sys}\hat{X}_n = \hat{X}_n^\dagger|\psi\rangle\langle\psi|\hat{X}_n$, we observe that transitions of the state $|\psi\rangle$ are caused by the action of the

operator $\hat{X}_n^\dagger$ on it. We thus refer to $\hat{X}_n^\dagger$ as a jump operator. From the third line, we get that $\hat{X}_n$ is also a jump operator. The frequencies accompanying these terms (F_n, G_n) are denoted dissipation rates, and specify the rate at which each dissipative process occurs. From Eq. (2.14), we can understand the precise influence of the bath on the system. On the one hand, the type of system-bath interactions, given by $\hat{H}_{\text{int}}$, are what determines what additional coherent interaction emerges and which jump operators are present in the master equation. On the other hand, the structure of the bath, encoded in the correlators $\langle\hat{\xi}_n(t)\hat{\xi}_n(t')\rangle$, defines the coupling strength of the additional interactions (δ_n, χ_n) and the dissipation rates (F_n, G_n).

This concludes our derivation of the master equation. We finish by mentioning that, in general, Lindblad master equations are usually expressed in the form

$$\partial_t\hat{\rho} = \mathcal{L}\hat{\rho} = -i[\hat{H}, \hat{\rho}] + \sum_n \kappa_n \mathcal{D}[\hat{R}_n]\hat{\rho}, \tag{2.15}$$

where the superoperator $\mathcal{D}$ is denoted as the dissipator and is defined as $\mathcal{D}[\hat{R}_n]\hat{\rho} = \hat{R}_n\hat{\rho}\hat{R}_n^\dagger - \frac{1}{2}\hat{R}_n^\dagger\hat{R}_n\hat{\rho} - \frac{1}{2}\hat{\rho}\hat{R}_n^\dagger\hat{R}_n$, with $\hat{R}_n$ the jump operators and κ_n the associated dissipation rates. The superoperator $\mathcal{L}$ is commonly known as *Lindbladian* or *Liouvillian*. In the next sections, we discuss how the spectral properties of the Lindbladian $\mathcal{L}$ fully determine the dynamics of the system and point out some of the most relevant differences between Lindbladian and Hamiltonian evolution.

2.3 Properties of Lindbladian evolution

In the previous section we derived the general form of the master equation (2.15). The main property of this equation is that it is linear in $\hat{\rho}$, meaning that the general solution can be casted as

$$\hat{\rho}(t) = e^{\mathcal{L}t}\,\hat{\rho}(0). \tag{2.16}$$

In this sense, the Lindbladian is the generator of the non-unitary dynamics under which $\hat{\rho}$ evolves. More specifically, the generalized evolution superoperator $\mathcal{L}$ is a completely positive trace preserving (CPTP) map. This means that despite the evolution being non-unitary, it is always guaranteed that the density matrix is completely positive and satisfies $\text{Tr}[\hat{\rho}] = 1$. This is guaranteed even if the Lindbladian is time dependent, as long as the dissipation rates remain positive[3]. For simplicity, we will only consider the case in which

[3]If this is not the case and the dissipation rates become negative during time-evolution, the problem becomes intrinsically non-Markovian, and requires a different approach to the systems dynamics [72, 73] beyond the scope of this discussion.

all terms inside $\mathcal{L}$ are time independent.

In analogy with the spectral decomposition of the Hamiltonian unitary evolution, the same method can be applied to the Lindbladian. We define the left and right eigenmatrices as

$$\mathcal{L}\hat{v}_i = \lambda_i \hat{v}_i \qquad\qquad \hat{w}_i \mathcal{L} = \lambda_i \hat{w}_i. \tag{2.17}$$

The fact that $\hat{v}_i \neq \hat{w}_i$ follows directly from $\mathcal{L}$ being non-unitary. Note that, in general, the eigenmatrices $\hat{v}_i$ do not represent physical density matrices, meaning they do not satisfy $\mathrm{Tr}[\hat{v}_i] = 1$. Additionally, non-unitarity results in the eigenvalues λ_i being complex. Since the Lindbladian is the generator of a CPTP map, it is guaranteed that all λ_i come in complex conjugate pairs and, more importantly, they satisfy $\mathrm{Re}[\lambda_i] \leq 0$. This ensures that the system always decays to a certain steady state. From (2.17), it follows that density matrices can be represented as linear combinations of right eigenmatrices. The CPTP property then ensures that a physical initial condition $\hat{\rho}(0)$, with $\mathrm{Tr}[\hat{\rho}(0)] = 1$, will remain physical at all times despite it being decomposable as a linear combination of "unphysical" matrices.

The eigenmatrices of $\mathcal{L}$ can be classified according to the form of their respective eigenvalue (see Fig. 2.1). The real part determines the decay rate of the eigenmatrix, as $\mathrm{Re}[\lambda_i] \leq 0$, and the imaginary part its oscillation rate. Purely real eigenvalues are associated with decaying states and for the case $\mathrm{Re}[\lambda_i] = 0$, the eigenmatrix corresponds to the steady state of the system. By definition of a CPTP map it is always true that there exists at least one eigenvalue with $\lambda_i = 0$, i.e. there is always a steady state. A finite imaginary part adds oscillations to the time evolution, which in combination with decay generates states denoted as spirals [74]. Purely imaginary eigenvalues do not decay and are associated with coherences between the steady states of the system. These notions also give rise to the concept of dissipative gap Δ_d, which is defined as the eigenvalue whose real part is closest to the steady state. This parameter is also used to characterize out-of-equilibrium phase transitions, which occur when the dissipative gap closes as one parameter is varied [67]. From a computational perspective, the spectral decomposition of $\mathcal{L}$ is especially interesting as obtaining the eigenvalues and eigenmatrices of $\mathcal{L}$ fully determines the dynamical evolution of the system, providing access to all type of observables and correlation functions. Nevertheless, this is restricted to systems with small Hilbert spaces, where diagonalizing $\mathcal{L}$ is not an expensive procedure.

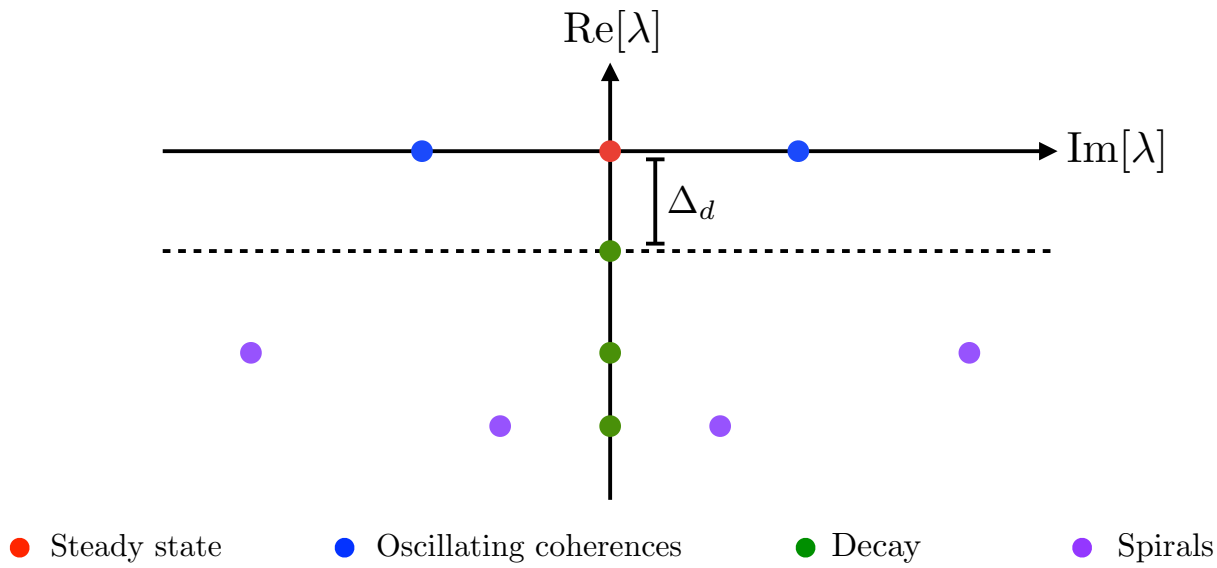

Figure 2.1: Generic spectrum of a Lindbladian super-operator. Right eigenstates are classified according to their eigenvalues λ. If $\mathrm{Re}(\lambda) < 0$, $\mathrm{Im}(\lambda) = 0$, the states will decay in time (green dots). If $\mathrm{Re}(\lambda) < 0$, $\mathrm{Im}(\lambda) \neq 0$, the states will show oscillatory behavior as they decay (purple dots). If $\mathrm{Re}(\lambda) = 0$, $\mathrm{Im}(\lambda) \neq 0$, the states will survive in the long time limit but will present an oscillatory behavior (blue dots). If $\mathrm{Re}(\lambda) = \mathrm{Im}(\lambda) = 0$, the states will not present any variation as time evolves, thus becoming the steady states of the system (red dot). The value Δ_d corresponds to the so-called dissipation gap which separates the steady state from the state with slowest decay rate.

2.4 Symmetries and conserved quantities

To finalize this chapter we discuss a few differences between Lindbladian and Hamiltonian evolution in what concerns symmetries and conserved quantities. These differences have been addressed in detail by Albert and Jiang in [74]. Here, we outline the main points of their discussion and refer the reader to [74] for details. In order to define conserved quantities, we first need to introduce the equations of motion for operators in the Lindbladian formalism. This can be done by examining the time evolution for the average value of an observable $\hat{O}$

$$\begin{aligned}
\partial_t \langle \hat{O} \rangle =& \mathrm{Tr}[\hat{O} \partial_t \hat{\rho}] \\
=& \mathrm{Tr}\left\{ \hat{O}(-i)[\hat{H}, \hat{\rho}] + \sum_n \kappa_n \left(\hat{O} \hat{R}_n \hat{\rho} \hat{R}_n^\dagger - \frac{1}{2} \hat{R}_n^\dagger \hat{R}_n r\hat{h}o - \frac{1}{2} \hat{\rho} \hat{R}_n^\dagger \hat{R}_n \right) \right\} \\
=& \mathrm{Tr}\left\{ \left[i[\hat{H}, \hat{O}] + \sum_n \kappa_n \left(\hat{R}_n^\dagger \hat{O} \hat{R}_n - \frac{1}{2} \hat{R}_n^\dagger \hat{R}_n \hat{O} - \frac{1}{2} \hat{O} \hat{R}_n^\dagger \hat{R}_n \right) \right] \hat{\rho} \right\},
\end{aligned} \tag{2.18}$$

where we employed the cyclic property of the trace in the third line. We thus obtain an equation of motion for operators

$$\partial_t \hat{O} = \mathcal{L}^\dagger \hat{O} = i[\hat{H}, \hat{O}] + \sum_n \kappa_n \left(\hat{R}_n^\dagger \hat{O} \hat{R}_n - \frac{1}{2} \hat{R}_n^\dagger \hat{R}_n \hat{O} - \frac{1}{2} \hat{O} \hat{R}_n^\dagger \hat{R}_n \right), \tag{2.19}$$

which is usually denoted adjoint equation. This is an extension of the Heisenberg equation of motion to open systems[4].

For closed systems, a specific observable $\hat{J}$ is a conserved quantity if and only if it commutes with the Hamiltonian $[\hat{H}, \hat{J}] = 0$. By virtue of Noether's theorem, the conserved quantity is also a generator of a symmetry of the system defined by the operator $\hat{U} = e^{i\varphi \hat{J}}$, By a symmetry of the system, we mean $\hat{U}$ satisfies $\hat{U}^\dagger \hat{H} \hat{U} = \hat{H}$, which is also true if and only if $[\hat{H}, \hat{J}] = 0$. This establishes a direct relation between the presence of conserved quantities, the presence symmetries and the commutator with $\hat{H}$ being equal to zero. This is no longer true when the system is open and the evolution of operators is given by the adjoint equation (2.19).

First thing to note is that when an operator commutes with $\hat{H}$ and all the jump operators $\hat{R}_n$, it is a conserved quantity $\partial_t \hat{J} = 0$. Importantly, this is not a necessary condition for a quantity to be conserved, as it is possible that for certain operators dissipative channels might cancel with each other. Note that conserved quantities have an interpretation as left eigenmatrices of $\mathcal{L}$ with eigenvalue zero, as they obey $\mathcal{L}^\dagger \hat{J} = (\hat{J}\mathcal{L})^\dagger = 0$.

For open systems, it is possible to define a symmetry of the system as $\mathcal{U}^\dagger \mathcal{L} \mathcal{U} = \mathcal{L}$, where $\mathcal{U} = e^{i\varphi \mathcal{J}}$ is a superoperator defined by the generator $\mathcal{J}$ which is in turn a superoperator defined by $\hat{J}$. At the superoperator level $\hat{J}$ will generate a symmetry of the open system if $[\mathcal{L}, \mathcal{J}] = 0$. By mapping the superoperators into $N^2 \times N^2$ dimensional matrices[5], with N the size of the Hilbert space,

$$\begin{aligned} \hat{\mathcal{L}} =& -i \left(\hat{H} \otimes \mathbb{1} - \mathbb{1} \otimes \hat{H}^* \right) - \sum_n \kappa_n \left(\hat{R}_n \otimes \hat{R}_n^* - \hat{R}_n^\dagger \hat{R}_n \otimes \mathbb{1} - \mathbb{1} \otimes (\hat{R}_n^\dagger \hat{R}_n)^* \right) \\ \hat{\mathcal{J}} =& \hat{J} \otimes \mathbb{1} - \mathbb{1} \otimes \hat{J}^*, \end{aligned} \tag{2.20}$$

we obtain that the conditions to satisfy $[\mathcal{L}, \mathcal{J}] = 0$ are

[4] It is worth noting that other approaches, such as Langevin equations [59], typically include a noise term. This term is absent in Eq. (2.19) as it results from the ensemble average characterizing the density matrix formalism.

[5] In this picture, density matrices become N^2 column vectors. This is a typical strategy to encode the dynamics of open systems when approaching the problem numerically [75].

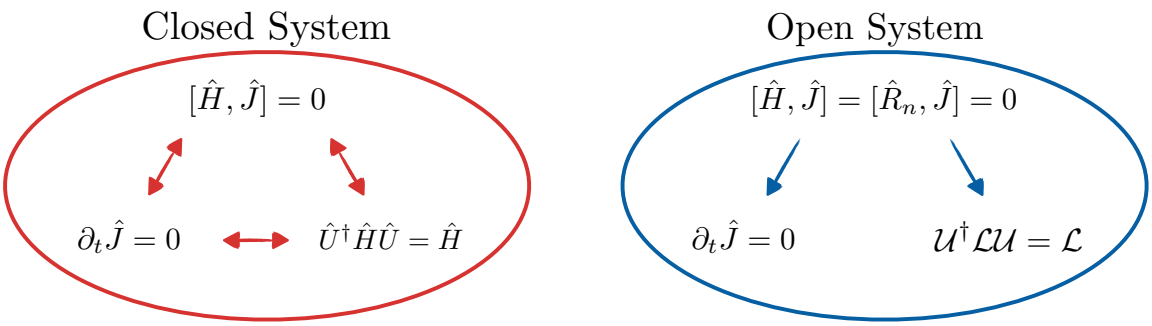

Figure 2.2: Schematic comparison of the relation between symmetries and conserved quantities for closed and open systems, adapted from Ref. [74].

$$\sum_n \kappa_n [\hat{R}_n, \hat{J}] \otimes \hat{R}_n^* - \hat{R}_n \otimes [\hat{R}_n^*, \hat{J}^*] = 0$$
$$\sum_n \kappa_n [\hat{R}_n^\dagger \hat{R}_n, \hat{J}] = [\hat{H}, \hat{J}] = 0. \tag{2.21}$$

From these expressions we observe that if the observable $\hat{J}$ satisfies $[\hat{R}_n, \hat{J}] = [\hat{H}, \hat{J}] = 0$, both conditions are automatically satisfied as well, thus meaning that $\hat{J}$ is a generator of a symmetry of the system. It is the case again that the converse is not true. The conditions (2.21) can still be satisfied if $[\hat{H}, \hat{J}] = 0$ and $[\hat{R}_n, \hat{J}] = \zeta_n$, with $\zeta_n \in \mathbb{R}$. In this case $\hat{J}$ still generates a symmetry despite it not commuting with both Hamiltonian and jump operators. Lastly, this means that $\hat{J}$ can generate a symmetry without having to be a conserved quantity. Moreover, if $\hat{J}$ is a conserved quantity which does not obey $[\hat{R}_n, \hat{J}] = [\hat{H}, \hat{J}] = 0$, there is no guarantee that the conditions (2.21) will be satisfied, meaning that conserved quantities are not in general generators of symmetries for open systems. These results are summarized schematically in Fig. 2.2.

This completes our introduction to open quantum systems and Lindblad master equations. In the following chapters we will make use of the master equation as introduced in (2.15) to describe the effects of photon losses in atom cavity systems. In particular, the derivation presented in Sec. 2.2 will be the basis to construct an effective master equation in chapter 5, where we are interested in adiabatically eliminating the photonic degrees of freedom.

3

Emergence of continuous rotational symmetries in ultracold atoms coupled to optical cavities

3.1 Introduction

In Chapter 1, we presented atom-cavity systems as an interesting platform for the quantum simulation of many-body systems. We put special emphasis on the presence of a self-organization phase transition [41–44], resulting from a $\mathbb{Z}_2$ symmetry breaking due to atom-cavity interactions [39]. This phenomenon was observed experimentally in [23], where the high degree of control allowed for the study of the symmetry breaking process [48], measurement of the excitation spectrum [50], and real-time observation of the fluctuations [51, 53].

Recent work has brought these ideas to a higher level of complexity by considering the effects of coupling a second cavity to the atomic cloud [28]. The combined system inherits an overall $\mathbb{Z}_2 \times \mathbb{Z}_2$ symmetry, where each $\mathbb{Z}_2$ symmetry can be broken separately, yielding a superradiant state in one of the cavities. More importantly, it was found that when the cavities are coupled symmetrically to the atoms, the system exhibits an overall continuous $U(1)$ symmetry, which upon breaking, leads to the presence of superradiant emission in both cavities simultaneously. These results were corroborated by the observation of the associated Goldstone and Higgs modes [29]. Further studies have also considered the robustness of this symmetry [76] and the effects of inter-cavity photon scattering processes on the ground state phase diagram [30, 77].

Symmetry enhancement of this type was previously discussed in the context of circuit

QED [78] and for atoms coupled to two-mode cavities [79], which has recently been analyzed in detail for generic atom-light couplings and including the effects of photon loss [80]. These systems exhibit complex ground and steady state phase diagrams, including multicritical points, and qualitatively different phases, resulting from the different underlying symmetries and their spontaneous breaking. With the emergence of these rich phenomena, it is intriguing to ask what other symmetries can arise for atom-cavity systems when further increasing their complexity, given their strong potential as quantum simulators.

In this chapter, we explore the consequences of adding a third cavity mode into a setup similar to the one in [28]. The results of our work have been published in [2]. In Sec. 3.2, we present an effective low-energy model of the system, analogous to the effective model derived in Sec. 1.2.2. We discuss the properties of the model in Sec. 3.3. We show that the system possesses a $\mathbb{Z}_2 \times \mathbb{Z}_2 \times \mathbb{Z}_2$ symmetry, which cannot only be combined to form the previously observed $U(1)$ symmetry, but also yields a global $SO(3)$ rotational symmetry when all cavities are coupled symmetrically to the atomic cloud. We additionally find that this generalizes to an $SO(n)$ symmetry when the atoms are symmetrically coupled to n cavities. In Sec. 3.4, we obtain the ground state phase diagram of the system using a mean-field approximation and characterize the emergent phases resulting from the spontaneous breaking of the different symmetries. We complement this analysis in Sec. 3.5 by calculating the excitation spectrum and studying its behavior when crossing the different critical points present in the system. In Sec. 3.6, we discuss the possible self-organized structures of the atoms in the different phases. We conclude in Sec. 3.7. Lastly, in Appendices 3.A and 3.B, we provide further details regarding the derivation of the effective model presented in Sec. 3.2 and the bilinear Hamiltonian from which the excitation spectrum is extracted in Sec. 3.5.

3.2 Model

We consider a system of three intersecting single-mode optical cavities, symmetrically aligned in the x-z plane, with a gas of ultracold atoms forming a Bose-Einstein condensate (BEC) placed in the center, see Fig. 3.1. The system is pumped by a circularly polarized laser in the y direction, which is reflected off a mirror, generating a standing wave potential for the atoms. Two-photon scattering processes between the pump and the cavities mediate momentum transitions for the atoms from the $|\vec{k}_0\rangle$ BEC state into a set of twelve excited states $|\vec{k}^{(i)} = \pm(\vec{k}_p \pm \vec{k}_c^{(i)})\rangle$, with $\vec{k}_p$ and $\vec{k}_c^{(i)}$ the wave vectors of the pump and cavity i, respectively. For the case $|\vec{k}_c^{(i)}| = |\vec{k}_p| = k$, these excited states

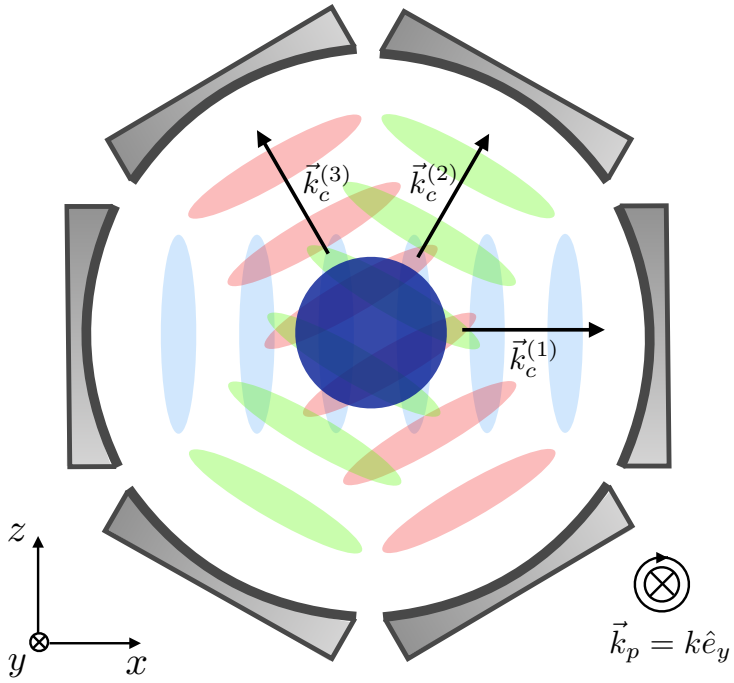

Figure 3.1: A gas of ultracold atoms in a BEC state (blue circle) is placed at the intersection of three high-finesse single-mode optical cavities, which are all located in the x-z plane and aligned at the same angle from each other, with wave vectors $\vec{k}_c^{(1)} = k\hat{e}_x$, $\vec{k}_c^{(2)} = \frac{k}{2}(\hat{e}_x + \sqrt{3}\hat{e}_z)$ and $\vec{k}_c^{(3)} = \frac{k}{2}(-\hat{e}_x + \sqrt{3}\hat{e}_z)$. An external circularly polarized laser, which is reflected off a mirror not shown in the figure, drives the atoms from the transverse direction, resulting in two-photon scattering processes between the cavity modes and the drive, mediated by atomic momentum transitions.

become degenerate, yielding a low-energy description which in the rotating frame of the pump reads

$$\hat{H} = \sum_{i=1}^{3}(-\Delta_i)\hat{a}_i^\dagger\hat{a}_i + \omega\hat{b}_i^\dagger\hat{b}_i + \frac{\lambda_i}{\sqrt{N}}(\hat{a}_i^\dagger + \hat{a}_i)\left(\hat{b}_i^\dagger\hat{b}_0 + \hat{b}_0^\dagger\hat{b}_i\right), \tag{3.1}$$

where $\hat{a}_i$ is the annihilation operator for photons in cavity i, with $\Delta_i = \omega_p - \omega_c$ the cavity-pump detuning, $\hat{b}_0$ and $\hat{b}_i$ are bosonic annihilation operators for atoms in the $|\vec{k}_0\rangle$ and the $|\vec{k}^{(i)}\rangle$ states, respectively, and ω is the energy difference between $|\vec{k}_0\rangle$ and $|\vec{k}^{(i)}\rangle$. The interaction term corresponds to transitions between $|\vec{k}_0\rangle$ and $|\vec{k}^{(i)}\rangle$ mediated by the emission or absorption of a photon in cavity i, with strength $\lambda_i/\sqrt{N}$, where N is the total number of atoms in the system. We focus on the case where $\Delta_i = \Delta < 0$ for all i, and use the coupling strengths λ_i as control parameters. The derivation of the Hamiltonian (3.1) is analogous to the one for the single cavity case in Eq. (1.12), and the precise steps are presented in Appendix 3.A.

3.3 Symmetries

For generic λ_i, the Hamiltonian (3.1) possesses a $\mathbb{Z}_2 \times \mathbb{Z}_2 \times \mathbb{Z}_2$ symmetry, associated with parity transformations of the form

$$\left(\hat{a}_i, \hat{a}_i^\dagger, \hat{b}_i, \hat{b}_i^\dagger\right) \longrightarrow -\left(\hat{a}_i, \hat{a}_i^\dagger, \hat{b}_i, \hat{b}_i^\dagger\right), \tag{3.2}$$

for $i = 1, 2, 3$. If two of the cavities have the same coupling strength $\lambda_1 = \lambda_2 = \lambda \neq \lambda_3$, their corresponding $\mathbb{Z}_2 \times \mathbb{Z}_2$ is combined into a $U(1)$ symmetry associated with rotations between the degrees of freedom of cavities 1 and 2

$$\begin{pmatrix} \hat{a}_1 \\ \hat{a}_2 \end{pmatrix} \to \hat{\mathcal{R}}_\theta \begin{pmatrix} \hat{a}_1 \\ \hat{a}_2 \end{pmatrix}, \qquad \begin{pmatrix} \hat{b}_1 \\ \hat{b}_2 \end{pmatrix} \to \hat{\mathcal{R}}_\theta \begin{pmatrix} \hat{b}_1 \\ \hat{b}_2 \end{pmatrix}, \tag{3.3}$$

with $\hat{\mathcal{R}}_\theta$ a rotation matrix

$$\hat{\mathcal{R}}_\theta = \begin{pmatrix} \cos\theta & -\sin\theta \\ \sin\theta & \cos\theta \end{pmatrix}. \tag{3.4}$$

The overall symmetry of the system then becomes $U(1) \times \mathbb{Z}_2$. For the case $\lambda_i = \lambda$ for all i, the Hamiltonian becomes invariant under the transformation $\hat{\mathcal{R}}_\theta$ acting on any pair of cavities. For three cavities, we can associate this invariance to a global $SO(3)$ symmetry, corresponding to the three possible rotations between cavities.

By tuning the coupling strengths, we can then interpolate between the regimes where the system acquires different symmetries, which can be spontaneously broken separately. As explained in Chapter 1, the breaking of a discrete $\mathbb{Z}_2$ symmetry is associated with the system undergoing a superradiant phase transition. This means that one of the cavities acquires a macroscopic occupation number, and that the atomic cloud self-organizes into a checkerboard pattern, resulting from the interference between the pump and the macroscopic cavity field [23, 46, 81]. In the case of a $U(1)$ symmetry breaking, the light field amplitude is arbitrarily spread between the two symmetrical cavities due to the ground state degeneracy, with the self-organization pattern given by the interference between the pump and the two cavity fields [28]. This is shown in Fig. 3.5.

As discussed in the next section, the same occurs when the emergent $SO(3)$ symmetry is broken, but with the light field amplitude spread among the three cavities instead. In the following, we make these notions precise by studying the phase diagram using a mean-field approach, obtaining the excitation spectrum, and analyzing the self-organization of the atoms due to the light-field interference.

3.4 Mean-field phase diagram

We obtain the ground state phase diagram making use of the mean-field approximation which is valid in the thermodynamic limit $N \to \infty$. We start by introducing the order parameters $\alpha_i = \langle \hat{a}_i \rangle$ and $\beta_i = \langle \hat{b}_i \rangle$ into Eq. (3.1)

$$E_{\mathrm{MF}} = \sum_{i=1}^{3}(-\Delta)|\alpha_i|^2 + \omega|\beta_i|^2 + \frac{\lambda_i}{\sqrt{N}}\left(\alpha_i + \alpha_i^*\right)\left(\beta_i + \beta_i^*\right)\sqrt{N - \sum_{j=1}^{3}|\beta_j|^2}, \tag{3.5}$$

where we factorized the two-point correlators as $\langle \hat{a}^\dagger \hat{a} \rangle \approx \langle \hat{a}^\dagger \rangle \langle \hat{a} \rangle$ and made use of particle number conservation $|\langle \hat{b}_0 \rangle|^2 = N - \sum_{j=1}^{3}|\beta_j|^2$. Minimizing the energy with respect to the cavity field leads to $\alpha_i = -\frac{\lambda_i}{(-\Delta)\sqrt{N}}\left(\beta_i + \beta_i^*\right)\sqrt{N - \sum_{j=1}^{3}|\beta_j|^2}$, resulting in

$$E_{\mathrm{MF}} = \sum_{i=1}^{3}\omega|\beta_i|^2 - \lambda_i^2\frac{(\beta_i + \beta_i^*)^2}{(-\Delta)N}\left(N - \sum_{j=1}^{3}|\beta_j|^2\right). \tag{3.6}$$

Next, minimizing E_{MF} with respect to the imaginary part of β_i, we further obtain $\mathrm{Im}[\beta_i] = 0$, yielding

$$E_{\mathrm{MF}} = \omega\left(\sum_{i=1}^{3}\frac{\mu_i - 1}{\mu_i}\beta_i^2 + \frac{1}{N}\sum_{i,j=1}^{3}\frac{\beta_i^2\beta_j^2}{\mu_i}\right), \tag{3.7}$$

with $\mu_i = \lambda_{\mathrm{cr}}^2/\lambda_i^2$, where $\lambda_{\mathrm{cr}} = \frac{\sqrt{(-\Delta)\omega}}{2}$ is the critical coupling strength. The ground state phase diagram of the system then follows from the global minima of E_{MF} as a function of the parameters λ_i. This yields four different phases, shown in Fig. 3.2, which we denote as normal (NP), single cavity superradiant (S1), double cavity superradiant (S2) and triple cavity superradiant (S3):

- (NP) - For all $\lambda_i < \lambda_{\mathrm{cr}}$, the only minimum of E_{MF} is the trivial solution, $\beta_i = 0$ for all i, where there is no macroscopic occupation in any cavity and the atoms remain in the BEC state.

- (S1) - For $\lambda_i > \lambda_{\mathrm{cr}}$ and $\lambda_i > (\lambda_j, \lambda_k)$, one of the $\mathbb{Z}_2$ symmetries is spontaneously broken and the energy develops two minima at $\beta_i = \pm\sqrt{\frac{N}{2}(1 - \mu_i)}$, $\beta_j = \beta_k = 0$, corresponding to the two possible self-organized patterns and the presence of a macroscopic light field in cavity i.

- (S2) - For $\lambda_i = \lambda_j = \lambda > \lambda_{\mathrm{cr}}$ and $\lambda > \lambda_k$, the minima of E_{MF} correspond to a

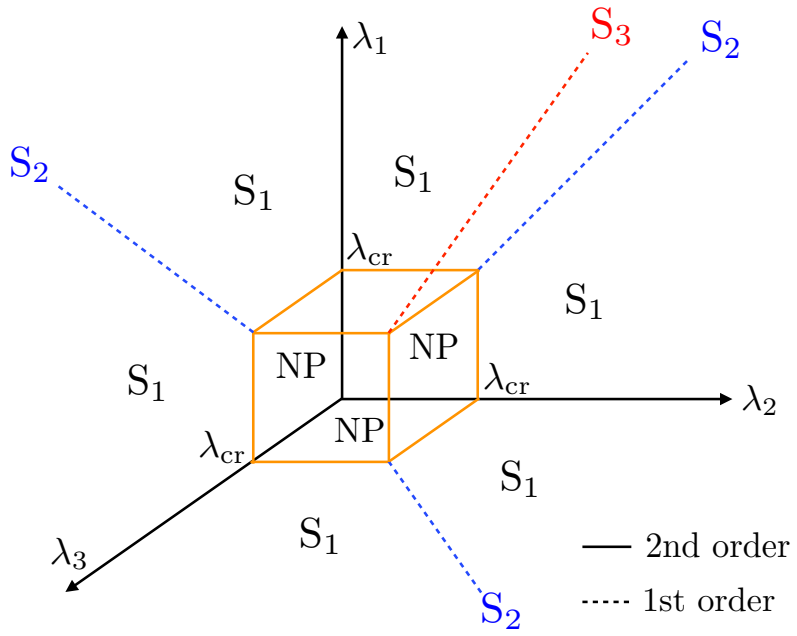

Figure 3.2: Mean-field ground state phase diagram of the system as a function of the atom-light couplings λ_i, resulting from the minima of E_{MF} (3.7). The orange cubic region where all $\lambda_i < \lambda_c$ corresponds to the normal phase (NP). The regions with $\lambda_i > \lambda_{cr}$ and $\lambda_i > (\lambda_j, \lambda_k)$ are associated with single cavity superradiance (S1). Blue lines denote the edge of the planes with $\lambda_j = \lambda_k = \lambda > \lambda_{cr}$ and $\lambda > \lambda_i$, where the broken $U(1)$ symmetry yields superradiance in two cavities (S2). The diagonal red line denotes the region $\lambda_i = \lambda > \lambda_{cr}$, for all i, where the spontaneous SO(3) symmetry breaking leads to superradiance in all cavities (S3). Solid and dashed lines correspond to second- and first-order phase transitions, respectively.

circumference in the β_i-β_j plane, parametrized by

$$\begin{pmatrix} \beta_i \\ \beta_j \end{pmatrix} = \sqrt{\frac{N}{2}(1-\mu)} \begin{pmatrix} \cos\theta \\ \sin\theta \end{pmatrix}, \tag{3.8}$$

with $\beta_k = 0$. This is associated with the spontaneous breaking of the continuous $U(1)$ symmetry, where two cavities become superradiant and the relative distribution of light intensity is given by the angle θ.

- (S3) - For all $\lambda_i = \lambda > \lambda_{cr}$, all modes become macroscopically occupied and the energy minima span a spherical surface in order parameter space, parametrized by

$$\begin{pmatrix} \beta_1 \\ \beta_2 \\ \beta_3 \end{pmatrix} = \sqrt{\frac{N}{2}(1-\mu)} \begin{pmatrix} \cos\phi \\ \sin\phi\cos\theta \\ \sin\phi\sin\theta \end{pmatrix}. \tag{3.9}$$

This triple superradiant phase emerges from the spontaneous breaking of the $SO(3)$ symmetry, where the two angles (ϕ, θ) parametrize the distribution of light intensity.

In all superradiant phases, the cavity field intensity $\alpha^2 = \sum_i \alpha_i^2 \propto \beta^2 = \sum_i \beta_i^2$ is fully determined by the driving strength, encoded in λ_i, and the total number of atoms in the system. Physically, this follows from the amount of photons present in the system being fixed by the amount of photons scattered from the pump. Crucially, we note that different ground states of a superradiant phase feature the same cavity field intensity. Therefore, they are connected by transformations that preserve the value of α^2. Geometrically, in $n > 1$ dimensions, such transformations correspond to proper rotations (and parity transformations in the single cavity case $n = 1$), which are the generators of the $SO(n)$ group. Thus, for the generic case of symmetrical coupling of the atoms to n different cavities, this results in an overall $SO(n)$ symmetry. The emergence of rotational symmetries in the system can then be understood as the ground states of a superradiant phase conserving the total field intensity, and being related to each other only by a redistribution of the light field among the different cavity modes.

In Fig. 3.3, we show the ground state manifold as a function of the order parameters for the four different phases. We find that all transitions from the normal phase into any of the superradiant ones are of second order, as the order parameters continuously move from zero to a finite value when the system crosses the phase boundary. In contrast, for transitions among superradiant phases, the order parameters change discontinuously at the critical points. Following Refs. [78, 79], we refer to these transitions as being first order. Note that, unlike usual first order phase transitions, due to the change in ground state topology at the critical points, the system does not exhibit any latent heat nor hysteresis.

3.5 Excitation spectrum

Following the methods in Refs. [39, 78], the spectrum of fluctuations can be obtained by linearizing the operators in Eq. (3.1) around their mean-field value, i.e. $\hat{a}_i \to \hat{c}_i + \alpha_i$, $\hat{b}_i \to \hat{d}_i - \beta_i$, and neglecting terms of order $\mathcal{O}(\frac{1}{N})$, with the fluctuations $(\hat{c}_i,\hat{d}_i)$ being of order $\mathcal{O}(1)$. This yields a bilinear Hamiltonian in the fluctuations $(\hat{c}_i,\hat{d}_i)$ from which the spectrum can be extracted using a Bogoliubov transformation, see Appendix 3.B for

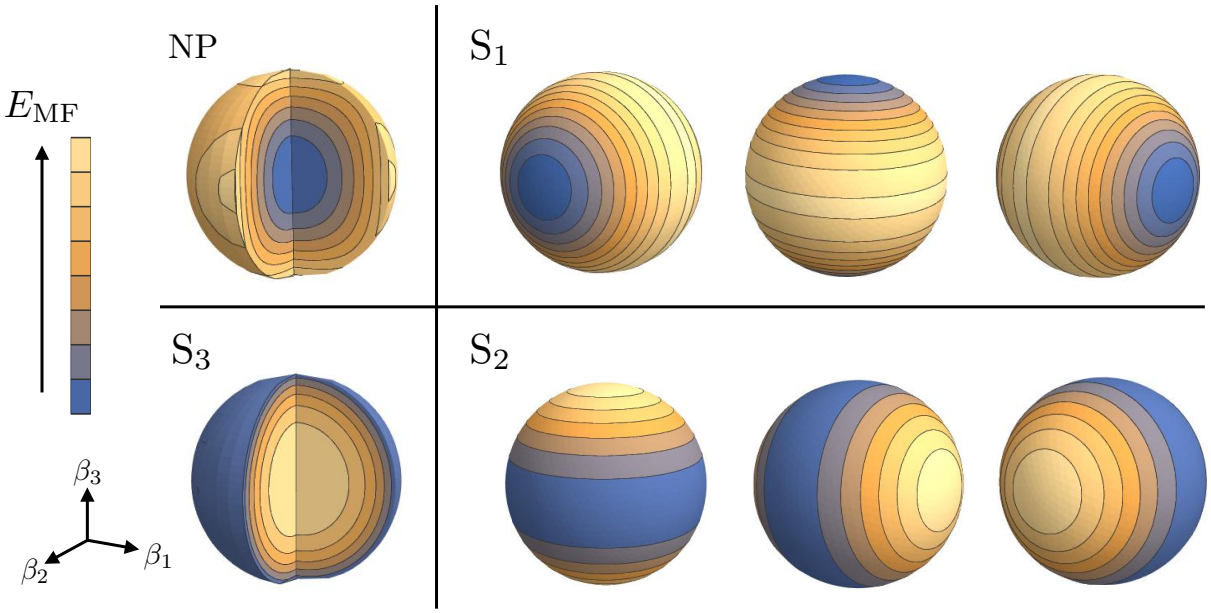

Figure 3.3: The mean-field energy (3.7) as a function of the order parameters $\beta_{1,2,3}$ for the four different phases. The energy minimum (blue region) sits at the origin in the NP, and its position becomes non-vanishing in the ordered phases. In the S1 phase, the three solutions correspond to one of the cavities becoming superradiant, and for the S2 phase to one pair of cavities becoming superradiant simultaneously, where different points in the ground state manifold are associated with different intensity distributions between the cavities. In the S3 phase, all cavities become superradiant and the ground state manifold corresponds to a spherical surface where the different ground states can also be associated with different intensity distributions.

details. In the normal and S1 phases, the spectrum reads

$$\varepsilon^{(i)2}_{\mathrm{NP},\pm} = \frac{1}{2}\left[\Delta^2 + \omega^2 \pm \sqrt{(\Delta^2-\omega^2)^2 - 16\lambda_i^2\Delta\omega}\right], \tag{3.10}$$

$$\varepsilon^{(i)2}_{\mathrm{S1},\pm} = \frac{1}{2}\left[\frac{\omega^2}{\mu_i^2} + \Delta^2 \pm \sqrt{\left(\frac{\omega^2}{\mu_i^2} - \Delta^2\right)^2 + 4\omega^2\Delta^2}\right], \tag{3.11}$$

$$\tilde{\varepsilon}^{(j\neq i),2}_{\mathrm{S1},\pm} = \frac{1}{2}\Bigg[\Delta^2 + \frac{\omega^2}{4\mu_i^2}(1+\mu_i)^2 \pm \sqrt{\left(\Delta^2 - \frac{\omega^2}{4\mu_i^2}(1+\mu_i)^2\right)^2 + 4\lambda_j^2\Delta\frac{\omega}{\mu_i}(1+\mu_i)^2}\Bigg], \tag{3.12}$$

where we considered cavity i to be in the superradiant state. These excitation spectra are shown in Fig. 3.4(a), where we observe how the lowest energy branch vanishes at the critical point between the NP and the S1 phases, to increase again in the S1 phase, as expected from the spontaneous breaking of a discrete symmetry. The dependence of (3.12)

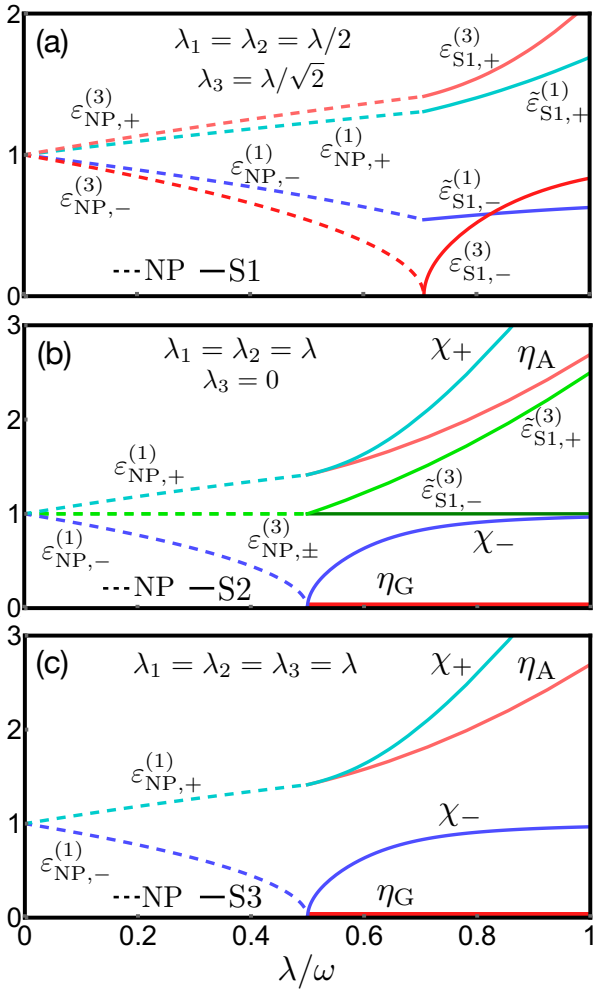

Figure 3.4: Excitation spectrum (in units of ω) when crossing the transitions from: (a) NP to S1, (b) NP to S2 and (c) NP to S3. In (b) and (c) we observe the emergence of Goldstone modes, resulting from the spontaneous breaking of the continuous symmetries $U(1)$ and $SO(3)$, respectively. In all cases, we have chosen $\omega = -\Delta$ for simplicity, but the results are independent of the parameter choice as long as $\Delta < 0$.

on λ_i, through $\mu_i = \lambda_{\mathrm{cr}}^2/\lambda_i^2$, stems from the transition boundaries to other superradiant phases also being dependent on λ_i (blue lines in Fig. 3.2). In the S2 phase, the excitation branches of the cavity that remains in the normal phase correspond to $\tilde{\varepsilon}^{(j)}_{\mathrm{S1},\pm}$, whereas the superradiant branches mix, yielding

$$\eta_{\mathrm{G}}^2 = 0 \tag{3.13}$$

$$\eta_{\mathrm{A}}^2 = \frac{1}{4\Delta^2}\left(4\Delta^4 + 16\lambda^4 - 8\lambda^2\Delta\omega + \Delta^2\omega^2\right) \tag{3.14}$$

$$\chi_{\pm}^2 = \frac{1}{2\Delta^2}\left(\Delta^4 + 16\lambda^4 \pm \sqrt{(\Delta^4 - 16\lambda^4)^2 + 4\Delta^6\omega^2}\right), \tag{3.15}$$

where $\eta_{\mathrm{G,A}}$ correspond to the Goldstone and amplitude modes, respectively, associated with the breaking of the continuous $U(1)$ symmetry. This can be observed in Fig. 3.4(b), with the appearance of a vanishing mode (η_G) as the gap closes at the critical point. One can also see how the energies in Eqs. (3.13)-(3.15) result from the mixing of the superradiant cavity modes, as the excitations for the non-superradiant cavity (solid green lines) emerge from the branches of the same cavity in the normal phase (dashed green lines). For the S3 phase, the mode mixing leads to the same spectrum of the S2 phase, where now the $\eta_{\mathrm{G,A}}$ modes become double degenerate instead. This is shown in Fig. 3.4(c), where the excitations associated with a non-superradiant cavity in (b) are not present any more. The increase in the number of Goldstone modes follows from the spontaneous breaking of a higher dimensional symmetry, namely $SO(3)$, and can be understood as excitations along the angular directions of the ground state manifold.

3.6 Self-organization in the S3 phase

Superradiance is accompanied by atomic self-organization, where the atoms sit at the minima of the effective potential generated by the interference between the pump and the cavity light fields. In this section, we present the self-organized patterns that arise in the S3 superradiant phase. The total effective potential reads

$$V(\vec{x}) = \left[\Omega_p \cos(ky) + \sum_{i=1}^{3} \Omega_i \cos(\vec{k}_c^{(i)}\vec{x} + \varphi_i)\right]^2, \tag{3.16}$$

where $\Omega_{(p,i)} = \sqrt{U_{(p,i)}}$ are the pump and cavity amplitudes, respectively, with $U_{(p,i)}$ the potential depths (see Appendix 3.A), φ_i are the phases of each cavity field, and the cavity wave vectors are defined as $\vec{k}_c^{(1)} = k\hat{e}_x$, $\vec{k}_c^{(2)} = \frac{k}{2}(\hat{e}_x + \sqrt{3}\hat{e}_z)$ and $\vec{k}_c^{(3)} = \frac{k}{2}(-\hat{e}_x + \sqrt{3}\hat{e}_z)$, as shown in Fig. 3.1. By choosing the origin of coordinates appropriately, we can set $\varphi_1 = 0$. In Fig. 3.5, we present four two-dimensional cuts of $V(\vec{x})$, for the self-organized atoms in the S3 phase, where the amplitudes are distributed according to $\Omega_1 = \Omega_c \cos\phi$, $\Omega_2 = \Omega_c \sin\phi \sin\theta$ and $\Omega_3 = \Omega_c \sin\phi \cos\theta$, for the case $\varphi_2 = \varphi_3 = 0$. We have additionally chosen the angles ϕ and θ to display the lattice structure in the other two superradiant phases. For clarity, the selected values correspond to the case where the cavity amplitudes contribute equally to the total potential. For $\varphi_2 = \varphi_3 = 0$, considering other values of ϕ and θ only modifies the lattice depth, but the position of the extremal points is fixed. In (a), we show the potential for the S1 phase, where cavity 1 is in the superradiant state. The atoms form a checkerboard pattern in the x-y plane (not shown) but are free in the z direction. Panel (b) corresponds to the S2 phase, where cavity 1 and 3 are superradiant.

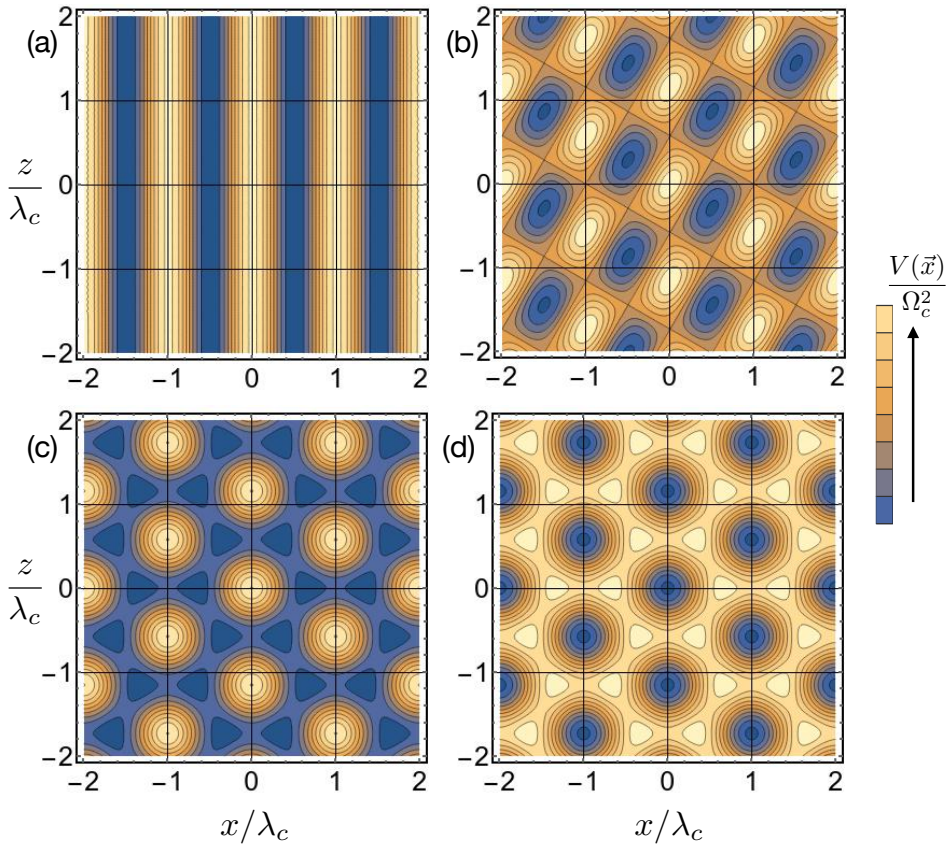

Figure 3.5: Two-dimensional cuts ($y = 0$) of the effective potential $V(\vec{x})$ generated by the light fields for $\varphi_2 = \varphi_3 = 0$ and $\Omega_p = 10\Omega_c$, in the S3 phase corresponding to: (a) $\phi = 0$, $\theta = 0$ (equivalent to the S1 phase); (b) $\phi = \pi/4$, $\theta = 0$ (equivalent to the S2 phase); (c) $\phi = \arctan(\sqrt{2})$, $\theta = \pi/4$; and (d) $\phi = \pi - \arctan(\sqrt{2})$, $\theta = 3\pi/4$.

In this case, the atoms arrange in a rhomboidal lattice with lattice constant $2\lambda_c/\sqrt{3}$, being λ_c the cavity wavelength. Finally, in (c) and (d), we present the potentials for the S3 phase, where all cavities are superradiant, for two situations where minima and maxima are exchanged. In both cases, the resulting structure is a hexagonal lattice, with lattice constant $2\lambda_c/3$ in (c) and $2\lambda_c/\sqrt{3}$ in (d). This set of qualitatively different self-organized structures is a consequence of the high complexity of the system, namely, the interference between the three different cavity modes.

For generic $\varphi_{2,3}$, the position of the atoms is shifted around when varying ϕ and θ. For example, if we consider a fixed value of ϕ and vary θ continuously, the position of the atoms is smoothly translated along the z axis. More specifically, for $x = 0$ and $\varphi_2 - \varphi_3 = \pi/2$, we obtain $V(z) = \left[\Omega_p + \Omega_c \cos(\phi) + \Omega_c \sin(\phi) \cos\left(\theta + \varphi_3 + \frac{\sqrt{3}}{2} kz\right)\right]^2$, in direct analogy with the results discussed in Ref. [28], where the continuous translation is directed along the axis perpendicular to the external pump. In Ref. [28], this translation is a direct consequence of the $U(1)$ symmetry resulting from the system being invariant

under rotations between cavities 1 and 2. In our case, the $SO(3)$ symmetry corresponds to invariance under rotations between cavities i and j, for any pair (i, j). We can then associate these rotations with continuous translations along the direction perpendicular to the wave vector of the cavity that is left invariant. Therefore, the $SO(3)$ symmetry can be interpreted as three different continuous translations of the atomic positions, along the directions perpendicular to each one of the cavity wave vectors. As a result, the potential can be located anywhere in the x-z plane. Thus, we can associate the presence of the two Goldstone modes in the S3 phase with the breaking of two continuous translational symmetries.

3.7 Conclusion

In this chapter, we have studied the interaction between a gas of ultracold atoms and three single-mode optical cavities, in the presence of transverse pumping. We showed that the $\mathbb{Z}_2$ symmetries associated with each cavity-atom coupling can be combined, not only into a $U(1)$ symmetry, but also into a rotational $SO(3)$ symmetry, which in the case of n different single-mode resonators generalizes to an $SO(n)$ symmetry. Using the mean-field approximation, we calculated the ground state phase diagram and obtained that spontaneous breaking of this symmetry led to a phase transition into a state where all cavities become superradiant. The continuous manifold of degenerate ground states corresponds to different light field intensity distributions among the three cavities, which conserve the overall intensity present in the system. We found signatures of the $SO(3)$ symmetry breaking in the excitation spectrum, with the appearance of two Goldstone modes at the critical point, associated with the two possible excitations along the angular directions of the ground state manifold. We also studied the self-organization of the atoms, which resulted in a hexagonal lattice, whose precise periodicity depends on the specific realization of the symmetry breaking that occurs at the phase transition.

In conclusion, our results demonstrate that rich phenomena emerge from multi-mode light-matter interacting systems. This is interesting from the perspective of quantum simulation, where efforts are being made towards the study of many-body systems with increasingly higher complexity [24, 25, 82]. Further interesting avenues include accounting for inter-cavity interactions, where coupling between order parameters allow to control the position of the phase boundaries [30], and considering the out-of-equilibrium nature of the system, e.g. the effects of quantum noise due to measurement back-action on the system dynamics [41, 43, 83], or the effects of photon losses on the steady state phase diagram [42, 44, 84].

Appendix

3.A Derivation of effective Hamiltonian (3.1)

Here we provide a derivation of the effective model (3.1), in analogy with the steps followed in Chapter 1 to derive the effective low-energy Hamiltonian (1.12). In contrast, here we need to account for the multiple cavity modes when introducing the electric field, and special care is needed when treating the alignment of the polarizations.

The setup consists of a gas of ultracold two-level atoms forming a BEC, located at the intersection point of three high-finesse Fabry-Pérot cavities, lying in the x-z plane, symmetrically aligned from each other and transversely pumped in the y direction by a circularly polarized laser (see Fig. 3.1). We start by considering the single-particle Hamiltonian of a two-level atom interacting with the cavity modes and the external pump. In the rotating frame of the pump, the interaction Hamiltonian reads

$$\hat{H}_{\text{int}} = -\hat{\vec{d}}^{\dagger} \cdot \hat{\vec{E}} - \hat{\vec{E}}^{\dagger} \cdot \hat{\vec{d}}, \tag{3.17}$$

within the rotating-wave and dipole approximations. The dipole operator is defined as $\hat{\vec{d}} = \vec{d}\hat{\sigma}_- e^{-i\omega_p t}$, with matrix element $\vec{d} = \langle g|\hat{\vec{x}}|e\rangle$, where $\hat{\vec{x}}$ is the position of the atom, $\hat{\sigma}_- = |g\rangle\langle e|$ is the lowering operator, and $|g\rangle$ and $|e\rangle$ are the ground and excited states of the atom, respectively. The electric field follows from the linear combination of the three cavity fields and the external pump, yielding

$$\hat{\vec{E}} = \sum_{l=1}^{3} E_l \vec{\epsilon}_l g_l(\vec{x}) \hat{a}_l e^{-i\omega_p t} + \frac{E_p}{2} \vec{\epsilon}_p g_p(\vec{x}) e^{-i\omega_p t}, \tag{3.18}$$

where ω_p is the pump frequency and $E_{l,p}$ and $\vec{\epsilon}_{l,p}$ are the field amplitudes and polarization vectors for cavity l and the pump, respectively. The mode functions for the cavities and the pump are $g_l(\vec{x}) \propto \cos(\vec{k}_c^{(l)}\vec{x})$ and $g_p(\vec{x}) \propto \cos(\vec{k}_p\vec{x})$, with wave-vectors $\vec{k}_c^{(l)}$ and $\vec{k}_p$ defined as in the main text. In the dispersive regime, where the driving is far detuned from the resonance frequency of the atom, the excited state can be eliminated using

perturbation theory. This results in the dipole operator being proportional to the electric field $\hat{\vec{d}} = -\alpha_s \hat{\vec{E}}$ [85], where $\alpha_s \propto \Delta_{\text{at}}^{-1}$ is the scalar polarizability of the atoms, with $\Delta_{\text{at}} = \omega_{\text{at}} - \omega_p$ the atom-pump detuning and ω_{at} the energy splitting of the two-level atoms. This leads to

$$\hat{H}_{\text{int}} = \sum_{l,l'=1}^{3} \alpha_s E_l E_{l'} g_l(\vec{x}) g_{l'}(\vec{x}) (\vec{\epsilon}_l \cdot \vec{\epsilon}_{l'}^*) \hat{a}_{l'}^\dagger \hat{a}_l + \sum_{l=1}^{3} \frac{\alpha_s E_l E_p}{2} g_l(\vec{x}) g_p(\vec{x}) \left[(\vec{\epsilon}_l \cdot \vec{\epsilon}_p^*) \hat{a}_l + \text{h.c.} \right] + \frac{\alpha_s E_p^2}{4} g_p(\vec{x})^2 |\vec{\epsilon}_p|^2. \tag{3.19}$$

In general, the atomic polarization also has vectorial and tensorial components. We take the atoms to be ^{87}Rb with $F = 1$ as the maximum eigenvalue of the total angular momentum in the ground-state manifold. The contribution from the vectorial component vanishes if we consider the case $m_F = 0$ [85], with $m_F = -F, \ldots, F$ the spin quantum number along the quantized axis. Furthermore, the tensorial component can be neglected in the typical frequency range used in these experiments [32]. We can thus simplify the Hamiltonian (3.19) to obtain

$$\hat{H}_{\text{int}} = U_p g_p(\vec{x})^2 + \sum_{l=1}^{3} U_l g_l(\vec{x})^2 \hat{a}_l^\dagger \hat{a}_l + \sum_{l=1}^{3} \eta_l g_l(\vec{x}) g_p(\vec{x}) \left(\xi_l \hat{a}_l + \xi_l^* \hat{a}_l^\dagger \right), \tag{3.20}$$

where we introduced the potential depths $U_p = \frac{\alpha_s E_p^2}{4}$ and $U_l = \alpha_s E_l^2$, the two-photon Rabi frequencies $\eta_l = \frac{\alpha_s E_l E_p}{2}$, the parameters $\xi_l = \vec{\epsilon}_l \cdot \vec{\epsilon}_p^*$, and used the definition $|\vec{\epsilon}_{l,p}|^2 = 1$. We have neglected inter-cavity interactions, which is justified in the limit $E_p \gg E_l$. This results in a many-body Hamiltonian of the form ($\hbar = 1$)

$$\hat{H} = \sum_{l=1}^{3} (-\Delta_l) \hat{a}_l^\dagger \hat{a}_l + \int d\vec{x}\ \hat{\Psi}^\dagger(\vec{x}) \Bigg\{ \frac{\hat{p}_x^2 + \hat{p}_y^2}{2m} + \sum_{l=1}^{3} \Bigg[\eta_l \left(\xi_l \hat{a}_l + \xi_l^* \hat{a}_l^\dagger \right) \cos(\vec{k}_p \vec{x}) \cos(\vec{k}_c^{(l)} \vec{x}) + U_l \cos^2(\vec{k}_c^{(i)} \vec{x}) \hat{a}_l^\dagger \hat{a}_l \Bigg] + U_p \cos^2(\vec{k}_p \vec{x}) \Bigg\} \hat{\Psi}(\vec{x}), \tag{3.21}$$

where Δ_l is the cavity-pump detuning as defined in the main text, $\hat{\Psi}(\vec{x})$ is the bosonic annihilation operator for the atomic field, $\hat{p}_{x,y}$ are the momentum operators, and m is the mass of the atoms. The first term inside the curly brackets corresponds to the kinetic energy of the atoms. The second term is associated with light-matter interactions, where the absorption or emission of photons mediates transitions of the atoms between the BEC

momentum state $|\vec{k}_0\rangle$ and twelve different momentum states $|\vec{k}^{(i)} = \pm(\vec{k}_p \pm \vec{k}_c^{(i)})\rangle$. We focus on the case where $|\vec{k}_c^{(i)}| = |\vec{k}_p| = k$, which leads to the energies of the excited momentum states becoming degenerate $\omega = 2\omega_{\text{rec}}$, with $\omega_{\text{rec}} = k^2/2m$ the recoil energy of the atoms. The third term is a dispersive shift of the cavity frequency due to the presence of the atoms and the last term corresponds to the periodic potential for the atoms generated by the pump. For simplicity, we have neglected the effects of short-ranged interactions. We now consider the low-energy physics of the system and use the ansatz

$$\hat{\Psi}(\vec{x}) = \frac{1}{\sqrt{V}}\hat{b}_0 + \sum_{l=1}^{3}\frac{2}{\sqrt{V}}\cos\left(\vec{k}_p\vec{x}\right)\cos\left(\vec{k}_c^{(l)}\vec{x}\right)\hat{b}_l, \tag{3.22}$$

where V is the volume of the system, and $\hat{b}_{0,l}$ are the bosonic annihilation operators of the momentum states defined in the main text. Inserting this ansatz into Eq. (3.21), we obtain the effective Hamiltonian

$$\hat{H} = \sum_{l=1}^{3}(-\Delta_l)\hat{a}_l^\dagger\hat{a}_l + \omega\hat{b}_l^\dagger\hat{b}_l + \frac{\lambda_l}{\sqrt{N}}\left(\xi_l\hat{a}_l + \xi_l^*\hat{a}_l^\dagger\right)\left(\hat{b}_l^\dagger\hat{b}_0 + \hat{b}_0^\dagger\hat{b}_l\right), \tag{3.23}$$

where we absorbed the dispersive shift of the cavity in the definition of the detuning and we introduced the light-matter couplings $\lambda_l = \eta_l\sqrt{N}/2$. We define the cavity fields to be linearly polarized in the x-z plane, with $\vec{\epsilon}_1 = \hat{e}_z$, $\vec{\epsilon}_2 = -\frac{\sqrt{3}}{2}\hat{e}_x + \frac{1}{2}\hat{e}_z$ and $\vec{\epsilon}_3 = \frac{\sqrt{3}}{2}\hat{e}_x + \frac{1}{2}\hat{e}_z$. To ensure the possibility of realizing symmetrical coupling between the cavities we choose the pump to be circularly polarized $\vec{\epsilon}_p = e^{-i\frac{\pi}{2}}\hat{e}_x + \hat{e}_z$, leading to $(\xi_1, \xi_2, \xi_3) = (1, e^{i\frac{\pi}{3}}, e^{-i\frac{\pi}{3}})$. These factors can then be removed by performing a set of unitary transformations of the form $\hat{a}_l \to \hat{a}_l/\xi_l$, which yields the effective Hamiltonian presented in Eq. (3.1).

3.B Calculation of the energy spectrum

We obtain the energy spectrum of the Hamiltonian (3.1) following the approach used in Refs. [39, 78]. First, we displace the operators by their expectation values $\hat{a}_i \to \hat{c}_i + \alpha_i$, $\hat{b}_i \to \hat{d}_i - \beta_i$. Considering the thermodynamic limit $N \to \infty$, we expand the Hamiltonian up to order $\mathcal{O}(1)$, exploiting the fact that $(\alpha_i, \beta_i) \propto \sqrt{N}$, where the leading order term corresponds to the mean-field energy E_{MF} defined in Eq. (3.5). Imposing the terms linear in $(\hat{c}_i, \hat{d}_i)$ to be vanishing leads to the mean-field solutions obtained in Sec. 3.4. We are

thus left with a bilinear Hamiltonian

$$\begin{aligned}\hat{H}_{\text{bil}} = &\sum_{i=1}^{3}\Bigg\{(-\Delta)\hat{c}_i^\dagger\hat{c}_i + \left[\omega + \left(\sum_j \frac{2\lambda_j}{\sqrt{kN}}\alpha_j\beta_j\right)\right]\hat{d}_i^\dagger\hat{d}_i \\ &+ \frac{\lambda_i}{\sqrt{kN}}\sum_{j=1}^{3}\alpha_i\beta_j\left(\hat{d}_i^\dagger\hat{d}_j^\dagger + \hat{d}_i^\dagger\hat{d}_j + \hat{d}_j^\dagger\hat{d}_i + \hat{d}_j\hat{d}_i\right) \\ &+ \frac{\lambda_i}{2k\sqrt{kN}}\sum_{j,l=1}^{3}\alpha_i\beta_i\beta_j\beta_l\left(\hat{d}_j^\dagger + \hat{d}_j\right)\left(\hat{d}_l^\dagger + \hat{d}_l\right) \\ &+ \lambda_i\left(\hat{c}_i^\dagger + \hat{c}_i\right)\sum_{j=1}^{3}\left(\delta_{ij}\sqrt{\frac{k}{N}} - \frac{\beta_i\beta_j}{\sqrt{kN}}\right)\left(\hat{d}_j^\dagger + \hat{d}_j\right)\Bigg\},\end{aligned} \tag{3.24}$$

where $k = N - \sum_i \beta_i$. Inserting the different solutions for α_i and β_i described in Sec. 3.4 yields the Hamiltonian in each different phase. Given the bilinear nature of (3.24), the normal modes and energy spectrum of the system in each phase are straightforwardly obtained by performing a Bogoliubov transformation.

4

Dissipation-induced instabilities of a spinor Bose-Einstein condensate inside an optical cavity

4.1 Introduction

In the previous chapter we explored the possibility of using atom-cavity systems for the quantum simulation of certain classes of Hamiltonians and their ground-state phase diagrams. Additionally, as it was explained in Chapter 1, quantum gases in optical cavities also form an ideal set-up for the study of quantum many-body systems far from equilibrium. Their large cooperativity allows reaching the strong light-matter coupling regime [86, 87] and cavity photon losses enable in-situ monitoring of the many-body dynamics in real time [88, 89]. In Chapter 1, we discussed out-of-equilibrium dynamics in the context of the open Dicke model [23, 53], where the experimental realization provided access to the observation of critical phenomena [50] and driven-dissipative dynamics [51]. Further advances have led to the study of competition between short- and long-ranged interactions out of equilibrium using optical lattices [27, 55], and the observation of complex many-body phenomena in multi-mode cavities [24, 25, 82].

Recently, considerable progress has been made, both theoretically [90, 91] and experimentally [31, 32, 92–94], on the coupling of multiple internal atomic states to the cavity modes, given its potential for quantum simulation of magnetism [91] and for quantum-enhanced metrology [93, 94]. The focus of these studies has been however on the coherent effects of the coupling, leaving the impact of dissipative processes largely unexplored. Dissipation can have noticeable effects on the properties of many-body systems, such as

modifying the nature of phase transitions [63, 64], the form of the phase diagram [45, 84], their dynamical evolution [1, 95–97], or giving rise to topological effects [98]. Therefore, it is exciting to explore the impact of dissipation on these complex systems.

In this chapter, we investigate the driven-dissipative dynamics of a spinor BEC composed of two hyperfine states coupled to a single mode of an optical cavity, as experimentally realized in Ref. [32], see Fig. 4.1. This can be captured by an open two-component Dicke model with complex light-matter couplings, as shown in Sec. 4.2. In Sec. 4.3, we obtain the steady-state phase diagram using a semi-classical approximation of the equations of motion and studying the stability of the fixed points. We uncover the emergence of a novel unstable region that, as we show, is induced by the photon losses. Our results are to be seen in contrast to previous studies where this type of dissipation leads to only minor quantitative effects [40–44, 49]. As we saw in Sec. 1.3.2, photon losses in the Dicke model shifted the position of the critical point but had no impact in the resulting phase diagram. By adiabatically eliminating the cavity field, we find that the interplay between dissipation and complex coupling results in level attraction between eigenfrequencies and the appearance of anti-damping, with the emergence of instabilities being heralded by the presence of exceptional points in the spectrum. In the unstable region, the anti-damping prevents the system from approaching a stable steady-state fixed point and leads to limit-cycle oscillations in the long-time limit. We trace this complex phenomena back to dissipative processes of the cavity field mediating non-reciprocal interactions between the spins. In Sec. 4.4, we go beyond adiabatic elimination and find that cavity fluctuations generate an additional anti-damping contribution that renders the normal phase unstable. Nevertheless, we show that this contribution remains negligible for typical parameters in the current generation of experiments [31, 32], allowing for observation of the aforementioned phenomena. We conclude in Sec. 4.5.

4.2 Model

We consider a gas of ultracold spin-1 atoms forming a BEC inside an optical cavity, see Fig. 4.1. The atoms are coupled to a single cavity mode via a linearly-polarized laser that pumps the system transversely. The atoms mediate two-photon scattering processes between the cavity and the pump which lead to transitions between the BEC state $|k_0\rangle$ and the excited states $|\vec{k}_{\pm,\pm}\rangle = |\pm(\vec{k}_c \pm \vec{k}_p)\rangle$, where $\vec{k}_{c,p}$ are cavity and pump momenta, respectively. We fix $|\vec{k}_c| = |\vec{k}_p| = k$ and, in this case, all the states $|\vec{k}_{\pm,\pm}\rangle$ are degenerate, thus for each atom i the transitions take place between $|k_0\rangle^i$ and the symmetric state $|k\rangle^i = \frac{1}{2}\sum_{\mu,\nu=\pm} |\vec{k}_{\mu,\nu}\rangle^i$ [23]. This allows for a description of the system in

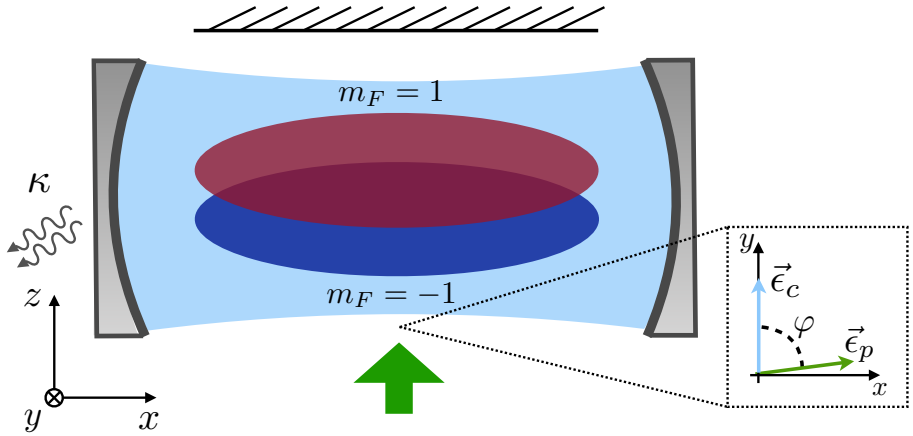

Figure 4.1: Spinor Bose-Einstein condensate composed of two hyperfine states $m_F = \pm 1$, coupled to a single-mode optical cavity with photon loss rate κ and transversely driven by a laser whose polarization vector $\vec{\epsilon}_p$ is at an angle φ with respect to the cavity field polarization vector $\vec{\epsilon}_c$. This leads to a finite contribution from the vectorial polarizability of the atoms, resulting in complex light-matter couplings, of equal strength but opposite phase, between the hyperfine states and the cavity field [32].

terms of collective spin operators, which, in the rotating frame of the pump, reads[1] [32]

$$\hat{H} = -\Delta \hat{a}^\dagger \hat{a} + \sum_{m_F} \omega_0 \hat{J}_{z,m_F} + \frac{\hat{J}_{x,m_F}}{\sqrt{N_{m_F}}} (\lambda^*_{m_F} \hat{a} + \lambda_{m_F} \hat{a}^\dagger), \tag{4.1}$$

where $\hat{a}$ is the bosonic annihilation operator for the cavity field, $\Delta = \omega_p - \omega_c$ is the detuning between the cavity ω_c and the pump ω_p frequency. The operator $\hat{J}_{\alpha,m_F} = \sum_i \hat{\sigma}^i_{\alpha,m_F}$ is a collective spin operator, where $\hat{\sigma}_{z,m_F} = |k\rangle^{ii}\langle k| - |k_0\rangle^{ii}\langle k_0|$ and $\hat{\sigma}^i_{x,m_F} = \frac{1}{2}(|k_0\rangle^{ii}\langle k| + \text{H.c.})$. The level splitting ω_0 equals twice the recoil frequency $\omega_r = k^2/2m$, and N_{m_F} is the number of atoms in spin state m_F. The third term in (4.1) describes the scattering of a pump photon into the cavity mode which is accompanied by an atomic transition. Misalignment between pump and cavity polarizations induces a non-vanishing vectorial component in the atomic polarizability, so the spin states couple differently to the cavity [32]. The complex light-matter couplings $\lambda_{m_F} = |\lambda_{m_F}| e^{i\phi_{m_F}}$ have modulus $|\lambda_{m_F}| = \sqrt{\lambda_s^2 \cos^2\varphi + \lambda_v^2 m_F^2 \sin^2\varphi}$, where $\lambda_{s,v}$ is proportional to the scalar and vectorial atomic polarizabilities and φ the angle between the pump and cavity polarization vectors $\vec{\epsilon}_p$ and $\vec{\epsilon}_c$, and $\tan\phi_{m_F} = \frac{\lambda_v m_F}{\lambda_s} \tan\varphi$ [32].

For the remainder of this chapter, we will focus on the case $N_{\pm 1} = N$, $|\lambda_{\pm 1}| = \lambda$ and $\phi_1 = -\phi_{-1} = \phi$. We obtain a two-component variant of the Dicke model [34, 37, 38]. We stress that, for the Hamiltonian (4.1), the two effective atomic spins cannot be

[1] Note that there is a factor of 2 difference between the defintion of λ here and in Eq. (1.13). This choice was made in order to make a straightforward comparison with the results in [32, 33] .

encapsulated in a single collective spin due to the phase difference between the couplings and that the phase difference ϕ cannot be removed from the Hamiltonian by any gauge transformation. Indeed, we find that it is one of the key ingredients for the effects we discuss below.

The Hamiltonian (4.1) possesses a $\mathbb{Z}_2$ symmetry, associated with invariance under the transformation $\hat{\mathcal{U}} = e^{i\pi\hat{\mathcal{N}}}$, with $\hat{\mathcal{N}} = \hat{a}^\dagger\hat{a} + \sum_{\sigma=\pm1} \hat{J}_{z,\sigma}$, which can be understood as parity conservation of the total number of excitations in the system. For $\phi = 0$, spontaneous breaking of this symmetry results in the well-known superradiant phase transition of the Dicke model [34, 37, 38], where the global spins acquire a finite and equal x-component. For the atom-cavity system, this corresponds to a transition from the BEC state with no photons inside the cavity, corresponding to the normal phase (NP), into a self-organized, density-wave state (DW), accompanied by the emergence of a macroscopic cavity field [41–44, 49]. It has been shown in Ref. [32] that for $\phi \neq 0$, the spontaneous breaking of the $\mathbb{Z}_2$ symmetry can lead to a different kind of superradiant order where the x-component of the collective spins anti-align, corresponding to each cloud of atoms self-organizing in opposite checkerboard patterns, i.e. formation of a spin wave (SW). In Fig. 4.2(a) we show the phase diagram obtained within mean-field theory (see Appendix 4.A), in agreement with the observations reported in [32], where the NP-DW as well as the NP-SW boundaries are given by $\lambda_{\rm cr}^{d/s} = \sqrt{\frac{(-\Delta)\omega_0}{1\pm\cos(2\phi)}}$ and the DW-SW boundary is located at $\phi = \pi/4$. In the following, we study how this phase diagram is modified when taking into account the dissipative nature of the cavity.

4.3 Steady-state phase diagram

We start by including dissipation in our model via a Lindblad master equation of the form $\partial_t\hat{\rho} = (-i)[\hat{H},\hat{\rho}] + \kappa(\hat{a}\hat{\rho}\hat{a}^\dagger - \frac{1}{2}\hat{a}^\dagger\hat{a}\hat{\rho} - \frac{1}{2}\hat{\rho}\hat{a}^\dagger\hat{a})$, where κ is the photon loss rate. In analogy with Sec. 1.3.2, we perform a semi-classical approximation and obtain a set of equations of motion for the cavity field and the collective spins, which after factorizing high-order correlations read

$$\begin{aligned}
\partial_t\alpha &= \left(i\Delta - \frac{\kappa}{2}\right)\alpha - i\frac{\lambda}{\sqrt{N}}\left(S_{x,1}e^{i\phi} + S_{x,-1}e^{-i\phi}\right),\\
\partial_t S_{x,\pm1} &= -\omega_0 S_{y,\pm1},\\
\partial_t S_{y,\pm1} &= \omega_0 S_{x,\pm1} - \frac{\lambda}{\sqrt{N}}\left(\alpha e^{\mp i\phi} + \alpha^* e^{\pm i\phi}\right) S_{z,\pm1},\\
\partial_t S_{z,\pm1} &= \frac{\lambda}{\sqrt{N}}\left(\alpha e^{\mp i\phi} + \alpha^* e^{\pm i\phi}\right) S_{y,\pm1},
\end{aligned} \tag{4.2}$$

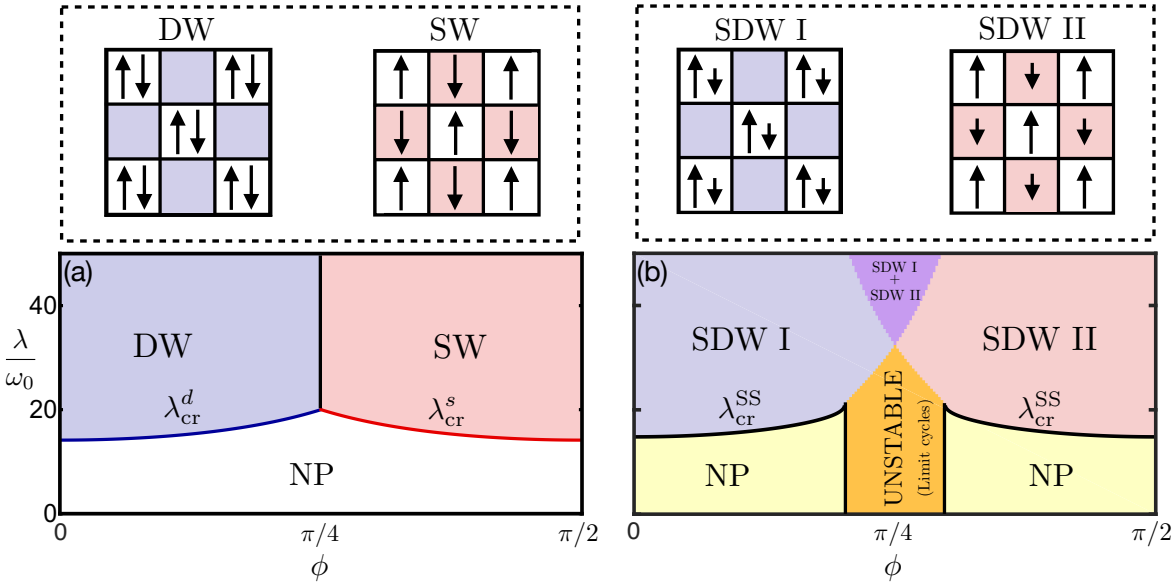

Figure 4.2: (a) Ground-state and (b) steady-state phase diagrams as a function of the light-matter coupling λ and phase ϕ, for $\Delta = -400\omega_0$ and $\kappa = 250\omega_0$. Going beyond adiabatic elimination and including the cavity field fluctuations renders the NP unstable (light orange shading) for $\phi \neq 0, \pm\frac{\pi}{2}$. Above the phase diagrams we show schematic depictions of the lattice configurations of the atoms in each phase. For the DW and SW phases, the spins occupy the same and opposite checkerboard patterns, respectively. In the SDW I and II phases, density and spin imbalance coexist, denoted by the difference in arrow lengths, with one being strongly dominant over the other in each phase.

with $\alpha = \langle \hat{a} \rangle$ and $S_{\sigma,\pm1} = \langle \hat{J}_{\sigma,\pm1} \rangle$. We first focus on the bad-cavity limit, $(|\Delta|, \kappa) \gg (\omega_0, \lambda)$, as studied experimentally in Refs. [31, 32]. In this limit, the cavity evolves much faster than the atoms, allowing us to adiabatically eliminate it by considering α to be in the steady state $\alpha \approx \frac{\lambda}{\sqrt{N}} \frac{S_{x,1}e^{i\phi} + S_{x,-1}e^{-i\phi}}{\Delta + i\frac{\kappa}{2}}$. By setting $\partial_t S_{\sigma,\pm1} = 0$, we obtain a set of algebraic equations for the steady-state solutions

$$S_{x,\pm1} + \frac{2\lambda^2}{N(\Delta^2 + \frac{\kappa^2}{4})} \left\{ \Delta S_{x,\pm1} + \left[\Delta \cos(2\phi) \mp \frac{\kappa}{2} \sin(2\phi) \right] S_{x,\mp1} \right\} \sqrt{\frac{N^2}{4} - S^2_{x,\pm1}} = 0, \tag{4.3}$$

where we used $S_{y,\pm1} = 0$ and $S_{z,\pm1} = -\sqrt{\frac{N^2}{4} - S^2_{x,\pm1}}$. These equations do not admit a closed analytical solution, except for the trivial solution $S_{x,\pm1} = 0$, associated with the NP. Hence, the steady-state values for $S_{x,\pm1}$ need to be obtained numerically. To construct the phase diagram, we determine the stability of these solutions by linearizing the equations

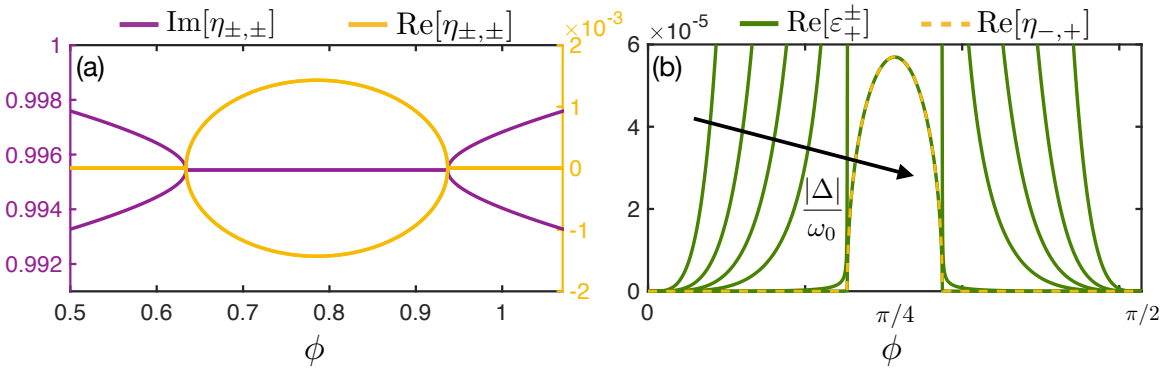

Figure 4.3: (a) The imaginary and real part of the eigenvalues $\eta_{\pm,\pm}$ of the dynamical matrix (4.4), resulting from adiabatic elimination of the cavity field, for $\lambda = 2\omega_0$, $\Delta = -400\omega_0$ and $\kappa = 250\omega_0$. We observe level attraction in the spectrum, consequence of the emergence of exceptional points. (b) The real part of the pair of eigenvalues $\varepsilon_+^{\pm}$ (solid lines) responsible for anti-damping in the NP, obtained from the full dynamical matrix including cavity field fluctuations in Eq. (4.9), for $\Delta/\omega_0 = 10, 25, 50, 400, 1000, 10000$, $\kappa = 0.625|\Delta|$ and $\lambda = 2\omega_0$. As the bad-cavity limit is approached, the eigenvalues reduce to $\eta_{-,+}$ (dashed lines) given by (4.7). All quantities are in units of ω_0.

of motion around the steady state $\hat{J}_{\sigma,\pm1}(t) \simeq S_{\sigma,\pm1} + \delta\hat{J}_{\sigma,\pm1}(t)$

$$\partial_t \begin{pmatrix} \delta\hat{J}_{x,1} \\ \delta\hat{J}_{y,1} \\ \delta\hat{J}_{x,-1} \\ \delta\hat{J}_{y,-1} \end{pmatrix} = \begin{pmatrix} 0 & -\omega_0 & 0 & 0 \\ \omega_0 + \xi_+ & 0 & \chi_+ & 0 \\ 0 & 0 & 0 & -\omega_0 \\ \chi_- & 0 & \omega_0 + \xi_- & 0 \end{pmatrix} \begin{pmatrix} \delta\hat{J}_{x,1} \\ \delta\hat{J}_{y,1} \\ \delta\hat{J}_{x,-1} \\ \delta\hat{J}_{y,-1} \end{pmatrix}. \tag{4.4}$$

We observe that the effects of the eliminated cavity field are that of introducing a frequency splitting

$$\xi_\pm = \frac{2\lambda^2 S_{z,\pm1}}{N(\Delta^2 + \frac{\kappa^2}{4})} \left\{ \Delta \left(\frac{S_{x,\pm1}^2}{S_{z,\pm1}^2} - 1 \right) + \left[\Delta\cos(2\phi)) \mp \frac{\kappa}{2}\sin(2\phi) \right] \frac{S_{x,1}S_{x,-1}}{S_{z,\pm1}^2} \right\} \tag{4.5}$$

between the spin components, and inducing effective interactions between the spins

$$\chi_\pm = -\frac{2\lambda^2 S_{z,\pm1}}{N(\Delta^2 + \frac{\kappa^2}{4})} \left[\Delta\cos(2\phi) \mp \frac{\kappa}{2}\sin(2\phi) \right]. \tag{4.6}$$

with both $\xi_\pm$ and $\chi_\pm$ functions of the external and order parameters. Note that the latter are in general different $\chi_+ \neq \chi_-$, resulting in a non-reciprocal coupling. This means that each spin responds differently to the motion of the other one, which turns out to have a strong impact on the driven-dissipative dynamics of the system. The resulting phase diagram is shown in Fig. 4.2(b), where we identify five different phases, classified by the

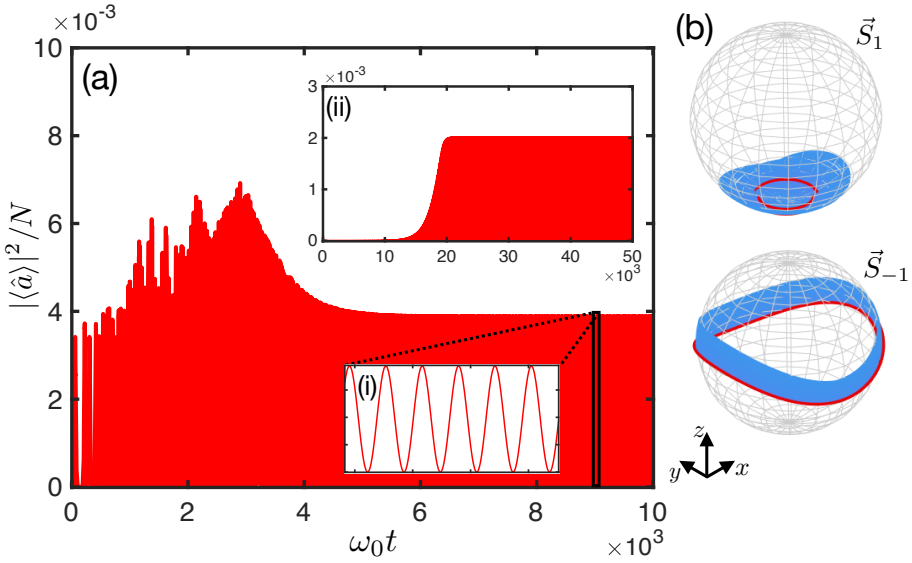

Figure 4.4: Dynamics in the unstable regime, with $\Delta = -40\omega_0$, $\kappa = 25\omega_0$, $\lambda = 5\omega_0$ and $\phi = \pi/4$. (a) Time evolution of the average photon number, displaying limit-cycle oscillations in the long-time limit. (b) Bloch spheres depicting the long-time dynamics (blue) of the collective spins preceding the start of the steady-state limit cycle (thick red line). Insets: (i) Magnified picture of the limit-cycle oscillations; (ii) Time evolution for $\phi = 0.4$, corresponding to the NP within adiabatic elimination, but unstable when including the cavity field dynamics.

order parameters $S_{x,\pm 1}$ and the number of stable solutions, which we will now describe in turn.

The most striking difference with the ground-state phase diagram is the emergence of an unstable region inside the NP. To understand this, we look at the spectrum of the dynamical matrix in Eq. (4.4), which in the NP reads

$$\eta_{\pm,\pm} = \pm i\sqrt{\omega_0(\omega_0 + \xi) \pm \omega_0\sqrt{\chi_+\chi_-}}, \tag{4.7}$$

where $\xi = \xi_\pm = \Omega\Delta$ and $\chi_\pm = \Omega[\Delta\cos(2\phi) \mp \frac{\kappa}{2}\sin(2\phi)]$, with $\Omega = \lambda^2/(\Delta^2 + \frac{\kappa^2}{4})$. From this expression, we see that when the couplings $\chi_\pm$ acquire opposite sign, $\tan^2(2\phi) > 4\Delta^2/\kappa^2$, the imaginary parts (frequencies) coalesce, while the real parts (decay rates) become finite, resulting in the emergence of decay and anti-damping, see Fig. 4.3(a). This phenomenon is known as level attraction and can only arise in non-Hermitian matrices, such as the dynamical matrix in Eq. (4.4) [99]. This is signaled by the presence of exceptional points, where the eigenvalues are degenerate and the eigenvectors coalesce. In our case, this corresponds to $\tan^2(2\phi) = 4\Delta^2/\kappa^2$, where we have $\chi_\pm = 0$. The emergent anti-damping is what makes the NP unstable. This can be observed in Fig. 4.4, where we show the time-evolution of the cavity field, from the semi-classical equations of motion (4.2). Initializing

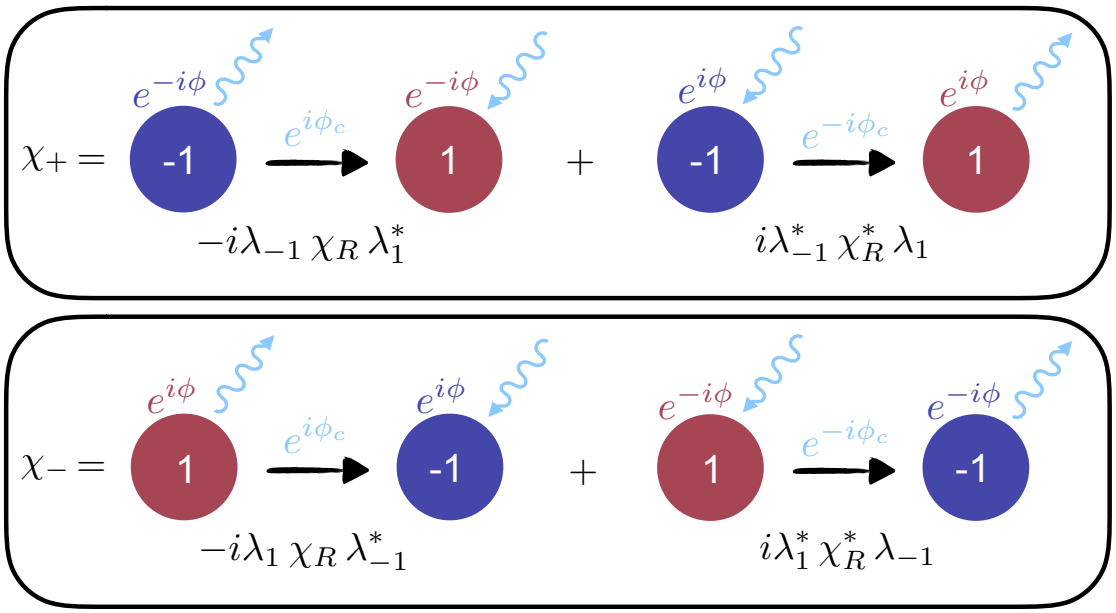

Figure 4.5: Schematic representation of the non-reciprocal coupling as the interference of light-matter scattering pathways. Red (Blue) circles denote the collective spin $\vec{S}_1$ ($\vec{S}_{-1}$). The light blue arrows denote the interaction with an incoming or outgoing photon. The phases are given by the light-matter coupling $\lambda_\pm = \lambda e^{\pm i\phi}$, and the cavity phase shift follows from the cavity response function $\chi_R = |\chi_R| e^{i\phi_c}$, with $\phi_c = \tan(-2\Delta/\kappa)$. Non-reciprocity emerges from the phase shift generated by the cavity is not modified when swapping the spins. This means that the cavity distinguishes the two type of scattering processes (the terms in the left vs. the terms in the right), but not which spin the photons are scattered from (left and right terms get the same phase shift respectively).

the system in the NP with small fluctuations in the cavity field, we see how the system does not remain in this phase, but becomes unstable and at long times features a limit cycle [2]. Excitingly, this phenomenon has recently been observed experimentally, with periodic oscillations in the phase and photon number of the light field leaking out of the cavity [33].

We trace the origin of the unstable behavior to the cavity field mediating non-reciprocal interactions between the atoms. The form of the couplings follows from the equations of motion of the cavity field in the NP, yielding

$$\chi_\pm = -\frac{i}{2}\lambda_{\mp 1}\chi_R\lambda_{\pm 1}^* + \frac{i}{2}\lambda_{\mp 1}^*\chi_R^*\lambda_{\pm 1}, \tag{4.8}$$

with $\chi_R = (-i\Delta + \kappa/2)^{-1}$ the cavity response function in the bad-cavity limit. Each term represents an amplitude for a photon scattering process from one spin to another, with

[2] We have used parameters different from those in the recent experiment [32] for the phase diagram in Fig. 4.2(b), so that clean self-sustained oscillations are established within the integration times available through numerical integration.

$\chi_\pm$ being the total scattering amplitude for each pathway. For $\kappa = 0$, the total scattering amplitudes are symmetric under the exchange of spins ($\chi_+ = \chi_-$). Conversely, for finite κ, the phase shift induced by the cavity response results in the interference between the scattering amplitudes being different for each pathway, leading to a non-reciprocal coupling, see Fig. 4.5. Thus, we can conclude that emergence of the dynamical instability is a consequence of the dissipative nature of the cavity field. Note that, nevertheless, the phase difference between $\lambda_{\pm 1}$ is a crucial ingredient, as for $\phi = 0$ both pathways are equivalent, independently of the value of κ. This constitutes one of the major findings of this work, which should be contrasted with the impact of photon loss in the standard Dicke model. There, these processes lead to a shift of the critical point [40, 42–44, 49] and a change in the critical exponent [43], but the ground-state and steady-state phase diagrams are qualitatively similar.

For $\lambda > \lambda_{\rm cr}^{\rm SS} = \sqrt{\frac{(-\omega_0)(\Delta^2+\kappa^2/4)}{\Delta\pm\sqrt{\Delta^2\cos^2(2\phi)-(\kappa^2/4)\sin^2(2\phi)}}}$, the system becomes unstable favoring two different steady-state superradiant phases, which we denote as SDW I and SDW II. These are different from the DW and SW phases in Fig. 4.2(a) as the effects of dissipation in the steady-state equations lead to $|S_{x,1}| \neq |S_{x,-1}|$, resulting in simultaneous presence of density- and spin-wave order. The SDW I phase is a reminiscent of the DW phase with two of solutions corresponding to the spins being almost aligned, and the SDW II phase is instead reminiscent of the SW phase, with a pair of solutions associated with the spins being almost anti-aligned. This schematically shown in Fig. 4.2. Finally, we identify a fifth phase at large coupling λ, where both SDW I and II are steady states of the system.

4.4 Beyond adiabatic elimination

Finally, we go beyond adiabatic elimination and include the fluctuations of the cavity field. The steady-state equations for the cavity field α and spins $S_{x,\pm 1}$ remain unchanged. In the linear stability analysis we now have to include the dynamics of the cavity-field fluctuations $\delta\hat{a}$ and $\delta\hat{a}^\dagger$, leading to a dynamical matrix of the form

$$\partial_t \begin{pmatrix} \delta\hat{a} \\ \delta\hat{a}^\dagger \\ \delta\hat{J}_{x,1} \\ \delta\hat{J}_{y,1} \\ \delta\hat{J}_{x,-1} \\ \delta\hat{J}_{y,-1} \end{pmatrix} = \begin{pmatrix} i\Delta - \frac{\kappa}{2} & 0 & -i\frac{\lambda}{\sqrt{N}}e^{i\phi} & 0 & -i\frac{\lambda}{\sqrt{N}}e^{-i\phi} & 0 \\ -i\Delta - \frac{\kappa}{2} & 0 & i\frac{\lambda}{\sqrt{N}}e^{-i\phi} & 0 & i\frac{\lambda}{\sqrt{N}}e^{i\phi} & 0 \\ 0 & 0 & 0 & -\omega_0 & 0 & 0 \\ -\frac{\lambda}{\sqrt{N}}S_{z,1}e^{-i\phi} & -\frac{\lambda}{\sqrt{N}}S_{z,1}e^{i\phi} & \omega_0 + \Xi_+ & 0 & 0 & 0 \\ 0 & 0 & 0 & 0 & 0 & -\omega_0 \\ -\frac{\lambda}{\sqrt{N}}S_{z,-1}e^{i\phi} & -\frac{\lambda}{\sqrt{N}}S_{z,-1}e^{-i\phi} & 0 & 0 & \omega_0 + \Xi_- & 0 \end{pmatrix} \begin{pmatrix} \delta\hat{a} \\ \delta\hat{a}^\dagger \\ \delta\hat{J}_{x,1} \\ \delta\hat{J}_{y,1} \\ \delta\hat{J}_{x,-1} \\ \delta\hat{J}_{y,-1} \end{pmatrix}, \tag{4.9}$$

where $\Xi_\pm$ is related to $\xi_\pm$, as defined in Eq. (4.5), through $\Xi_\pm = \xi_\pm + \frac{2\Delta\lambda^2 S_{z,\pm 1}}{N(\Delta^2+\frac{\kappa^2}{4})}$. As opposed to the previous case, it is not possible to diagonalize this dynamical matrix analytically, even in the NP. Thus, we compute the eigenvalues numerically. We find that the resulting phase diagram is qualitatively similar to the one presented in Fig. 4.2(b), with the important exception of the NP being unstable for all $\phi \neq 0, \pm\frac{\pi}{2}$. This is due to a pair of complex conjugate eigenvalues $\varepsilon_+^\pm$ with finite real positive part. In Fig. 4.3(b), we show the real part of these eigenvalues. These are finite for all $\phi \neq 0, \pm\frac{\pi}{2}$ and they reduce to expression (4.7) in the limit $(|\Delta|, \kappa) \gg (\omega_0, \lambda)$. As a consequence, the system is driven into limit cycles all throughout the region associated with the solutions $S_{x,\pm 1} = 0$. This is shown in the inset of Fig. 4.4, where the time-evolution is considered at a point where adiabatic elimination predicts the NP to be stable, i.e. $\lambda < \lambda_{\rm cr}^{\rm SS}$ and $\tan^2(2\phi) < 4\Delta^2/\kappa^2$. We observe how the system initially remains in the NP, but at longer times, the system dynamics features limit-cycle behavior.

We investigate this further by calculating the eigenvalues perturbatively, exploiting that this phenomenon is also present at small λ. In Fourier space, the linearized equations of motion for the cavity fluctuations are

$$\chi_R^{-1}(\omega)\delta\hat{a}(\omega) = \frac{-i\lambda}{2\sqrt{N}}\sum_\sigma \left[\delta\hat{J}_\sigma^+(\omega) + \delta\hat{J}_\sigma^-(\omega)\right] e^{i\sigma\phi} - \sqrt{\kappa}\hat{a}_{\rm in}(\omega) \tag{4.10}$$

with $[\delta\hat{a}(\omega)]^\dagger = \delta\hat{a}(-\omega)^\dagger$, $\chi_R(\omega) = [-i(\Delta+\omega)+\kappa/2]^{-1}$ the cavity response function at finite frequency, $\hat{J}^\pm = \hat{J}_x \pm i\hat{J}_y$ the spin raising and lowering operators and $\hat{a}_{\rm in}$ the cavity input noise. For $\lambda = 0$, $\delta\hat{J}_{\pm 1}^+$ and $\delta\hat{J}_{\pm 1}^-$ rotate with frequencies ω_0 and $-\omega_0$, respectively. Using a rotating-wave approximation, we can consider these pairs of modes to be effectively uncoupled and focus only on the dynamics of $\delta\hat{J}_{\pm 1}^-$. Substituting Eq. (4.10) into the equation of motion for $\delta\hat{J}_{\pm 1}^-(\omega)$, we obtain

$$\begin{pmatrix} i(\omega_0-\omega)+\frac{i}{2}\Sigma(\omega_0) & \frac{i}{2}\Lambda_+(\omega_0) \\ \frac{i}{2}\Lambda_-(\omega_0) & i(\omega_0-\omega)+\frac{i}{2}\Sigma(\omega_0) \end{pmatrix} \begin{pmatrix} \delta\hat{J}_1^-(\omega) \\ \delta\hat{J}_{-1}^-(\omega) \end{pmatrix} = \vec{\Gamma}_{\rm in} \tag{4.11}$$

with

$$\Sigma(\omega) = \frac{\lambda^2}{2}[-i\chi_R(\omega) + i\chi_R^*(-\omega)], \qquad \Lambda_\pm(\omega) = \frac{\lambda^2}{2}[-i\chi_R(\omega)e^{\mp 2i\phi} + i\chi_R^*(-\omega)e^{\pm 2i\phi}], \tag{4.12}$$

the self-energy and the non-reciprocal coupling, respectively. In the sprit of Fermi's Golden Rule we have evaluated the energy-dependent self-energy and coupling at the

unperturbed frequency of the mode ω_0 [100]. We have incorporated all noise terms in

$$\vec{\Gamma}_{\text{in}} = \frac{\lambda\sqrt{\kappa N}}{2}\begin{pmatrix}\chi_R(\omega)\hat{a}_{\text{in}}(\omega)e^{-i\phi} + \chi_R^*(-\omega)\hat{a}_{\text{in}}^\dagger(\omega)e^{i\phi}\\ \chi_R(\omega)\hat{a}_{\text{in}}(\omega)e^{i\phi} + \chi_R^*(-\omega)\hat{a}_{\text{in}}^\dagger(\omega)e^{-i\phi}\end{pmatrix}. \tag{4.13}$$

The spectrum follows from the determinant of the dynamical matrix (4.11) as[3]

$$\varepsilon_\pm^- = -i\omega_0 - \frac{i}{2}\Sigma(\omega_0) \pm \frac{i}{2}\sqrt{\Lambda_+(\omega_0)\Lambda_-(\omega_0)}. \tag{4.14}$$

The self-energy $\Sigma(\omega_0)$ only provides a frequency shift and a finite damping rate, given that for $\Delta < 0$, $\text{Im}[\Sigma(\omega_0)] < 0$. On the contrary, the couplings $\Lambda_\pm(\omega_0)$ always yield an anti-damping contribution, which cannot be compensated by the self-energy damping, as they emerge in a $\pm$ pair and due to $\text{Im}[\Lambda_+(\omega_0)\Lambda_-(\omega_0)] \neq 0$ for all $\phi \neq 0, \pm\frac{\pi}{2}$ and $\kappa \neq 0$. Thus, the finite-frequency response of the cavity fluctuations is responsible for the emergence of anti-damping and for the NP becoming unstable to self-sustained oscillations. As expected, in the limit $\kappa \to 0$, we obtain $\text{Im}[\Lambda_+(\omega_0)\Lambda_-(\omega_0)] \to 0$ and $\text{Re}[\Lambda_+(\omega_0)\Lambda_-(\omega_0)] > 0$, thus restoring the stability of the NP and confirming again the dissipative nature of the instability. Interestingly, in this limit, the interaction still remains non-reciprocal $\Lambda_+(\omega_0) \neq \Lambda_-(\omega_0)$, meaning that outside the bad-cavity regime the presence of non-reciprocity does not imply unstable behavior. A second pair of eigenvalues $\varepsilon_\pm^+$ is obtained if one considers the dynamics of $\delta\hat{J}_{\pm1}^+$ instead, which together with (4.14) provides an approximate form for the eigenvalues $\varepsilon_+^\pm$ shown in Fig. 4.3(b) in the limit of small λ. The form of (4.14) also explains why in the bad-cavity limit the instability is confined to a finite region. More specifically, the bad-cavity limit is equivalent to $\omega \to 0$, corresponding to the zero-frequency response of the cavity fluctuations being the only component playing a role in the dynamics. This leads to $\Sigma(\omega) \to \xi$ and $\Lambda_+(\omega)\Lambda_-(\omega) \to \chi_+\chi_-$, i.e. the instability occurs if $\chi_+\chi_- < 0$, in agreement with our previous result.

4.5 Conclusion

In this chapter, we explored the driven-dissipative dynamics of a spinor-BEC interacting with the single mode of an optical cavity, by means of an effective two-mode Dicke model. We found that a misalignment between the polarizations of the cavity mode and the external drive resulted in complex light-matter couplings. By adiabatically eliminat-

[3]We use the Fourier transform convention $\hat{O}(t) \propto \int d\omega e^{-i\omega t}\hat{O}(\omega)$. Hence, the frequency ω is related to the spectrum of the dynamical matrix by a factor of $-i$.

ing the cavity field we obtained that photons mediate non-reciprocal interactions between the collective spins. Using a semiclassical approach, we uncovered the presence of an unstable region in the steady-state phase diagram in which the system is driven into limit cycles. Through a linear stability analysis, we showed that the presence of the unstable region is caused by the non-reciprocity in the interactions. Moreover, we found the root for non-reciprocity to be in the phase shift generated by the cavity during atom-photon scattering events. In particular, this phase shift is purely a consequence of the dissipative nature of the cavity, leading to the conclusion that the obtained instability is induced by dissipation. This constitutes a highly interesting result as it shifts the paradigm of photon losses in Dicke models, from merely shifting the position of the critical point, to have a stronger impact in the overall dynamical behavior of the model.

Our work opens exciting avenues for future investigations. First, finding an exact solution similar to [39] or efficient numerics [101] would allow one to explore the instability beyond the semi-classical approximation employed here. Second, non-reciprocity has recently been investigated with several platforms [102–105] that have been specifically engineered. Here, it emerges naturally as a consequence of the dissipative nature of the cavity field, offering a testbed for non-reciprocal phenomena in a highly-controlled environment. In particular, interesting directions include the impact of non-reciprocity on higher-order photon correlations [106] or on synchronization behavior [107]. Lastly, the effects of interatomic interactions could be investigated with an additional optical lattice and lead to complex many-body behavior [108].

Appendix

4.A Mean-field ground-state phase diagram

In this appendix we discuss the main steps taken to obtain the form of the ground-state phase diagram presented in the main text. This was first discussed in Ref. [32] and follows the same arguments as in Secs. 1.3.1 and 3.4. We start by introducing the Holstein-Primakoff transformation $\hat{J}_{z,\pm 1} = \hat{b}_{\pm}^{\dagger}\hat{b}_{\pm} - \frac{N}{2}$ and $\hat{J}_{x,\pm 1} = \frac{1}{2}\left(\hat{b}_{\pm}^{\dagger}\sqrt{N-\hat{b}_{\pm}^{\dagger}\hat{b}_{\pm}} + \sqrt{N-\hat{b}_{\pm}^{\dagger}\hat{b}_{\pm}}\,\hat{b}_{\pm}\right)$ and inserting it in the Hamiltonian (4.1) defined in the main text, which leads to (up to a constant shift)

$$\hat{H} = -\Delta\hat{a}^{\dagger}\hat{a} + \sum_{\sigma=\pm}\left[\omega_0\hat{b}_{\sigma}^{\dagger}\hat{b}_{\sigma} + \frac{\lambda}{2}\left(\hat{a}e^{-i\sigma\phi} + \hat{a}^{\dagger}e^{i\sigma\phi}\right)\left(\hat{b}_{\sigma}^{\dagger}\sqrt{N-\hat{b}_{\sigma}^{\dagger}\hat{b}_{\sigma}} + \sqrt{N-\hat{b}_{\sigma}^{\dagger}\hat{b}_{\sigma}}\,\hat{b}_{\sigma}\right)\right]. \tag{4.15}$$

We obtain the ground-state phase diagram of the Hamiltonian (4.15) by studying the mean-field energy

$$E_{\mathrm{MF}} = -\Delta|\alpha|^2 + \sum_{\sigma=\pm}\left[\omega_0|\beta_{\sigma}|^2 + \lambda(\alpha e^{-i\sigma\phi} + \alpha^* e^{i\sigma\phi})\mathrm{Re}[\beta_{\sigma}]\sqrt{1-\frac{|\beta_{\sigma}^2|}{N}}\right], \tag{4.16}$$

where $\alpha = \langle\hat{a}\rangle$ and $\beta_{\pm} = \langle\hat{b}_{\pm}\rangle$. Minimizing the energy with respect to both fields yields $\beta_{\pm} = \mathrm{Re}[\beta_{\pm}]$ and $\alpha = \frac{\lambda}{\Delta}\sum_{\sigma} e^{i\sigma\phi}\beta_{\sigma}\sqrt{1-\frac{\beta_{\sigma}^2}{N}}$. We expand the square-root terms to first order, since close to the phase transition $(\beta_{\pm}/N) \ll 1$, and introduce new order parameters $\beta_{d,s} = \frac{1}{\sqrt{2}}(\beta_{+} \pm \beta_{-})$, which signal the presence of density- and spin-wave order, respecitvely. This leads to

$$\begin{aligned} E_{\mathrm{MF}} \simeq &\left[\omega_0 + \frac{\lambda^2}{\Delta}(1+\cos(2\phi))\right]\beta_d^2 - \frac{\lambda^2}{2N\Delta}(1+\cos(2\phi))\beta_d^4 \\ &+ \left[\omega_0 + \frac{\lambda^2}{\Delta}(1-\cos(2\phi))\right]\beta_s^2 - \frac{\lambda^2}{2N\Delta}(1-\cos(2\phi))\beta_s^4. \end{aligned} \tag{4.17}$$

From the global minima of (4.17), we distinguish three different phases as function of λ and ϕ, see Fig. 4.2(a) in the main text. First, for $\lambda < (\lambda_{\mathrm{cr}}^{d}, \lambda_{\mathrm{cr}}^{s})$, being the critical

values $\lambda_{\mathrm{cr}}^{d} = \sqrt{\frac{(-\Delta)\omega_0}{1+\cos(2\phi)}}$ and $\lambda_{\mathrm{cr}}^{s} = \sqrt{\frac{(-\Delta)\omega_0}{1-\cos(2\phi)}}$, both order parameters vanish $\beta_{d,s} = 0$. This corresponds to the NP, where both collective spins point down in the z direction, meaning that all atoms remain in the BEC state. Second, for $\lambda > \lambda_{\mathrm{cr}}^{d}$ and $0 \leq \phi \leq \frac{\pi}{4}$, we obtain $\beta_d = \pm\sqrt{N(1-(\lambda_{\mathrm{cr}}^{d}/\lambda)^2)}$, while $\beta_s = 0$. This is associated with both collective spins aligning in the x-z plane, meaning that both atomic species self-organize in the same pattern, thus realizing a density-wave state (DW). Lastly, for $\lambda > \lambda_{\mathrm{cr}}^{s}$ and $\frac{\pi}{4} \leq \phi \leq \frac{\pi}{2}$, we obtain $\beta_s = \pm\sqrt{N(1-(\lambda_{\mathrm{cr}}^{s}/\lambda)^2)}$ and $\beta_d = 0$, where now the x-components of the spins point in opposite directions. This can be understood as the atomic species self-organizing in the opposite checkerboard patterns, resulting in the emergence of a spin-wave state (SW).

5

Tuning the relaxation dynamics of ultracold atoms in a lattice with an optical cavity

5.1 Introduction

Ultracold atomic gases loaded in optical lattices have proven to be an ideal playground for simulating quantum many-body physics [10–18]. The Bose-Hubbard (BH) model [109] is a paradigmatic example for which the superfluid-Mott insulator phase transition has been observed experimentally [12].

More recently, ultracold atoms in optical lattices have been coupled to the single mode of an optical cavity with the aim of exploring and simulating richer phenomena [26, 27]. The description of these systems can be based on a BH-type model whose physics is determined by the competition between kinetic energy, on-site, and infinite-range interactions. The ground-state phase diagram of this system and quench dynamics have been explored experimentally [26, 27, 55] and theoretically [54, 56–58, 110]. This has provided a detailed understanding of the coherent phenomena of the system. However, little is known about its open system dynamics. Driven-dissipative systems can exhibit notably different phase diagrams from their equilibrium counterparts [65] and the interplay of interactions and dissipation can lead to unusual relaxation dynamics [111–114].

In this chapter, we investigate the effects of dissipation in the set-up realized in Ref. [26]. The model is introduced in Sec. 5.2. For weak atom-light coupling, we derive an effective quantum master equation for the atoms by adiabatically eliminating the cavity field (Sec. 5.3). In the bad cavity limit (Sec. 5.4), where the cavity field adiabatically fol-

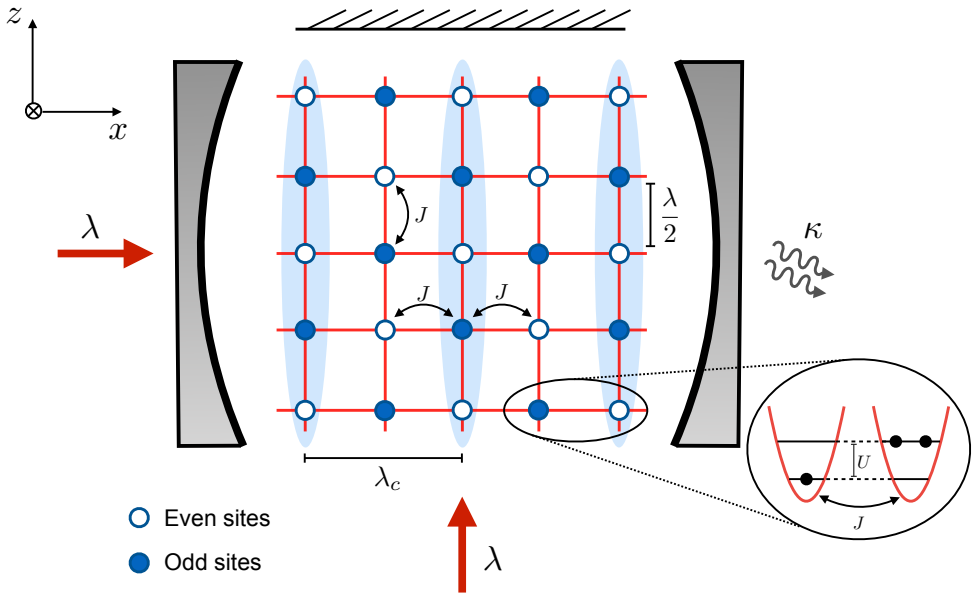

Figure 5.1: Schematic representation of the system. A gas of ultracold atoms is placed inside a high-finesse cavity with cavity wavelength λ_c and photon loss rate κ. Two lasers of wavelength λ (red arrows) form a periodic lattice potential of wavelength $\frac{\lambda}{2}$. Atoms can hop across the lattice in the x-z plane with an amplitude J and are subject to an on-site interaction U. The laser in the transverse direction also acts as an external pump which can scatter photons off the atoms into the cavity and vice versa.

lows the atoms, we recover the effective Hamiltonian studied in Refs. [26, 54, 56, 57], but supplemented with measurement-induced dephasing between states of different imbalance between the even and odd sites. The steady state is that of infinite temperature, however, the relaxation dynamics can change drastically: For small hopping (Sec. 5.4.1), the atoms explore configuration space in anomalous diffusion [112–114]. In contrast, if short- and long-range interactions are of the same order, their effects can cancel giving rise to normal diffusion. For large hopping and vanishing short-ranged interactions (Sec. 5.4.2), we show that the dynamics can be reduced to a linear rate equation predicting an exponential relaxation to the infinite-temperature state. Finally, in Sec. 5.5, we study the good cavity limit for zero on-site interactions, where optical pumping between momentum pairs enables cavity-assisted cooling, similar to the one observed in Ref. [115]. We conclude in Sec. 5.6.

The results presented in this chapter have been published in [1]. Later studies have also considered the open system dynamics by analyzing the effects of quantum noise on the ground-state phase diagram [83] and studying the light-matter entanglement in the steady state using numerical methods [116]. As an important note, at the time of writing this thesis, we found an error in the calculations of the relaxation dynamics in [1]. Despite the correction being of high physical relevance, the results obtained in [1] remain correct

to a large extent. The calculation details comparing the results in [1] and the correct results, described in Sec. 5.4.1, are presented in Appendix 5.A.

5.2 Model

We consider a gas of ultracold atoms placed inside an optical cavity, in the presence of an external optical lattice and driven by a pump laser in the direction transverse to the cavity axis (see Fig. 5.1). We focus on the case where the cavity wavelength λ_c is commensurate with that of the lasers forming the lattice $\lambda_c = \lambda$. Such a system can be described with the BH model including an atom-light interaction term [26], which in the rotating frame of the pump reads

$$\hat{H} = \hat{H}_U + \hat{H}_J + \hat{H}_\Delta + g(\hat{a}^\dagger + \hat{a})\hat{\Phi}, \tag{5.1}$$

with $\hat{H}_U + \hat{H}_J = \frac{U}{2}\sum_i \hat{n}_i\,(\hat{n}_i - 1) - J\sum_{\langle i,j\rangle} \hat{b}_i^\dagger \hat{b}_j$ the BH Hamiltonian, being $\hat{n}_i = \hat{b}_i^\dagger \hat{b}_i$ the atomic number operator at site i and $\hat{\Phi} = \sum_e \hat{n}_e - \sum_o \hat{n}_o$, where e/o stands for even/odd sites. The operators $\hat{a}$ and $\hat{b}$ obey bosonic commutation relations. Here, J is the nearest neighbor hopping amplitude and U the on-site interaction strength. The third term represents the cavity photons $\hat{H}_\Delta = -\Delta \hat{a}^\dagger \hat{a}$, where $\Delta = \omega_\mathrm{p} - \omega_\mathrm{cav}$ is the laser detuning with respect to the cavity mode, and the last term is the light-matter coupling induced by the pump. This interaction corresponds to photon scattering between the pump field and the cavity mode, which is determined by the atomic distribution across the lattice. The derivation of the Hamiltonian (5.1) can be found in Sec. 1.5.

We include cavity losses using the Lindblad master equation

$$\partial_t \hat{\rho} = \mathcal{L}\hat{\rho} \equiv (-i)[\hat{H}, \hat{\rho}] + \kappa \mathcal{D}[\hat{a}](\hat{\rho}) \tag{5.2}$$

where $\mathcal{D}[\hat{a}](\star) \equiv \hat{a}\ \star\ \hat{a}^\dagger - \frac{1}{2}\ \{\hat{a}^\dagger \hat{a}, \star\}$ and κ is the rate of photon loss. As we are most interested in characterizing the atomic dynamics, we focus on the case of weak light-matter coupling g. In this regime, we can adiabatically eliminate the photonic degrees of freedom and obtain an effective description for the atoms.

5.3 Adiabatic elimination

In this section, we adiabatically eliminate the cavity photons using the Nakajima-Zwanzigg formalism [59, 60, 69, 70], following the same steps as in Sec. 2.2. This yields

an effective equation of motion for the reduced atomic density matrix to second order in the light-matter coupling g

$$\mathcal{P}\hat{\rho}_{\rm tot}(t) = \mathcal{P}\mathcal{L}_{\rm at}\mathcal{P}\hat{\rho}_{\rm tot}(t) + g^2\mathcal{P}\mathcal{L}_{\rm int}\int_0^\infty dt'\; e^{(\mathcal{L}_{\rm at}+\mathcal{L}_{\rm ph})t'}\mathcal{L}_{\rm int}\mathcal{P}\hat{\rho}_{\rm tot}(t-t'), \tag{5.3}$$

where the projector $\mathcal{P}$ is defined as $\mathcal{P}\hat{\rho}_{\rm tot}(t) = {\rm Tr}_{\rm ph}[\hat{\rho}(t)] \otimes \hat{\rho}_{\rm ph}^{\rm ss}$, with $\hat{\rho}_{\rm ph}^{\rm ss}$ the steady state density matrix for the photons in the absence of coupling. The Liouvillian terms are defined as $\mathcal{L}_{\rm at}\hat{\rho}_{\rm tot} = (-i)[\hat{H}_U + \hat{H}_J, \hat{\rho}_{\rm tot}]$, $\mathcal{L}_{\rm ph}\hat{\rho}_{\rm tot} = (-i)[\hat{H}_\Delta, \hat{\rho}_{\rm tot}] + \kappa\mathcal{D}[\hat{a}](\hat{\rho}_{\rm tot})$ and $\mathcal{L}_{\rm int}\hat{\rho}_{\rm tot} = (-i)[\hat{H}_{\rm int}, \hat{\rho}_{\rm tot}]$.

To take the trace over the photon sector, we need to consider correlation functions of the form $\langle\hat{\xi}(t)\hat{\xi}(t')\rangle$, with $\hat{\xi} = \hat{a}^\dagger + \hat{a}$ and where $\langle\dots\rangle$ denotes an average for $g = 0$. These can be obtained by considering the bath coupled to the light field as a zero-temperature source of white noise, i.e. the only non-vanishing correlation function is $\langle\hat{a}_{\rm in}(t)\hat{a}_{\rm in}^\dagger(t')\rangle = \delta(t-t')$, where $\hat{a}_{\rm in}$ and $\hat{a}_{\rm in}^\dagger$ are input noise operators [117]. This yields $\langle\hat{\xi}(t)\hat{\xi}(t')\rangle = \langle\hat{a}(t)\hat{a}^\dagger(t')\rangle = e^{-\frac{\kappa}{2}|t-t'|+i\Delta(t-t')}$. Inserting this into (5.3) and tracing over the cavity mode, we obtain

$$\dot{\hat{\rho}}_{\rm at}(t) = \mathcal{L}_{\rm at}\hat{\rho}_{\rm at}(t) - g^2\int_0^\infty dt'\Big(e^{-\frac{\kappa}{2}|t'|+i\Delta t'}[\hat{\Phi}(0), \hat{\Phi}(-t')\hat{\rho}_{\rm at}(t)] + e^{-\frac{\kappa}{2}|t'|-i\Delta t'}[\hat{\rho}_{\rm at}(t)\hat{\Phi}(-t'), \hat{\Phi}(0)]\Big), \tag{5.4}$$

where $\hat{\rho}_{\rm at}(t) = {\rm Tr}_{\rm ph}[\hat{\rho}(t)]$, $\hat{\Phi}(t) = e^{i\hat{H}_{\rm at}t}\hat{\Phi}e^{-i\hat{H}_{\rm at}t}$ and we have made use of the Markov approximation. Since (5.4) is an integro-differential equation, it is difficult to use in practice.

The imbalance operator $\hat{\Phi} = \sum_e \hat{n}_e - \sum_o \hat{n}_o$ commutes with the on-site interactions $[\hat{H}_U, \hat{\Phi}] = 0$, so its free evolution is $\hat{\Phi}(t) = e^{i\hat{H}_J t}\hat{\Phi}e^{-i\hat{H}_J t}$. In the quasimomentum basis $\hat{b}_k = \frac{1}{\sqrt{K}}\sum_j \hat{b}_j e^{ikj}$, where j denotes the lattice sites, K is the total number of sites, and $k = \frac{2\pi}{K}n$ the quasimomentum with $n = 0, \dots, K$ an integer, $\hat{H}_J = \sum_k \varepsilon_k \hat{b}_k^\dagger\hat{b}_k$ and $\hat{\Phi} = \sum_k \hat{b}_k^\dagger\hat{b}_{k-k_\pi}$, with $k_\pi = \pi$. We then have $\hat{\Phi}(t) = \sum_k e^{i(\varepsilon_k - \varepsilon_{k-k_\pi})t}\; \hat{b}_k^\dagger\hat{b}_{k-k_\pi}$. Using this property, we can integrate over t' and obtain

$$\dot{\hat{\rho}}_{\rm at} = (-i)[\hat{H}_U + \hat{H}_J, \hat{\rho}_{\rm at}] + g^2\sum_{k\in{\rm BZ}}\Big\{G(-\varepsilon_k + \varepsilon_{k-k_\pi})[\hat{b}_k^\dagger\hat{b}_{k-k_\pi}\hat{\rho}_{\rm at}, \hat{\Phi}] - G^*(\varepsilon_k - \varepsilon_{k-k_\pi})[\hat{\rho}_{\rm at}\hat{b}_k^\dagger\hat{b}_{k-k_\pi}, \hat{\Phi}]\Big\} \tag{5.5}$$

with

$$G(\omega) = \int_0^\infty dt'\; e^{-\frac{\kappa}{2}|t'|+i(\Delta+\omega)t'} = \frac{\kappa/2}{(\Delta+\omega)^2 + \kappa^2/4} + i\frac{\Delta+\omega}{(\Delta+\omega)^2+\kappa^2/4}, \tag{5.6}$$

where the sums over k run over the first Brillouin zone (BZ) $k \in [-\pi, \pi)$. Equation (5.5) is a Markovian quantum master equation that is local in time. However, its non-Lindblad form makes its physical interpretation not straightforward.

It is possible to bring (5.5) into Lindblad form in two different regimes: the bad cavity limit $J \ll (\kappa, |\Delta|)$, where $G(\omega)$ becomes independent of ω, and in the good cavity limit, where terms of the form $(\hat{b}_k^\dagger \hat{b}_{k-k_\pi})^2$ can be safely neglected using a rotating wave approximation (RWA). In the following, we focus on the bad cavity limit and discuss the good cavity limit in Sec. 5.5.

5.4 Bad-cavity regime $J \ll (\kappa, |\Delta|)$

In the bad cavity limit $J \ll (\kappa, |\Delta|)$, the cavity follows the dynamics of the atoms adiabatically, and $G(\omega) = \frac{\kappa/2}{\Delta^2+\kappa^2/4} + i\frac{\Delta}{\Delta^2+\kappa^2/4}$, which allows us to bring (5.5) into Lindblad form

$$\dot{\hat{\rho}}_{\text{at}} = (-i)[\hat{H}_{\text{eff}}, \hat{\rho}_{\text{at}}] + \gamma \mathcal{D}[\hat{\Phi}](\hat{\rho}_{\text{at}}) \tag{5.7}$$

with

$$\hat{H}_{\text{eff}} = \hat{H}_U + \hat{H}_J + \hat{H}_{U_l}, \tag{5.8}$$

where

$$\hat{H}_{U_l} = -\frac{U_l}{K}\left(\sum_e \hat{n}_e - \sum_o \hat{n}_o\right)^2, \tag{5.9}$$

with

$$U_l = -Kg^2 \text{Im}[G(\varepsilon_k - \varepsilon_{k-k_\pi})] = -K\frac{g^2\Delta}{\Delta^2 + \frac{\kappa^2}{4}} \tag{5.10}$$

$$\gamma = 2g^2 \text{Re}[G(\varepsilon_k - \varepsilon_{k-k_\pi})] = \frac{g^2\kappa}{\Delta^2 + \frac{\kappa^2}{4}}. \tag{5.11}$$

The effective Hamiltonian (5.8) features hopping, on-site interactions, and infinite-range interactions $\hat{H}_{U_l}$, a consequence of the global coupling of all atoms to the single-mode cavity field. The Hamiltonian (5.8) has been previously studied in Refs. [54, 56, 57] where it was shown that the ground-state phase diagram exhibits four phases classified by the presence or absence of atomic coherence and even-odd imbalance.

Crucially, we find that there is dephasing between atomic configurations corresponding to different imbalance with rate γ, which comes as the dissipative counterpart to the coherent long-range interactions $\hat{H}_{U_l}$. Since $\hat{\Phi}$ is Hermitian, the dissipator can be rearranged as a commutator with the density matrix $\mathcal{D}[\hat{\Phi}]\hat{\rho}_{\text{at}} = \frac{1}{2}[\hat{\Phi}, [\hat{\rho}_{\text{at}}, \hat{\Phi}]]$, meaning that the steady state $\hat{\rho}_{\text{at}}^{\text{ss}}$ needs to obey $[\hat{\rho}_{\text{at}}^{\text{ss}}, \hat{H}_{\text{eff}}] = [\hat{\rho}_{\text{at}}^{\text{ss}}, \hat{\Phi}] = 0$.

For $J = 0$, the Hamiltonian and the jump operator satisfy $[\hat{H}_{\text{eff}}, \hat{\Phi}] = 0$, making the quantum master equation (5.7) exactly solvable. Since both $\hat{H}_{\text{eff}}$ and $\hat{\Phi}$ are diagonal in

the site basis, the steady states correspond to number states in this basis. The dissipator in (5.7) eliminates coherences between states associated with different eigenvalues of $\hat{\Phi}$, but does not affect coherences between states where these are equal. For a general initial state, expressed in number state basis, this means the density matrix can be decomposed in blocks, corresponding to different eigenvalues of $\hat{\Phi}$, which remain unchanged by dynamical evolution and will preserve coherence in the long time limit. Steady states with non-vanishing coherences are usually referred to as decoherence free subspaces [118] and have been subject of much investigation due to potential applications for quantum computing [119].

For $J \neq 0$, $\hat{H}_{\text{eff}}$ and $\hat{\Phi}$ do not commute anymore $[\hat{H}_{\text{eff}}, \hat{\Phi}] \neq 0$. From this, it follows that the steady state is unique and $\hat{\rho}_{\text{at}}^{\text{ss}} \propto \mathbb{1}$. This corresponds to a steady state of the form $\hat{\rho}(t = \infty) = \frac{1}{M} \sum_{\mathbf{n}} |\mathbf{n}\rangle\langle\mathbf{n}|$, where $\mathbf{n} = (n_1, n_2, ..., n_K)$ denotes a specific atomic configuration and $M = \binom{K+N-1}{N}$, i.e. the external pump eventually heats the system up to the completely mixed (infinite-temperature) steady state.

In the following, we will study the relaxation dynamics towards the infinite-temperature steady state. We find two different regimes: for small hopping the interplay between interactions and dissipation leads to (normal and anomalous) diffusion [112, 113], while for large hopping the steady state is approached exponentially.

5.4.1 Small hopping limit $J \ll (U, U_l, \gamma)$

Following [112–114], we start our analysis by perturbatively eliminating the density matrix coherences, given that for strong interactions and in the presence of dephasing these should not play an important role in the evolution of the system. This yields an effective description in terms of the diagonal elements of $\hat{\rho}_{\text{at}}$. We then simplify the problem by introducing a mean-field decomposition and obtain analytical results in the limit of large particle filling, where we can derive a continuum description for the equations of motion.

The equations of motion for the coherences can be approximated to

$$\begin{aligned}\partial_t \rho_{\mathbf{n}}^{\mathbf{n}+e_{e,o}^d} \simeq & d\left[-iU(n_e - n_o + d) + i\frac{4U_l}{K}(\phi_0 + d) - 2\gamma\right]\rho_{\mathbf{n}}^{\mathbf{n}+e_{e,o}^d} \\ & + iJ\sqrt{n_e + \delta_{d,1}}\sqrt{n_o + \delta_{d,-1}}\left(\rho_{\mathbf{n}}^{\mathbf{n}} - \rho_{\mathbf{n}+e_{e,o}^d}^{\mathbf{n}+e_{e,o}^d}\right), \end{aligned} \tag{5.12}$$

where $e_{i,j}^d$ is a vector whose ith component is equal to d, its jth component equal to $-d$, and the rest are equal to 0. Here the labels e and o refer to a specific even-odd pair of sites. Note that in Eq. (5.12) we have assumed $d = \pm 1$. We focus on this set of coherences

since they are the only ones coupled to the diagonal elements. We have also introduced the imbalance $\phi_0(\mathbf{n}) = \sum_e n_e - \sum_o n_o$. The approximate sign stands for having ignored the coupling to other coherences, which barely influences the dynamics in this limit. Using $J \ll (U, U_l, \gamma)$ we can integrate (5.12) to obtain

$$\rho_{\mathbf{n}}^{\mathbf{n}+e^d_{e,o}} \simeq \frac{dJ\sqrt{n_e+\delta_{d,1}}\sqrt{n_o+\delta_{d,-1}}}{U(n_e-n_o+d)-\frac{4U_l}{K}(\phi_0+d)-2i\gamma}\left(\rho_{\mathbf{n}}^{\mathbf{n}}-\rho_{\mathbf{n}+e^d_{e,o}}^{\mathbf{n}+e^d_{e,o}}\right), \tag{5.13}$$

where we have neglected the transient terms and kept terms up first order in $(J/U, J/U_l, J/\gamma)$ (see Supplemental Material in [114] for further details). Inserting this in the equations of motion for the diagonal elements, we obtain

$$\begin{aligned}\partial_t \rho_{\mathbf{n}}^{\mathbf{n}} = 4\gamma J^2 \sum_{\substack{\langle i,j\rangle \\ d=\pm 1}} \Bigg[&\delta_{i\in e}\frac{(n_i+\delta_{d,1})(n_j+\delta_{d,-1})}{[U(n_i-n_j+d)-\frac{4U_l}{K}(\phi_0+d)]^2+4\gamma^2}\left(\rho_{\mathbf{n}+e^d_{i,j}}^{\mathbf{n}+e^d_{i,j}}-\rho_{\mathbf{n}}^{\mathbf{n}}\right)+ \\ &\delta_{i\in o}\frac{(n_j+\delta_{d,1})(n_i+\delta_{d,-1})}{[U(n_j-n_i+d)-\frac{4U_l}{K}(\phi_0+d)]^2+4\gamma^2}\left(\rho_{\mathbf{n}+e^d_{j,i}}^{\mathbf{n}+e^d_{j,i}}-\rho_{\mathbf{n}}^{\mathbf{n}}\right)\Bigg].\end{aligned} \tag{5.14}$$

We now simplify the form of (5.14) using a Gutzwiller ansatz

$$\hat{\rho}(t) = \bigotimes_{j=1}^{K}\left[\sum_{n_j}\rho_j(n_j,t)|n_j\rangle\langle n_j|\right], \tag{5.15}$$

where we only make a distinction between even and odd sites $\rho_e(m,t) \neq \rho_o(m,t)$, but consider all even/odd to be equivalent among themselves $\rho_{e(o)}(m,t) = \rho_{e'(o')}(m,t)$. In this form, the trace condition on the density matrix translates to $\sum_{n_j}\rho_j(n_j,t) = 1$. Plugging this ansatz into (5.14) yields (see Appendix 5.A for details)

$$\begin{aligned}\partial_t\rho_e(n_i,t) = 4z\gamma J^2 &\sum_{\substack{\{n_k\}\\ k\neq i}}\sum_{d=\pm1}\frac{(n_i+\delta_{d,1})(n_j+\delta_{d,-1})}{[U(n_i-n_j+d)-\frac{4U_l}{K}(n_i-n_j+d+\varphi_{\mathbf{n}})]^2+4\gamma^2} \\ &\times\left(\prod_{\substack{p\in e\\ p\neq i}}\rho_e(n_p,t)\right)\left(\prod_{\substack{q\in o\\ q\neq j}}\rho_o(n_q,t)\right)\Big(\rho_e(n_i+d,t)\rho_o(n_j-d,t)-\rho_e(n_i,t)\rho_o(n_j,t)\Big) \\ \partial_t\rho_o(n_i,t) = 4z\gamma J^2 &\sum_{\substack{\{n_k\}\\ k\neq i}}\sum_{d=\pm1}\frac{(n_i+\delta_{d,1})(n_j+\delta_{d,-1})}{[U(n_i-n_j+d)-\frac{4U_l}{K}(n_i-n_j+d-\varphi_{\mathbf{n}})]^2+4\gamma^2} \\ &\times\left(\prod_{\substack{p\in e\\ p\neq j}}\rho_e(n_p,t)\right)\left(\prod_{\substack{q\in o\\ q\neq i}}\rho_o(n_q,t)\right)\Big(\rho_o(n_i+d,t)\rho_e(n_j-d,t)-\rho_o(n_i,t)\rho_e(n_j,t)\Big),\end{aligned} \tag{5.16}$$

where z is the coordination number and we have split the imbalance $\phi_0(\mathbf{n})$ into the contribution from i and j and the contribution from the rest of the lattice $\varphi_{\mathbf{n}} = \sum_{p\in e, p\neq i} n_p - \sum_{q\in o, q\neq j} n_q$. By integrating these equations numerically we can access all the properties of the system. In this language, the steady state of the system now adopts the form $\rho_{e(o)}(n, t=\infty) = \frac{1}{M}\binom{K+N-n-2}{N-n}$. Considering the limit of large system size $K \to \infty$, this can be recasted as $\rho_{e(o)}(n, t=\infty) \simeq f^{n+1}/[f(1+f)^{n+1}]$ using Stirling's formula, where $f = N/K$ is the lattice filling.

To explore (5.16) analytically, we follow Refs. [112–114] by considering the limit of large filling f and introducing a continuous variable $x = n/f$. The probability distributions are redefined as $p_{e(o)}(x = n/f, t) = f\rho_{e(o)}(n, t)$, with $p_{e(o)}((n+1)/f, t) = p_{e(o)}(x, t) + \partial_x[p_{e(o)}(x, t)]dx$ and the steady state given by $p_{e(o)}(x, \infty) = e^{-x}$. In the continuum limit, the equations of motion (5.16) read

$$\partial_t p_{e(o)}(x,t) = \frac{4z\gamma J^2}{f^2}\partial_x\Big[D_{o(e)}(x,t)\partial_x p_{e(o)}(x,t) - F_{o(e)}(x,t)p_{e(o)}(x,t)\Big]. \tag{5.17}$$

In this expression we have introduced the diffusion functions

$$D_e(x,t) = \int d\vec{x}\int dy \frac{xy}{[U(x-y) - \frac{4U_l}{K}(x-y+\varphi(\vec{x}))]^2 + \frac{4\gamma^2}{f^2}}\left(\prod_{\substack{p\in e\\ x_p\neq x}} p_e(x_p,t)\right)\left(\prod_{\substack{q\in o\\ x_q\neq y}} p_o(x_q,t)\right)p_o(y,t)$$

$$D_o(x,t) = \int d\vec{x}\int dy \frac{xy}{[U(x-y) - \frac{4U_l}{K}(x-y-\varphi(\vec{x}))]^2 + \frac{4\gamma^2}{f^2}}\left(\prod_{\substack{p\in e\\ x_p\neq y}} p_e(x_p,t)\right)\left(\prod_{\substack{q\in o\\ x_q\neq x}} p_o(x_q,t)\right)p_e(y,t),$$

and the force functions

$$F_e(x,t) = \int d\vec{x}\int dy \frac{xy}{[U(x-y) - \frac{4U_l}{K}(x-y+\varphi(\vec{x}))]^2 + \frac{4\gamma^2}{f^2}}\left(\prod_{\substack{p\in e\\ x_p\neq x}} p_e(x_p,t)\right)\left(\prod_{\substack{q\in o\\ x_q\neq y}} p_o(x_q,t)\right)\partial_y p_o(y,t)$$

$$F_o(x,t) = \int d\vec{x}\int dy \frac{xy}{[U(x-y) - \frac{4U_l}{K}(x-y-\varphi(\vec{x}))]^2 + \frac{4\gamma^2}{f^2}}\left(\prod_{\substack{p\in e\\ x_p\neq y}} p_e(x_p,t)\right)\left(\prod_{\substack{q\in o\\ x_q\neq x}} p_o(x_q,t)\right)\partial_y p_e(y,t),$$

where the integrals run over all variables $x_{p,q}$ and y, with $\varphi(\vec{x}) = \sum_{p\in e} x_p - \sum_{q\in o} x_q$. The expressions $x_{p,q} \neq x$ and $x_{p,q} \neq y$ in the products refer to the fact that each product contains $\frac{K}{2} - 1$ factors, corresponding to the infinite-range coupling between the pair of sites we consider and the rest of the system. The highly complicated dependence of the diffusion and force functions on the probability distributions makes it very difficult to approach Eq. (5.17) for a generic case. Thus, we analyze (5.17) in the limits where analytical solutions can be obtained. We distinguish two regimes: one in which one of

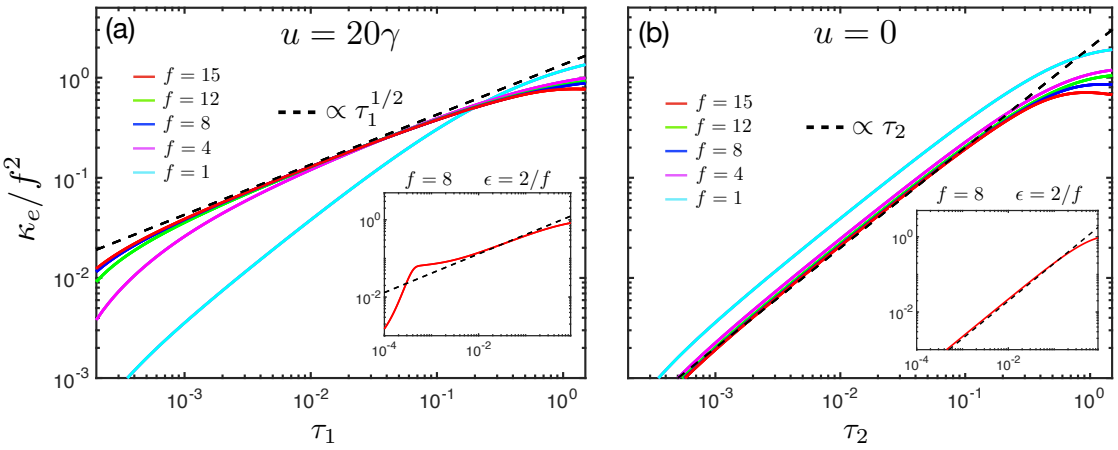

Figure 5.2: Dynamical evolution of the local particle fluctuations of the even sites for different fillings and $x_e = x_o = 1$ in the two different regimes from (5.16) (solid color lines). The insets show the evolution for $x_e = 1 + \epsilon$ and $x_o = 1 - \epsilon$ in the case of a double well $K = 2$. Dashed black lines correspond to the analytical results (5.20) and (5.23) in the main figures, and to the Eqs (5.25) and (5.26) in the insets.

the interactions is strongly dominant, either short or long range, and a second one when they are both of the same order. As we will see, this has a strong impact in the relaxation dynamics. In particular, we will consider sharply peaked and symmetrically distributed initial conditions of the form $p_{e(o)}(x, 0) = \delta(x - x_{e(o)})$. This allows us to ignore the effects of the force functions $F_{e(o)}(x, t)$ at short times.

We first consider initializing the system in the MI phase, with $x_e = x_o = x_0$. For $U \neq 4U_l/K$, with either $U \ll 4U_l/K$ or $U \gg 4U_l/K$, at very short times, the dynamics around the initial points can then be approximated by

$$\partial_{\tau_1} p_{e(o)}(x, \tau_1) = \partial_x \left[\left(\frac{x_0^2}{(x - x_0)^2 + \frac{4\gamma^2}{u^2 f^2}} \right) \partial_x p_{e(o)}(x, \tau_1) \right], \tag{5.18}$$

where we introduced the parameter $u = U - 4U_l/K$ and the dimensionless time $\tau_1 = t/t_1^*$, with $t_1^* = \frac{u^2 f^2}{4zJ^2\gamma}$. Hence, when referring to short times, we mean $\tau_1 \ll 1$. Note that for initial conditions in the MI phase, the effects of the imbalance term $\varphi(\vec{x})$ disappear[1]. This gives numerical access to Eqs. (5.16) at short times, as the terms inside the product can be traced out. We can then obtain an analytical solution for Eq. (5.18). By ignoring the term of order γ/uN in the denominator we find a scaling solution of the form $p_e(x, \tau_1) =$

[1]This turns out to remain true throughout the entire time evolution and can be shown by computing the time evolution of $\langle \hat{\Phi} \rangle$. There, it is possible to see that, within our mean-field approximation, choosing $x_e = x_o$ leads to $\langle \hat{\Phi} \rangle = 0$ at all times.

$g_e(\xi)/\tau_1^\nu$ with $\xi = x/\tau_1^\nu$, leading to

$$p_{e(o)}(x, \tau_1) = \frac{1}{4\Gamma(5/4)(x_0^2\tau_1)^{1/4}} e^{-\frac{(x-x_0)^4}{16\tau_1 x_0^2}}. \tag{5.19}$$

This corresponds to anomalous diffusion of the probability distribution at short times. Using (5.19), we can readily obtain the local number fluctuations $\kappa_i = \langle \hat{n}_i^2 \rangle - \langle \hat{n}_i \rangle^2$, which reads

$$\frac{\kappa_{e(o)}}{f^2} = \frac{\Gamma(3/4)}{\Gamma(5/4)} x_0 \sqrt{\tau_1}. \tag{5.20}$$

This initial fast growth of the fluctuations can be understood as the system starting to explore neighboring configurations, separated by a small energy barrier from the initial state. Anomalous diffusion was also obtained in [113] for a BH model under the effects of local dephasing. This indicates that the impact of strong interactions on the dynamics is independent of their range of action and that the global nature of the dephasing in (5.7) does not play a major role within this level of approximation.

In Fig. 5.2(a) we show the time evolution of the local particle number fluctuations of the even sites for $uN/\gamma \gg 1$ and $x_e = x_o = 1$, resulting from numerical integration of (5.16). We see that correlations do follow the power-law behavior predicted from the analysis in the continuous limit. As expected, the analytical results become more accurate for increasing values of the particle filling.

In the opposite limit, where interactions are of the same order, i.e. $uN/\gamma \ll 1$, the behavior of the system becomes notably different. Assuming same initial conditions as before, i.e. ignoring the force terms and the imbalance function, the dynamics around the initial points reduce to

$$\partial_{\tau_2} p_{e(o)}(x, \tau_2) = x_0^2 \partial_x^2 p_{e(o)}(x, \tau_2), \tag{5.21}$$

where we introduced a new dimensionless time $\tau_2 = t/t_2^*$, where $t_2^* = \frac{\gamma}{zJ^2}$, and with short times corresponding to $\tau_2 \ll 1$. Analogously to the previous case, this equation also allows for a scaling solution, leading to

$$p_{e(o)}(x, \tau_2) = \frac{1}{2x_0\sqrt{\pi\tau_2}} e^{-\frac{(x-x_0)^2}{4x_0^2\tau_2}} \tag{5.22}$$

and local number fluctuations

$$\frac{\kappa_{e(o)}}{f^2} = 2x_0^2\tau_2. \tag{5.23}$$

This corresponds to normal diffusion, characterized by the linear growth of κ_e in time. The emergence of this regime in the limit $uN/\gamma \to 0$ can be understood in terms of

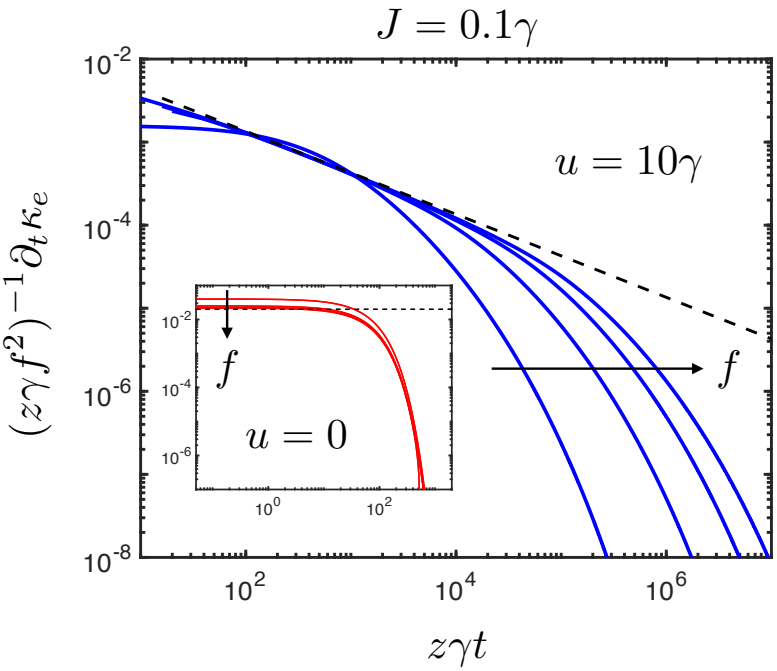

Figure 5.3: Dynamical evolution of the time derivative of the local particle number fluctuations for different values of the filling $f = 1, 4, 8, 12$ and initial conditions in the MI phase, with $x_0 = 1$. We observe how for $uN/\gamma \gg 1$ the time-scales at which the steady state is reached become larger for increasing filling, consequence of the large energy splitting with the states associated with high on-site population ($x \gg 1$). In contrast, for $uf/\gamma \ll 1$, the steady state is approached orders of magnitude faster as all configurations are energetically degenerate. Dashed black lines correspond to the analytical predictions for short times (5.20) and (5.23).

the spectrum of the effective Hamiltonian (5.8) for $J = 0$. For $u = 0$, all atomic states become degenerate. As a result, the system explores every configuration at the same rate, meaning that the evolution of the probability distribution is the same at every point in x, corresponding to a normal diffusion process in configuration space. In Fig. 5.2(b) we present the evolution of κ_e/f^2 for $uN/\gamma = 0$. We find good agreement between numerical results and (5.23) that improves for larger filling f.

The long time behavior of the system can also be understood in terms of the energy spectrum of (5.8). For $uN/\gamma \gg 1$, after the distribution reaches the $x = 0$ boundary, the dynamics becomes dominated by the $x \gg 1$ region. These configurations are associated to states with large occupation numbers and have a high energy cost to populate. As a result, there is a slowdown of the dynamics, which becomes more pronounced for higher fillings. This is shown in Fig. 5.3, where one can see how for higher values of f the approach of the steady state becomes increasingly slower. This phenomenon was also observed in [113], where it is shown that correlations exhibit a stretched exponential behavior

$\kappa_e(\tau_1) \propto e^{-\alpha\sqrt{\tau_1}}$. For $uN/\gamma \ll 1$, this is no longer the case due to the energy degeneracy among the different atomic configurations, which allows the probability distribution to explore all the configuration space at the same rate, leading to a much faster approach of the steady state distribution. This behavior can be observed in the inset of Fig. 5.3, where the time at which the steady state is reached is orders of magnitude smaller than in the $uN/\gamma \gg 1$ case.

If we now consider initializing the system in the DW phase, namely, with a finite imbalance between even and odd sites, $x_e = 1 + \epsilon$ and $x_o = 1 - \epsilon$, the situation becomes more complicated. The contribution from the imbalance $\varphi(\vec{x}) = (\frac{K}{2} - 1)2\epsilon \simeq K\epsilon$, since $K \gg 1$, leads to an effective diffusion function of the form

$$D_{e(o)(x)} \simeq \frac{x_e x_o}{[(U - \frac{4U_l}{K})(x - x_{e(o)}) \pm 4U_l\epsilon]^2 + \frac{4\gamma^2}{f^2}}. \tag{5.24}$$

From this expression, one can obtain analytical expressions similar to Eqs. (5.19) and (5.22), depending on the system parameters[2]. From the form of the diffusion function (5.24), we find four different regimes. First, for $U \gg 4U_l$, we recover anomalous diffusion with time scale given by t_1^*. For $U \sim 4U_l$, same anomalous diffusion is obtained, with time scale t_1^*, but with shifted initial points, $x_e' = x_e - \frac{4U_l\epsilon}{K}$ and $x_o' = x_o + \frac{4U_l\epsilon}{K}$ for the probability distribution. When $U \ll 4U_l$, but $U \sim \frac{4U_l}{K}$, the x dependence in the denominator disappears, leading again to normal diffusion but now with a new timescale $t_3^* = \frac{4U_l^2\epsilon^2 f^2}{zJ^2\gamma}$. We expect this time scale to be particularly large given that $U_l \propto K$. Finally, for $U \ll \frac{4U_l}{K}$, anomalous diffusion re-emerges, with a time scale given by t_1^*, but with modified initial points $x_e' = x_e + K\epsilon$ and $x_o' = x_o - K\epsilon$. Note that in all these cases we have also assumed $\gamma/f \ll (U, U_l)$, as in [112–114].

Although it is still possible to make analytical predictions in the same way as for the MI case, it is not feasible to contrast them numerically with the solutions from Eq. (5.16). More specifically, the contribution from the imbalance term forces one to include terms inside the product, making the calculation unfeasible. Nevertheless, we still expect the analytical results to be accurate, given the strong of matching in the MI case. As a way of assessing the level of impact of the imbalance in the initial conditions, we consider the case of a double well , where $\varphi(\vec{x}) = 0$, which allows for a numerical treatment. Despite it being a crude simplification, we obtain a few insightful differences with respect to the MI case. Taking $K = 2$ and $\varphi(\vec{x}) = 0$ results in solutions analogous to Eqs. (5.19) and

[2]We assume $\epsilon \sim K^{-1}$, given that for smaller values it can be neglected and that $\epsilon \sim 1$ would correspond to imbalances of order f, which in the $f \gg 1$ limit does not comprise a realistic experimental situation.

(5.22), with

$$p_{e(o)}(x,\tau_1) = \frac{1}{4\Gamma(5/4)(x_e x_o \tau_1)^{1/4}} e^{-\frac{(x-x_{e(o)})^4}{16\tau_1 x_e x_o}} \qquad \frac{\kappa_{e(o)}}{f^2} = \frac{\Gamma(3/4)}{\Gamma(5/4)}\sqrt{x_e x_o \tau_1} \quad (5.25)$$

for finite u and

$$p_{e(o)}(x,\tau_2) = \frac{1}{2\sqrt{\pi x_e x_o \tau_2}} e^{-\frac{(x-x_{e(o)})^2}{4x_e x_o \tau_2}} \qquad \frac{\kappa_{e(o)}}{f^2} = 2x_e x_o \tau_2 \quad (5.26)$$

for $u = 0$. The insets in Fig. 5.2 show the evolution of the correlations for initial conditions with imbalance 2ϵ. On the one hand, for finite u we observe that the imbalance results in a delayed approach of the algebraic regime (5.20). This arises as the peaks of the effective diffusion distributions in Eqs. (5.24) and the initial probabilities are centered at different points. Thus, the probability distribution needs a certain amount of time to broaden before exploring the region of space that leads to (5.19). For large enough ϵ, the anomalous diffusive behavior can get washed out if the broadening time required by $p_{e(o)}(x,\tau_1)$ is larger than the time it takes to reach the reflective boundary at $x = 0$, where $F_{e(o)}(x,\tau_1) \approx 0$ stops being a good approximation. On the other hand, for $u = 0$, we see that an initial imbalance does not modify the evolution of the correlations, this follows from the diffusion function being homogeneous, i.e. it has the same form independently of the initial point of the neighboring site. Finally, in the long time limit, the same energetic arguments used in the MI case apply here. Thus, a slowdown of the dynamics is expected for finite u and a fast approach of the steady state for $u \approx 0$.

5.4.2 Large hopping limit $J \gg (U, U_l, \gamma)$

We now return to Eq. (5.7) and consider the limit where the hopping amplitude is the dominant energy scale $J \gg (U, U_l, \gamma)$. For convenience, we will consider vanishing onsite interactions $U = 0$. In this regime, it is best to work in momentum space, so we start with Eq. (5.5) in the limit $J \ll (|\Delta|, \kappa)$. To simplify the problem, we move to an interaction picture, taking $\hat{H}_J$ as the free Hamiltonian, and perform a RWA, i.e. we eliminate all the left over rotating terms. This yields

$$\dot{\hat{\rho}}_{\text{at}} = (-i)[\hat{H}_{\text{eff}}, \hat{\rho}_{\text{at}}] + \gamma \sum_{k=0}^{k<\pi} \Big\{ \mathcal{D}[\hat{b}_k^\dagger \hat{b}_{k-k_\pi}](\hat{\rho}_{\text{at}}) + \mathcal{D}[\hat{b}_{k-k_\pi}^\dagger \hat{b}_k](\hat{\rho}_{\text{at}}) \Big\}, \quad (5.27)$$

$$\hat{H}_{\text{eff}} = \sum_{k=0}^{k<\pi} \Big[(\varepsilon_k + \delta)\hat{n}_k + (\varepsilon_{k-k_\pi} + \delta)\hat{n}_{k-k_\pi} + 2\delta \hat{n}_k \hat{n}_{k-k_\pi} \Big], \quad (5.28)$$

with $\hat{n}_k = \hat{b}_k^\dagger \hat{b}_k$ and $\delta = g^2\Delta/(\Delta^2 + \kappa^2/4)$.

From the definition of $\hat{\Phi}$ we know that this operator only couples pairs of momentum states with momentum differing by k_π. For $U = 0$, this means that $[\hat{n}_k + \hat{n}_{k-k_\pi}, \hat{H}_{\text{eff}}] = 0$. Together with $[\hat{n}_k + \hat{n}_{k-k_\pi}, \hat{b}_k^\dagger \hat{b}_{k-k_\pi}] = [\hat{n}_k + \hat{n}_{k-k_\pi}, \hat{b}_{k-k_\pi}^\dagger \hat{b}_k] = 0$, we find that the dynamics of each pair of momentum states is decoupled from that of the other momentum modes. For simplicity, we focus only on the states $k_0 = 0$ and $k_\pi = \pi$, with $\hat{H}_J = -J(\hat{n}_{k_0} - \hat{n}_{k_\pi})$ and $\hat{\Phi} = \hat{b}_{k_0}^\dagger \hat{b}_{k_\pi} + \hat{b}_{k_\pi}^\dagger \hat{b}_{k_0}$. The reduced version of (5.27) reads

$$\dot{\hat{\rho}}_{\text{at}} = (-i)[\hat{H}_{\text{eff}}, \hat{\rho}_{\text{at}}] + \gamma \left\{ \mathcal{D}[\hat{b}_{k_0}^\dagger \hat{b}_{k_\pi}](\hat{\rho}_{\text{at}}) + \mathcal{D}[\hat{b}_{k_\pi}^\dagger \hat{b}_{k_0}](\hat{\rho}_{\text{at}}) \right\} \tag{5.29}$$

with

$$\hat{H}_{\text{eff}} = N\delta - J(\hat{n}_{k_0} - \hat{n}_{k_\pi}) + 2\delta \hat{n}_{k_0} \hat{n}_{k_\pi}. \tag{5.30}$$

As result of the RWA, the long-ranged interactions have been reduced to a number-number interaction between the momentum states k_0 and k_π. This interaction modifies the spectrum of $\hat{H}_{\text{eff}}$ but commutes with the rest of the terms in (5.30). The form of (5.30) leads to momentum being a good quantum number $[\hat{n}_k, \hat{H}_{\text{eff}}] = 0$. This feature enables us to recast Eq. (5.29) as a linear rate equation of the form $\dot{P}_i = \sum_j (\Gamma_{j\to i} P_j - \Gamma_{i\to j} P_i)$, where P_i is the probability for the system to be in a certain state $|n_{k_0}, n_{k_\pi}\rangle$ and $\Gamma_{j\to i}$ are the transition rates between different states. This equation of motion depends linearly on the state probabilities, as opposed to the non-linear form of Eqs. (5.16). The general solution for such a rate equation corresponds to a linear combination of exponential decays. Thus, in contrast to the results of the previous section, the relaxation towards the steady state is now exponential. Note that $\Gamma_{j\to i} = \gamma$ for all i,j, leading to $P_i(t \to \infty) = 1/D$, being $D = N+1$ the size of the Hilbert space, for all i, i.e. the steady state is indeed an effective infinite temperature state as expected. In terms of average population, this corresponds to the atoms equally occupying each momentum mode $\langle \hat{n}_{k_0} \rangle = \langle \hat{n}_{k_\pi} \rangle = N/2$ in the steady state.

In Fig. 5.4(a) we present the evolution of the diagonal density matrix elements from the numerical integration of (5.29) (solid blue) and the full quantum master equation (5.2) (dashed black). As expected, all the diagonal elements exponentially approach the same steady state value and the population of the k_0 mode becomes $N/2$. The match between both numerical solutions indicate the validity of the RWA for large hopping J.

We have checked numerically that small corrections due to the rotating terms will only account for small oscillations at very short times. The effect of small but finite U is that of slowly spreading the atoms across all the available momentum states. We expect that as the atoms start populating other pairs of momentum modes differing by k_π, these will

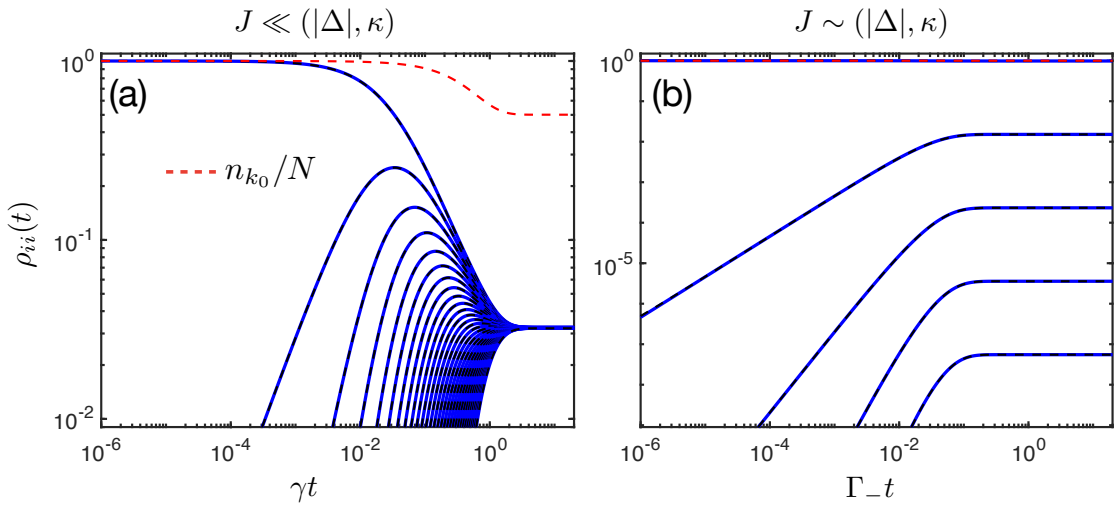

Figure 5.4: Dynamical evolution of the diagonal density matrix elements for $N = 30$ and $U = 0$, in the bad (a) and good (b) cavity regimes. The blue lines denote the solution obtained from (5.29) and the dashed black lines from (5.2). In red, the time evolution of the average number of particles in the k_0 state. Parameters: (a) $g = 10^{-4}\kappa$, $\Delta = -2\kappa$, $J = 10^{-4}\kappa$; (b) $g = 10^{-4}\kappa$, $\Delta = -2\kappa$, $J = \kappa$. In both cases all particles are initially in the momentum state $k_0 = 0$.

quickly thermalize into the steady state discussed above and eventually scatter towards other states at a rate of order $U^2/J \ll \gamma$. Once the atoms have explored all possible momentum modes, the final state will correspond to an infinite temperature state that spans the entire Hilbert space of the system, corresponding to the steady state of Eq. (5.7).

5.5 Good-cavity regime

This regime is characterized by the cavity being able to resolve the scales of atomic transitions, i.e. $J \sim (|\Delta|, \kappa)$. Thus, our starting point is Eq. (5.5). In this limit, it is only possible to bring this equation into Lindblad form by applying the RWA. For our purposes, we will again consider the limit of vanishing on-site interactions $U = 0$, in order to focus on the impact of the cavity. This leads to

$$\dot{\hat{\rho}}_{\rm at} = (-i)[\hat{H}_{\rm eff}, \hat{\rho}_{\rm at}] + \sum_{k=0}^{k<\pi} \left\{ \Gamma_{k,+} \mathcal{D}[\hat{b}_k^\dagger \hat{b}_{k-k_\pi}](\hat{\rho}_{\rm at}) + \Gamma_{k,-} \mathcal{D}[\hat{b}_{k-k_\pi}^\dagger \hat{b}_k](\hat{\rho}_{\rm at}) \right\}, \tag{5.31}$$

with

$$\hat{H}_{\rm eff} = \sum_{k=0}^{k<\pi} \Big[(\varepsilon_k + \delta_{k,-}) \hat{n}_k + (\varepsilon_{k-k_\pi} + \delta_{k,+}) \hat{n}_{k-k_\pi} + \lambda_k \hat{n}_k \hat{n}_{k-k_\pi} \Big], \tag{5.32}$$

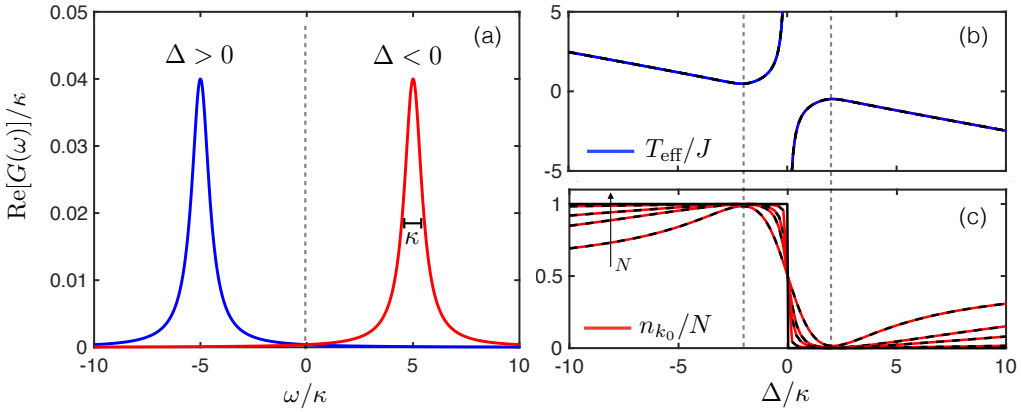

Figure 5.5: (a) The spectral function $\mathrm{Re}[G(\omega)]$ of the cavity field. For zero-temperature white noise, this corresponds to a Lorentzian function of width κ centered at $-\Delta$. For positive(negative) values of Δ, i.e. a blue(red) detuned light field, we obtain pumping of the high(low) momentum state. (b) The effective steady state temperature T_{eff} as a function of Δ/κ with $J = \kappa$. (c) Average number of particles in the low momentum state $\langle \hat{n}_{k_0} \rangle / N$ as a function of Δ/κ, with $J = \kappa$, for $N = 1, 5, 10, 50$ (dashed) and $N \to \infty$ (solid). The function becomes sharper for increasing N and develops a step at $\Delta = 0$, where it always satisfies $\langle \hat{n}_{k_0} \rangle / N = 1/2$. Vertical grey dashed lines indicate $\Delta = \pm 2J$.

where $\delta_{k,\pm} = g^2 \mathrm{Im}[G(\mp\varepsilon_k \pm \varepsilon_{k-k_\pi})]$, $\lambda_k = \delta_{k,+} + \delta_{k,-}$ and $\Gamma_{k,\pm} = 2g^2 \mathrm{Re}[G(\mp\varepsilon_k \pm \varepsilon_{k-k_\pi})]$.

We then reduce our description to a pair of representative momentum states (k_0, k_π), which reads

$$\dot{\hat{\rho}}_{\mathrm{at}} = (-i)[\hat{H}_{\mathrm{eff}}, \hat{\rho}_{\mathrm{at}}] + \Gamma_- \mathcal{D}[\hat{b}_{k_0}^\dagger \hat{b}_{k_\pi}](\hat{\rho}_{\mathrm{at}}) + \Gamma_+ \mathcal{D}[\hat{b}_{k_\pi}^\dagger \hat{b}_{k_0}](\hat{\rho}_{\mathrm{at}}) \tag{5.33}$$

with

$$\hat{H}_{\mathrm{eff}} = (\delta_- - J)\hat{n}_{k_0} + (\delta_+ + J)\hat{n}_{k_\pi} + \lambda \hat{n}_{k_0}\hat{n}_{k_\pi}, \tag{5.34}$$

where $\delta_\pm = \frac{g^2(\Delta \pm 2J)}{(\Delta \pm 2J)^2 + \kappa^2/4}$, $\lambda = \delta_+ + \delta_-$ and $\Gamma_\pm = \frac{g^2 \kappa}{(\Delta \mp 2J)^2 + \kappa^2/4)}$ are the transition rates. Analogously to (5.30), here momentum is also a good quantum number, and thus the dynamics of the states $|n_{k_0}, n_{k_\pi}\rangle$ will be purely dissipative. This again allows to rewrite the master equation (5.33) as a rate equation, where now the transitions $|n_{k_0}, n_{k_\pi}\rangle \to |n_{k_0}+1, n_{k_\pi}-1\rangle$ occur at rate Γ_- and the transitions $|n_{k_0}, n_{k_\pi}\rangle \to |n_{k_0}-1, n_{k_\pi}+1\rangle$ at rate Γ_+, leading to the rates $\Gamma_{i\to j}$ satisfying detailed balance

$$\frac{\Gamma_-}{\Gamma_+} = \frac{\frac{\kappa^2}{4} + (2J - \Delta)^2}{\frac{\kappa^2}{4} + (2J + \Delta)^2} = e^{\frac{2J}{T_{\mathrm{eff}}}} \ . \tag{5.35}$$

Note that the form of these rates follow the Lorentzian form of cavity spectral function (see Fig. 5.5(a)). In (5.35), T_{eff} stands for the effective temperature of the system. The

steady state of the system is then given by a thermal distribution whose temperature can be controlled via the detuning Δ. This enables control over the population of the atoms which can be optically pumped into either momentum mode according to

$$\langle \hat{n}_{k_0} \rangle = \frac{r - (N+1)r^{N+1} + Nr^{N+2}}{(1-r)(1-r^{N+1})}, \tag{5.36}$$

for $r \neq 1$, with $r = \Gamma_-/\Gamma_+$, and $\langle \hat{n}_{k_\pi} \rangle = N - \langle \hat{n}_{k_0} \rangle$. The case $r = 1$ corresponds to the bad cavity limit result ($\Gamma_+ = \Gamma_- = \gamma$) with $T_{\text{eff}} = \infty$ and $\langle \hat{n}_{k_0} \rangle = \frac{N}{2}$. In Fig. 5.5(b) and (c), we present the effective temperature and the population fraction of the k_0 mode as a function of the detuning. The dashed lines correspond to the results in Eqs. (5.35) and (5.36), and the solid lines to the results from numerical integration of (5.2). Note that as the number of particles N becomes very large the behavior of $\langle \hat{n}_{k_0} \rangle$ becomes extreme, i.e. the atoms fully polarize in either state only as a function of the sign of Δ. This follows from considering $N \to \infty$ in (5.36) which yields $\langle \hat{n}_{k_0} \rangle / N \to 1$ for $\Delta < 0$, $\langle \hat{n}_{k_0} \rangle / N \to 0$ for $\Delta > 0$, and $\langle \hat{n}_{k_0} \rangle / N \to 1/2$ when $\Delta = 0$ or in the bad cavity limit $|\Delta|/J \gg 1$.

The dynamical behavior of (5.33) is shown in Fig. 5.4(b). The system is initialized with all atoms in the k_0 state and with $\Delta = -2J$. As expected, the atoms mostly remain in this configuration when they approach the steady state. This can also be observed in the behavior of $\langle \hat{n}_{k_0} \rangle$ which remains very close to 1 throughout the entire evolution. As previously, the good match with the solutions obtained from (5.2) indicates the validity of our approximations.

The presence of optical pumping in this regime is interesting from the perspective of state preparation, as it could be used as a cavity cooling mechanism to maximize the number of particles in the BEC state. A similar strategy was used in [115] for cavity cooling by pumping the system along the cavity axis. The main difference with [115] is that here the energy splitting between atomic transitions is not given by the recoil energy of the atoms but instead by the hopping amplitude J. Analogously to Sec. 5.4.2, we expect the effects of finite but small U to be that of slowly scattering the atoms into other momentum configurations at a rate $U^2/J \ll \Gamma_\pm$ and a final state corresponding to each pair of momentum modes being equally populated but obeying a thermal distribution between the two modes.

5.6 Conclusions

In this chapter, we have studied the non-equilibrium dynamics of a gas of ultracold atoms inside an optical resonator, in the presence of an optical lattice and transverse

driving. We have shown that the relaxation dynamics of ultracold atomic inside optical cavities can display a wide variety of different behaviors, as a consequence of the competition between interactions, hopping and dissipation.

In the bad cavity regime, we obtained that the steady state always corresponds to infinite temperature. However, the approach to this steady state strongly depends on the considered parameter regime. For small hopping, we integrated the coherences of the density matrix to obtain a description only in terms of the probabilities associated to each atomic configuration and analyzed these quantities using a Gutzwiller ansatz and considering a continuum description in the limit of large filling f. The result was an algebraic decay of the particle number fluctuations, which can be associated with anomalous diffusion if one of the interaction strengths dominates over the other, or with normal diffusion when the interactions are of the same order. For large hopping, by performing a RWA, we obtained that the dynamics of the system is entirely dissipative and shown that the resulting master equation can be mapped into a linear rate equation. As a consequence, in this limit the approach of the steady state is given by a linear combination of exponential decays.

In contrast, in the good cavity regime, we found that for vanishing on-site interactions, the system evolves into a different steady state, given by a thermal distribution between pairs of momentum states. This allows for optical pumping between these pairs as the effective temperature can be controlled using the detuning Δ. This could be implemented as an alternative scheme for cavity-assisted cooling of atomic clouds in ultra-narrow band cavities, where one can access good cavity regime.

We believe that all the presented results are within experimental reach. Observation of the algebraic regime requires $(U, U_l, \gamma) \gg J$ as realized in [26], with $(U, U_l) = 10J$-$40J$. This can be tailored to $uN \ll \gamma$ or $uN \gg \gamma$, while satisfying the single-band approximation [26], i.e. all energy scales being much smaller that the interband energy gap. Tuning of the dissipation rate is available through $\gamma \propto V_0/\Delta^2$, where V_0 is the optical lattice depth, meaning that the ratio γ/J can be controlled. The regime of exponential relaxation could be observed by reducing the effective short-range interactions by means of Feshbach resonances, using external magnetic fields. Implementation of the bad cavity regime requires detuning the pump laser such that $|\Delta| \gg J$, and using an optical cavity with a linewidth of order $\kappa \sim$ MHz. Both conditions are already fulfilled in [26], where $\Delta \sim$ MHz and $J \sim$ Hz. Exploring the good cavity regime requires a detuning on the order of $\Delta \sim$ Hz and an ultranarrow-band optical cavity [52, 53, 115], where $\kappa \sim$ Hz.

Finally, it is worth emphasizing that our results rely on the adiabatic elimination scheme discussed in Sec. 5.3. It has been recently shown [120] that the approximations

needed to construct a Lindblad type master equation, i.e. bad cavity limit or RWA, can lead to unphysical results, e.g. the lack of a superradiant phase transition in the steady-state for the bad cavity regime due to the system always heating up to infinite temperature. Thus, it would be interesting to explore the corrections to our predictions by employing the approach presented in [120], corresponding to studying Eq. (5.5) numerically without making any further assumptions[3].

[3]In Sec. 5.3 we stated that since Eq. (5.5) is not in Lindblad form, it is not guaranteed that the dynamics of the system will remain physical. Nevertheless, it is mentioned in [120] that violation of physical properties only happens in very special cases.

Appendix

5.A Erratum in [1] and further details for Section 5.4.1

In this appendix we discuss the erratum found in [1], concerning the relaxation dynamics of Eq. (5.7) in the small hopping limit, and the calculation details behind the correction to this error, which lead to the expressions presented in Sec. 5.4.1.

Steps followed in [1]

As discussed in Sec. 5.3, after eliminating the cavity field by means of the Nakajima-Zwanzig method, in the bad-cavity limit, one is left with a master equation of the form

$$\dot{\hat{\rho}} = (-i)[\hat{H}_U + \hat{H}_J + \hat{H}_{U_l}, \hat{\rho}] + \gamma \mathcal{D}[\hat{\Phi}](\hat{\rho}). \tag{5.37}$$

Following the steps of [112–114], in [1] we analyzed the relaxation dynamics in the small hopping limit $J \ll (U, U_l, \gamma)$ by perturbatively eliminating the density matrix coherences in the equations of motion for the diagonal elements. The equation of motion presented in [1] for the coherences of $\hat{\rho} = \sum_{\mathbf{n},\mathbf{n}'} \rho_{\mathbf{n}}^{\mathbf{n}'} |\mathbf{n}'\rangle\langle\mathbf{n}|$ is

$$\partial_t \rho_{\mathbf{n}}^{\mathbf{n}+e^1_{i,j}} \simeq \left[-iu(n_i - n_j + 1) - 2\gamma\right] \rho_{\mathbf{n}}^{\mathbf{n}+e^1_{i,j}} + iJ\sqrt{n_i + 1}\sqrt{n_j}\left(\rho_{\mathbf{n}}^{\mathbf{n}} - \rho_{\mathbf{n}+e^1_{i,j}}^{\mathbf{n}+e^1_{i,j}}\right), \tag{5.38}$$

where we ignore further coupling between coherences. Most importantly, the role of the interactions was encapsulated in the parameter $u = U - 4U_l/K$. This led to the equations of motion

$$\partial_t \rho_{\mathbf{n}}^{\mathbf{n}} = 4\gamma J^2 \sum_{\substack{\langle i,j\rangle \\ d=\pm 1}} \frac{(n_i + \delta_{d,1})(n_j + \delta_{d,-1})}{u^2(n_i - n_j + d)^2 + 4\gamma^2} \left(\rho_{\mathbf{n}+e^d_{i,j}}^{\mathbf{n}+e^d_{i,j}} - \rho_{\mathbf{n}}^{\mathbf{n}}\right) \tag{5.39}$$

for the diagonal elements of $\hat{\rho}$, resulting in an algebraic relaxation of these quantities, which could be interpolated between anomalous diffusion ($u \gg \gamma$) and normal diffusion ($u = 0$) according to [1]. The error is precisely in these expressions, as the form of Eq. (5.38) is only valid for a double-well lattice $K = 2$. For $K > 2$, the terms proportional to U and γ remain correct, meaning that the anomalous diffusion discussed in [1] is valid,

but only in the regime where the term $\propto U_l$ is negligibly small compared to on-site interactions and dephasing. This is in accordance with the results presented in [112–114]. However, for $K > 2$ the contribution from $-i[\hat{H}_{U_l}, \hat{\rho}]$ is no longer proportional to $\frac{4iU_l}{K}(n_i - n_j + d)$ but instead acquires a more complicated form. In particular, it depends on the overall imbalance of the specific atomic configuration that is under consideration. In the following, we analyze the corrections to this behavior and provide more details on the derivation of the expressions presented in Sec. 5.4.1.

Corrections to erratum and calculation details for Sec. 5.4.1

Accounting for the in general non-vanishing imbalance, $\phi_0(\mathbf{n}) = \sum_e n_e - \sum_o n_o$ of a generic configuration $|\mathbf{n}\rangle$, the coherent evolution term yields

$$-i[\hat{H}_{U_l}, \hat{\rho}] = \frac{iU_l}{K} \sum_{\mathbf{n},\mathbf{n}'} \rho_{\mathbf{n}}^{\mathbf{n}'} [\hat{\Phi}^2, |\mathbf{n}'\rangle\langle\mathbf{n}|] = \frac{iU_l}{K} \sum_{\mathbf{n},\mathbf{n}'} \rho_{\mathbf{n}}^{\mathbf{n}'} (\phi_0(\mathbf{n}')^2 - \phi_0(\mathbf{n})^2) |\mathbf{n}'\rangle\langle\mathbf{n}|. \tag{5.40}$$

For $\mathbf{n}' = \mathbf{n} + e_{e,o}^{\pm 1}$, we obtain $(\phi_0(\mathbf{n}')^2 - \phi_0(\mathbf{n})^2) = \pm 4(\phi_0(\mathbf{n}) \pm 1)$, whereas for $\mathbf{n}' = \mathbf{n} + e_{o,e}^{\pm 1}$, $(\phi_0(\mathbf{n}')^2 - \phi_0(\mathbf{n})^2) = \mp 4(\phi_0(\mathbf{n}) \mp 1)$. Therefore, the equations of motion for the coherences read

$$\begin{aligned}
\partial_t \rho_{\mathbf{n}}^{\mathbf{n}+e_{e,o}^d} &\simeq d \left[-iU(n_e - n_o + d) + i\frac{4U_l}{K}(\phi_0 + d) - 2\gamma \right] \rho_{\mathbf{n}}^{\mathbf{n}+e_{e,o}^d} + iJ\sqrt{n_e + \delta_{d,1}}\sqrt{n_o + \delta_{d,-1}} \left(\rho_{\mathbf{n}}^{\mathbf{n}} - \rho_{\mathbf{n}+e_{e,o}^d}^{\mathbf{n}+e_{e,o}^d} \right) \\
\partial_t \rho_{\mathbf{n}}^{\mathbf{n}+e_{o,e}^d} &\simeq d \left[-iU(n_o - n_e + d) - i\frac{4U_l}{K}(\phi_0 - d) - 2\gamma \right] \rho_{\mathbf{n}}^{\mathbf{n}+e_{o,e}^d} + iJ\sqrt{n_e + \delta_{d,-1}}\sqrt{n_o + \delta_{d,1}} \left(\rho_{\mathbf{n}}^{\mathbf{n}} - \rho_{\mathbf{n}+e_{o,e}^d}^{\mathbf{n}+e_{o,e}^d} \right)
\end{aligned} \tag{5.41}$$

where we abbreviated $\phi_0 = \phi_0(\mathbf{n})$. Setting the time derivatives to 0 and plugging the result into the equations of motion for the diagonal terms, we obtain

$$\begin{aligned}
\partial_t \rho_{\mathbf{n}}^{\mathbf{n}} = 4\gamma J^2 \Bigg[& \sum_{\substack{\langle e,o \rangle \\ d=\pm 1}} \frac{(n_e + \delta_{d,1})(n_o + \delta_{d,-1})}{[U(n_e - n_o + d) - \frac{4U_l}{K}(\phi_0 + d)]^2 + 4\gamma^2} \left(\rho_{\mathbf{n}+e_{e,o}^d}^{\mathbf{n}+e_{e,o}^d} - \rho_{\mathbf{n}}^{\mathbf{n}} \right) + \\
& \sum_{\substack{\langle o,e \rangle \\ d=\pm 1}} \frac{(n_o + \delta_{d,1})(n_e + \delta_{d,-1})}{[U(n_o - n_e + d) + \frac{4U_l}{K}(\phi_0 - d)]^2 + 4\gamma^2} \left(\rho_{\mathbf{n}+e_{o,e}^d}^{\mathbf{n}+e_{o,e}^d} - \rho_{\mathbf{n}}^{\mathbf{n}} \right) \Bigg] = \\
4\gamma J^2 \Bigg[& \sum_{\substack{\langle e,o \rangle \\ d=\pm 1}} \frac{(n_e + \delta_{d,1})(n_o + \delta_{d,-1})}{[U(n_e - n_o + d) - \frac{4U_l}{K}(\phi_0 + d)]^2 + 4\gamma^2} \left(\rho_{\mathbf{n}+e_{e,o}^d}^{\mathbf{n}+e_{e,o}^d} - \rho_{\mathbf{n}}^{\mathbf{n}} \right) + \\
& \sum_{\substack{\langle o,e \rangle \\ d=\pm 1}} \frac{(n_o + \delta_{d,-1})(n_e + \delta_{d,1})}{[U(n_o - n_e - d) + \frac{4U_l}{K}(\phi_0 + d)]^2 + 4\gamma^2} \left(\rho_{\mathbf{n}+e_{e,o}^d}^{\mathbf{n}+e_{e,o}^d} - \rho_{\mathbf{n}}^{\mathbf{n}} \right) \Bigg],
\end{aligned} \tag{5.42}$$

where we flipped the sign of d in the fourth line and made use of $e^{d}_{i,j} = e^{-d}_{j,i}$. Note that for $K = 2$, $\phi_0 = n_e - n_o$, thus retrieving the results from [1].

To simplify things, we introduce a Gutzwiller ansatz $\hat{\rho}(t) = \bigotimes_{j=1}^{K} \left[\sum_{n_j} \rho_j(n_j,t)|n_j\rangle\langle n_j|\right]$, resulting in $\rho^{\mathbf{n}}_{\mathbf{n}}(t) = \prod_j \rho_j(n_j,t)$. Inserting this into Eq. (5.42) and tracing over all sites except for a particular site l we are left with

$$\partial_t \rho_l(n_l,t) = 4\gamma J^2 \sum_{\substack{\{n_k\}\\ k\neq l}} \sum_{\substack{\langle i,j\rangle\\ d=\pm 1}} \tau(n_e,n_o;\mathbf{n},d)\,(\rho_1\dots\rho_K)\,(\rho_e(n_e+d,t)\rho_o(n_o-d,t) - \rho_e(n_e,t)\rho_o(n_o,t))\,, \tag{5.43}$$

where the labels (e,o) stand for whichever index (i,j) is even or odd, with the definition $\tau(n_e,n_o;\mathbf{n},d) = \frac{(n_e+\delta_{d,1})(n_o+\delta_{d,-1})}{[U(n_e-n_o+d)-\frac{4U_l}{K}(\phi_0+d)]^2+4\gamma^2}$. Note that this is consistent with the result in Eq. (5.42). At this point, we can cancel the terms where neither $(i,j)\neq l$ by noting that $\tau(n_e-d,n_o+d;\mathbf{n},d) = \tau(n_e,n_o;\mathbf{n},-d)$

$$\begin{aligned}
&\cdots \sum_{\substack{n_e=0,n_o=0\\ d=\pm 1}} \tau(n_e,n_o;\mathbf{n},d)\Big[\rho_e(n_e+d,t)\rho_o(n_o-d,t) - \rho_i(n_e,t)\rho_o(n_j,t)\Big]\\
&\cdots \sum_{\substack{n_e=d,n_o=-d\\ d=\pm 1}} \tau(n_e-d,n_o+d;\mathbf{n},d)\rho_e(n_e,t)\rho_o(n_o,t) - \sum_{\substack{n_e=0,n_o=0\\ d=\pm 1}} \tau(n_e,n_o;\mathbf{n},d)\rho_i(n_e,t)\rho_o(n_j,t)\\
&\cdots \sum_{\substack{n_e=0,n_o=0\\ d=\pm 1}} \tau(n_e,n_o;\mathbf{n},-d)\rho_e(n_e,t)\rho_o(n_o,t) - \sum_{\substack{n_e=0,n_o=0\\ d=\pm 1}} \tau(n_e,n_o;\mathbf{n},d)\rho_i(n_e,t)\rho_o(n_j,t) = 0,
\end{aligned} \tag{5.44}$$

where in the third line we exploited that $\tau(n_e,n_o;\mathbf{n},-d) = 0$ when either $(n_e,n_o) = 0$ and that $\rho_j(n,t) = 0$ for $n < 0$, allowing us to reset the sum limits back to $(n_e,n_o) = 0$. We further simplify expression (5.43) by introducing a homogeneity approximation

$\rho_j(n_j,t) = \rho_e(n_j,t)\ \forall\ j$ even and $\rho_j(n_j,t) = \rho_o(n_j,t)\ \forall\ j$ odd. This yields

$$\begin{aligned}
\partial_t \rho_e(n_i,t) = 4z\gamma J^2 \sum_{\substack{\{n_k\}\\ k\neq i}} \sum_{d=\pm 1} & \frac{(n_i+\delta_{d,1})(n_j+\delta_{d,-1})}{[U(n_i-n_j+d)-\frac{4U_l}{K}(n_i-n_j+d+\varphi_{\mathbf{n}})]^2+4\gamma^2} \\
& \times \left(\prod_{\substack{p\in e\\ p\neq i}} \rho_e(n_p,t)\right)\left(\prod_{\substack{q\in o\\ q\neq j}} \rho_o(n_q,t)\right)\Big(\rho_e(n_i+d,t)\rho_o(n_j-d,t)-\rho_e(n_i,t)\rho_o(n_j,t)\Big) \\
\partial_t \rho_o(n_i,t) = 4z\gamma J^2 \sum_{\substack{\{n_k\}\\ k\neq i}} \sum_{d=\pm 1} & \frac{(n_i+\delta_{d,1})(n_j+\delta_{d,-1})}{[U(n_i-n_j+d)-\frac{4U_l}{K}(n_i-n_j+d-\varphi_{\mathbf{n}})]^2+4\gamma^2} \\
& \times \left(\prod_{\substack{p\in e\\ p\neq j}} \rho_e(n_p,t)\right)\left(\prod_{\substack{q\in o\\ q\neq i}} \rho_o(n_q,t)\right)\Big(\rho_o(n_i+d,t)\rho_e(n_j-d,t)-\rho_o(n_i,t)\rho_e(n_j,t)\Big),
\end{aligned} \tag{5.45}$$

where we introduced the coordination number z, and split the imbalance $\phi_0(\mathbf{n})$ into the contribution from i and j and the contribution from the rest of the lattice $\varphi_{\mathbf{n}} = \sum_{p\in e,p\neq i} n_p - \sum_{q\in o,q\neq j} n_q$. For $K=2$, we have $\varphi_{\mathbf{n}}=0$ and we can trace out all of the sites except l and j, thus retrieving the results in [1, 112–114]. In general, however, for $K>2$ this is not possible anymore and we need to account for all possible imbalance configurations of the full lattice $\varphi_{\mathbf{n}}\neq 0$. From these expressions, the rest of the analysis proceeds as described in Sec. 5.4.1.

6

Conclusion and Outlook

In this thesis we have investigated the physics of ultracold atoms coupled to optical cavities. We have studied several variations of this concept and uncovered new routes for quantum simulations as well as novel out-of-equilibrium phenomena resulting from the dissipative processes intrinsic to cavity QED.

In Chapter 3, we considered a system consisting of a BEC cloud interacting with three different optical resonators. By performing a mean-field analysis we computed the ground-state phase diagram, and the main defining features of each phase. Specifically, we obtained that by tuning the light-matter couplings and the cavity-pump detunings it is possible to interpolate between different global rotational symmetries in the system. For three different resonators these can be either $\mathbb{Z}_2$, $U(1)$ or $SO(3)$ and they can be spontaneously broken. We gained further insight by computing the excitation spectrum and shown that Goldstone(roton) modes emerge upon spontaneously breaking the continuous(discrete) symmetry. This provides evidence that for n resonators it is in principle to possible simulate systems exhibiting an $SO(n)$ rotational symmetry. We also made connection with the experiments by considering the different atomic configurations that emerge when entering the symmetry broken phases.

These results take atom-cavity systems one step forward as quantum simulators. Besides realizing this phenomena experimentally, it would be exciting to consider what are the effects of accounting for more momentum states in the low-energy description. There is evidence that these type of coupling leads to intertwined order [30] and the presence of richer symmetries could yield interesting complex phenomena. A customary task would be to evaluate the precise effects of noise and dissipation of the phase diagram in order to assess the presence of this symmetries in realistic scenarios.

In Chapter 4, we studied the driven-dissipative dynamics of a spinor BEC coupled to a

single cavity mode. We showed that the vectorial coupling resulting from misalignment between pump and cavity polarizations resulted in the cavity mode mediating non-reciprocal interactions between the two spin species. We found that the non-reciprocal coupling had a major impact on the form of the phase diagram, resulting in the emergence of an unstable phase dominated by perpetual oscillations of the system observables. We tracked the origin of the non-reciprocal coupling to the phase shift generated by the cavity mode through dissipative processes. Thus, we concluded that the presence of this instability was induced by dissipation.

This work paves the way for exploring novel phenomena exploiting this dissipative effect. This is particularly exciting from the perspective of non-reciprocal interactions as they have not yet been discussed in the context of many-body systems. A natural follow up would be to perform an in depth analysis of the dynamical behavior of the system, in analogy with [42], to properly characterize the boundaries of the unstable region and its main properties. Using this knowledge, an exciting route would be to place this system under the influence of an external optical lattice potential in the same spirit as Chapter 5 and study the effects of the instability. We expect a competition between non-reciprocal interactions trying drive the system between different CDW configurations and short-range interactions trying to stabilize a MI phase. We know from Chapter 5 that this competition has a strong impact on the phase diagram of the system, and the presence of non-reciprocity could lead to the stabilization of exotic non-equilibrium phases and novel dynamical behavior.

The last part of our work was presented in Chapter 5, where we considered a BEC cloud interacting with a single mode of a cavity and placed under an external lattice potential. We derived an effective master equation by eliminating the photonic degrees of freedom and studied the relaxation dynamics of the system. In the bad-cavity limit, we obtained an infinite temperature steady-state which could be approached either algebraically or exponentially, depending on the strength of the interactions relative to the hopping parameter. Moreover, in the former case, the decay towards the steady state corresponds to either anomalous or normal diffusion, as a result of the competition between short and long range interactions. In the good cavity regime, for small interactions, we found that the relaxation dynamics were still exponential but towards a steady state with a thermal distribution between the BEC state and the first excited momentum state. These findings demonstrate how the high complexity of a many-body system can have a strong impact on its relaxation dynamics. This lattice-cavity system offers an exciting opportunity to observe and study these different regimes. Interestingly, the diffusive behavior predicted by [113] was recently observed experimentally for a BH model generated using optical

lattices [121]. The measurements of the correlations necessitated only of time-of-flight protocols, readily available in atom-cavity systems.

Overall, the work presented in this thesis evidences the capacity and the versatility of quantum gases coupled to optical cavities. There are numerous directions to be further explored in the future with the advent of increasing complexity in these platforms. Among many others, two natural extensions of the paradigm considered here are accounting for extra cavity modes and time-dependent coupling. The former has already shown exciting results and promises to lead the next generation of quantum simulation experiments in cavity systems, given their tunability of sign and range of interactions [25]. The latter is currently under development, with some studies exploring the possibility for time crystals [122, 123], and others delving into the field of quantum control by implementing feedback protocols in the driving scheme [124, 125]. Finally, we hope the ideas discussed throughout this thesis, which constitute Refs. [1–3], stimulate further studies and spark new exciting ideas in this rapidly growing field.

Bibliography

[1] E. I. Rodríguez Chiacchio and A. Nunnenkamp, Phys. Rev. A **97**, 033618 (2018).

[2] E. I. R. Chiacchio and A. Nunnenkamp, Phys. Rev. A **98**, 023617 (2018).

[3] E. I. R. Chiacchio and A. Nunnenkamp, Phys. Rev. Lett. **122**, 193605 (2019).

[4] S. Chu, Rev. Mod. Phys. **70**, 685 (1998).

[5] C. N. Cohen-Tannoudji, Rev. Mod. Phys. **70**, 707 (1998).

[6] W. D. Phillips, Rev. Mod. Phys. **70**, 721 (1998).

[7] E. A. Cornell and C. E. Wieman, Rev. Mod. Phys. **74**, 875 (2002).

[8] W. Ketterle, Rev. Mod. Phys. **74**, 1131 (2002).

[9] I. Bloch, J. Dalibard, and W. Zwerger, Rev. Mod. Phys. **80**, 885 (2008).

[10] I. Bloch, J. Dalibard, and S. Nascimbene, Nat Phys **8**, 267 (2012).

[11] C. Gross and I. Bloch, Science (80-.). **357**, 995 (2017).

[12] M. Greiner, O. Mandel, T. Esslinger, T. W. Hänsch, and I. Bloch, Nature **415**, 39 (2002).

[13] R. Jördens, N. Strohmaier, K. Günter, H. Moritz, and T. Esslinger, Nature **455**, 204 (2008).

[14] U. Schneider, L. Hackermüller, S. Will, T. Best, I. Bloch, T. A. Costi, R. W. Helmes, D. Rasch, and A. Rosch, Science (80-.). **322**, 1520 (2008).

[15] M. Aidelsburger, M. Atala, M. Lohse, J. T. Barreiro, B. Paredes, and I. Bloch, Phys. Rev. Lett. **111**, 185301 (2013).

[16] H. Miyake, G. A. Siviloglou, C. J. Kennedy, W. C. Burton, and W. Ketterle, Phys. Rev. Lett. **111**, 185302 (2013).

[17] G. Jotzu, M. Messer, R. Desbuquois, M. Lebrat, T. Uehlinger, D. Greif, and T. Esslinger, Nature **515**, 237 (2014).

[18] M. Schreiber, S. S. Hodgman, P. Bordia, H. P. Lüschen, M. H. Fischer, R. Vosk, E. Altman, U. Schneider, and I. Bloch, Science (80-.). **349**, 842 (2015).

[19] R. Blatt and C. F. Roos, Nat. Phys. **8**, 277 (2012).

[20] A. A. Houck, H. E. Türeci, and J. Koch, Nat. Phys. **8**, 292 (2012).

[21] C.-L. Hung, A. González-Tudela, J. I. Cirac, and H. J. Kimble, Proc. Natl. Acad. Sci. **113**, E4946 (2016).

[22] H. Ritsch, P. Domokos, F. Brennecke, and T. Esslinger, Rev. Mod. Phys. **85**, 553 (2013).

[23] K. Baumann, C. Guerlin, F. Brennecke, and T. Esslinger, Nature **464**, 1301 (2010).

[24] A. J. Kollár, A. T. Papageorge, V. D. Vaidya, Y. Guo, J. Keeling, and B. L. Lev, Nat. Commun. **8**, 14386 (2017).

[25] V. D. Vaidya, Y. Guo, R. M. Kroeze, K. E. Ballantine, A. J. Kollár, J. Keeling, and B. L. Lev, Phys. Rev. X **8**, 011002 (2018).

[26] R. Landig, L. Hruby, N. Dogra, M. Landini, R. Mottl, T. Donner, and T. Esslinger, Nature **532**, 476 (2016).

[27] J. Klinder, H. Keßler, M. R. Bakhtiari, M. Thorwart, and A. Hemmerich, Phys. Rev. Lett. **115**, 230403 (2015).

[28] J. Léonard, A. Morales, P. Zupancic, T. Esslinger, and T. Donner, Nature **543**, 87 (2017).

[29] J. Léonard, A. Morales, P. Zupancic, T. Donner, and T. Esslinger, Science **358**, 1415 (2017).

[30] A. Morales, P. Zupancic, J. Léonard, T. Esslinger, and T. Donner, Nat. Mater. **17**, 686 (2018).

[31] R. M. Kroeze, Y. Guo, V. D. Vaidya, J. Keeling, and B. L. Lev, Phys. Rev. Lett. **121**, 163601 (2018).

[32] M. Landini, N. Dogra, K. Kroeger, L. Hruby, T. Donner, and T. Esslinger, Phys. Rev. Lett. **120**, 223602 (2018).

[33] N. Dogra, M. Landini, K. Kroeger, L. Hruby, T. Donner, and T. Esslinger, (2019), arXiv:1901.05974 .

[34] R. H. Dicke, Phys. Rev. **93**, 99 (1954).

[35] E. T. Jaynes and F. W. Cummings, Proc. IEEE **51**, 89 (1963).

[36] C. Maschler, I. B. Mekhov, and H. Ritsch, Eur. Phys. J. D **46**, 545 (2008).

[37] K. Hepp and E. H. Lieb, Phys. Rev. A **8**, 2517 (1973).

[38] Y. K. Wang and F. T. Hioe, Phys. Rev. A **7**, 831 (1973).

[39] C. Emary and T. Brandes, Phys. Rev. E **67**, 066203 (2003).

[40] F. Dimer, B. Estienne, A. S. Parkins, and H. J. Carmichael, Phys. Rev. A **75**, 013804 (2007).

[41] D. Nagy, G. Kónya, G. Szirmai, and P. Domokos, Phys. Rev. Lett. **104**, 130401 (2010).

[42] J. Keeling, M. J. Bhaseen, and B. D. Simons, Phys. Rev. Lett. **105**, 043001 (2010).

[43] D. Nagy, G. Szirmai, and P. Domokos, Phys. Rev. A **84**, 043637 (2011).

[44] M. J. Bhaseen, J. Mayoh, B. D. Simons, and J. Keeling, Phys. Rev. A **85**, 013817 (2012).

[45] P. Kirton and J. Keeling, Phys. Rev. Lett. **118**, 123602 (2017).

[46] P. Domokos and H. Ritsch, Phys. Rev. Lett. **89**, 253003 (2002).

[47] A. T. Black, H. W. Chan, and V. Vuletić, Phys. Rev. Lett. **91**, 203001 (2003).

[48] K. Baumann, R. Mottl, F. Brennecke, and T. Esslinger, Phys. Rev. Lett. **107**, 140402 (2011).

[49] B. Öztop, M. Bordyuh, Ö. E. Müstecaplıoğlu, and H. E. Türeci, New J. Phys. **14**, 085011 (2012).

[50] R. Mottl, F. Brennecke, K. Baumann, R. Landig, T. Donner, and T. Esslinger, Science (80-.). **336**, 1570 LP (2012).

[51] F. Brennecke, R. Mottl, K. Baumann, R. Landig, T. Donner, and T. Esslinger, Proc. Natl. Acad. Sci. U. S. A. **110**, 11763 (2013).

[52] H. Kessler, J. Klinder, M. Wolke, and A. Hemmerich, Phys. Rev. Lett. **113**, 070404 (2014).

[53] J. Klinder, H. Keßler, M. Wolke, L. Mathey, and A. Hemmerich, Proc. Natl. Acad. Sci. U. S. A. **112**, 3290 (2015).

[54] A. E. Niederle, G. Morigi, and H. Rieger, Phys. Rev. A **94**, 033607 (2016).

[55] L. Hruby, N. Dogra, M. Landini, T. Donner, and T. Esslinger, Proc. Natl. Acad. Sci. U. S. A. , 201720415 (2018).

[56] N. Dogra, F. Brennecke, S. D. Huber, and T. Donner, Phys. Rev. A **94**, 023632 (2016).

[57] B. Sundar and E. J. Mueller, Phys. Rev. A **94**, 033631 (2016).

[58] T. Flottat, L. d. F. de Parny, F. Hébert, V. G. Rousseau, and G. G. Batrouni, Phys. Rev. B **95**, 144501 (2017).

[59] C. W. Gardiner and H. Haken, *Quantum noise*, Vol. 26 (Springer Berlin, 1991).

[60] H.-P. Breuer and F. Petruccione, *The Theory of Open Quantum Systems* (Oxford University Press, 2007).

[61] M. A. Nielsen and I. L. Chuang, *Quantum Computation and Quantum Information: 10th Anniversary Edition*, 10th ed. (Cambridge University Press, USA, 2011).

[62] F. Verstraete, M. M. Wolf, and J. Ignacio Cirac, Nat. Phys. **5**, 633 (2009).

[63] S. Diehl, A. Tomadin, A. Micheli, R. Fazio, and P. Zoller, Phys. Rev. Lett. **105**, 015702 (2010).

[64] L. M. Sieberer, S. D. Huber, E. Altman, and S. Diehl, Phys. Rev. Lett. **110**, 195301 (2013).

[65] A. Le Boité, G. Orso, and C. Ciuti, Phys. Rev. Lett. **110**, 233601 (2013).

[66] A. Biella, F. Storme, J. Lebreuilly, D. Rossini, R. Fazio, I. Carusotto, and C. Ciuti, (2017), arXiv:1704.08978 .

[67] F. Minganti, A. Biella, N. Bartolo, and C. Ciuti, Phys. Rev. A **98**, 042118 (2018).

[68] W. Casteels, R. Fazio, and C. Ciuti, Phys. Rev. A **95**, 012128 (2017).

[69] S. Nakajima, Prog. Theor. Phys. **20**, 948 (1958).

[70] R. Zwanzig, J. Chem. Phys. **33**, 1338 (1960).

[71] I. de Vega and D. Alonso, Rev. Mod. Phys. **89**, 015001 (2017).

[72] J. Piilo, S. Maniscalco, K. Härkönen, and K.-A. Suominen, Phys. Rev. Lett. **100**, 180402 (2008).

[73] J. Piilo, K. Härkönen, S. Maniscalco, and K.-A. Suominen, Phys. Rev. A **79**, 062112 (2009).

[74] V. V. Albert and L. Jiang, Phys. Rev. A **89**, 22118 (2014).

[75] C. Navarrete-Benlloch, (2015), arXiv:1504.05266 .

[76] J. Lang, F. Piazza, and W. Zwerger, New J. Phys. **19**, 123027 (2017).

[77] S. Gopalakrishnan, Y. E. Shchadilova, and E. Demler, Phys. Rev. A **96**, 063828 (2017).

[78] A. Baksic and C. Ciuti, Phys. Rev. Lett. **112**, 173601 (2014).

[79] J. Fan, Z. Yang, Y. Zhang, J. Ma, G. Chen, and S. Jia, Phys. Rev. A **89**, 023812 (2014).

[80] R. I. Moodie, K. E. Ballantine, and J. Keeling, Phys. Rev. A **97**, 033802 (2018).

[81] D. Nagy, G. Szirmai, and P. Domokos, Eur. Phys. J. D **48**, 127 (2008).

[82] K. E. Ballantine, B. L. Lev, and J. Keeling, Phys. Rev. Lett. **118**, 045302 (2017).

[83] D. Nagy, G. Kónya, P. Domokos, and G. Szirmai, Phys. Rev. A **97**, 063602 (2018).

[84] M. Soriente, T. Donner, R. Chitra, and O. Zilberberg, Phys. Rev. Lett. **120**, 183603 (2018).

[85] F. Le Kien, P. Schneeweiss, and A. Rauschenbeutel, Eur. Phys. J. D **67**, 92 (2013).

[86] F. Brennecke, T. Donner, S. Ritter, T. Bourdel, M. Köhl, and T. Esslinger, Nature **450**, 268 (2007).

[87] Y. Colombe, T. Steinmetz, G. Dubois, F. Linke, D. Hunger, and J. Reichel, Nature **450**, 272 (2007).

[88] I. B. Mekhov, C. Maschler, and H. Ritsch, Nat. Phys. **3**, 319 (2007).

[89] W. Chen, D. Meiser, and P. Meystre, Phys. Rev. A **75**, 023812 (2007).

[90] F. Mivehvar, F. Piazza, and H. Ritsch, Phys. Rev. Lett. **119**, 063602 (2017).

[91] F. Mivehvar, H. Ritsch, and F. Piazza, Phys. Rev. Lett. **122**, 113603 (2019).

[92] Z. Zhiqiang, C. H. Lee, R. Kumar, K. J. Arnold, S. J. Masson, A. S. Parkins, and M. D. Barrett, Optica **4**, 424 (2017).

[93] M. A. Norcia, R. J. Lewis-Swan, J. R. K. Cline, B. Zhu, A. M. Rey, and J. K. Thompson, Science (80-.). **361**, 259 (2018).

[94] E. J. Davis, G. Bentsen, L. Homeier, T. Li, and M. H. Schleier-Smith, Phys. Rev. Lett. **122**, 010405 (2019).

[95] J. Lang and F. Piazza, Phys. Rev. A **94**, 033628 (2016).

[96] W. Zheng and N. R. Cooper, Phys. Rev. A **97**, 021601 (2018).

[97] B. Buca, J. Tindall, and D. Jaksch, (2018), arXiv:1804.06744 .

[98] S. Diehl, E. Rico, M. A. Baranov, and P. Zoller, Nat. Phys. **7**, 971 (2011).

[99] N. Moiseyev, *Non-Hermitian Quantum Mechanics* (Cambridge University Press, Cambridge, 2011).

[100] F. Marquardt, J. P. Chen, A. A. Clerk, and S. M. Girvin, Phys. Rev. Lett. **99**, 093902 (2007).

[101] N. Shammah, S. Ahmed, N. Lambert, S. De Liberato, and F. Nori, Phys. Rev. A **98**, 063815 (2018).

[102] D. Jalas, A. Petrov, M. Eich, W. Freude, S. Fan, Z. Yu, R. Baets, M. Popović, A. Melloni, J. D. Joannopoulos, M. Vanwolleghem, C. R. Doerr, and H. Renner, Nat. Photonics **7**, 579 (2013).

[103] P. Lodahl, S. Mahmoodian, S. Stobbe, A. Rauschenbeutel, P. Schneeweiss, J. Volz, H. Pichler, and P. Zoller, Nature **541**, 473 (2017).

[104] N. R. Bernier, L. D. Tóth, A. Koottandavida, M. A. Ioannou, D. Malz, A. Nunnenkamp, A. K. Feofanov, and T. J. Kippenberg, Nat. Commun. **8**, 604 (2017).

[105] E. Verhagen and A. Alù, Nat. Phys. **13**, 922 (2017).

[106] M. Harder, Y. Yang, B. Yao, C. Yu, J. Rao, Y. Gui, R. Stamps, and C.-M. Hu, Phys. Rev. Lett. **121**, 137203 (2018).

[107] M. Xu, D. A. Tieri, E. C. Fine, J. K. Thompson, and M. J. Holland, Phys. Rev. Lett. **113**, 154101 (2014).

[108] G. Mazzucchi, W. Kozlowski, S. F. Caballero-Benitez, T. J. Elliott, and I. B. Mekhov, Phys. Rev. A **93**, 023632 (2016).

[109] D. Jaksch, C. Bruder, J. I. Cirac, C. W. Gardiner, and P. Zoller, Phys. Rev. Lett. **81**, 3108 (1998).

[110] B. Blaß, H. Rieger, G. Roósz, and F. Iglói, Phys. Rev. Lett. **121**, 095301 (2018).

[111] Z. Cai and T. Barthel, Phys. Rev. Lett. **111**, 150403 (2013).

[112] D. Poletti, J.-S. Bernier, A. Georges, and C. Kollath, Phys. Rev. Lett. **109**, 045302 (2012).

[113] D. Poletti, P. Barmettler, A. Georges, and C. Kollath, Phys. Rev. Lett. **111**, 195301 (2013).

[114] B. Sciolla, D. Poletti, and C. Kollath, Phys. Rev. Lett. **114**, 170401 (2015).

[115] M. Wolke, J. Klinner, H. Keßler, and A. Hemmerich, Science (80-.). **337**, 75 (2012).

[116] C.-M. Halati, A. Sheikhan, H. Ritsch, and C. Kollath, (2019), arXiv:1909.07335 .

[117] A. A. Clerk, M. H. Devoret, S. M. Girvin, F. Marquardt, and R. J. Schoelkopf, Rev. Mod. Phys. **82**, 1155 (2010).

[118] D. A. Lidar and K. Birgitta Whaley, "Decoherence-Free Subspaces and Subsystems," in *Irreversible Quantum Dyn.*, edited by F. Benatti and R. Floreanini (Springer Berlin Heidelberg, Berlin, Heidelberg, 2003) pp. 83–120.

[119] J. Kempe, D. Bacon, D. A. Lidar, and K. B. Whaley, Phys. Rev. A **63**, 042307 (2001).

[120] F. Damanet, A. J. Daley, and J. Keeling, Phys. Rev. A **99**, 033845 (2019).

[121] R. Bouganne, M. Bosch Aguilera, A. Ghermaoui, J. Beugnon, and F. Gerbier, Nat. Phys. **16**, 21 (2020).

[122] H. Keßler, J. G. Cosme, M. Hemmerling, L. Mathey, and A. Hemmerich, Phys. Rev. A **99**, 053605 (2019).

[123] J. G. Cosme, J. Skulte, and L. Mathey, Phys. Rev. A **100**, 053615 (2019).

[124] D. Ivanov, T. Ivanova, S. Caballero-Benitez, and I. Mekhov, Phys. Rev. Lett. **124**, 010603 (2020).

[125] K. Kroeger, N. Dogra, R. Rosa-Medina, M. Paluch, F. Ferri, T. Donner, and T. Esslinger, (2019), arXiv:1912.02505 .